

Sculpting with light: light/matter interactions in biocompatible polymers

A dissertation submitted by

Matthew B. Applegate

in partial fulfillment for the requirements for the degree of

Doctor of Philosophy
in
Biomedical Engineering

Tufts University

August 2016

Adviser:
Fiorenzo G. Omenetto

Abstract

When light interacts with matter either the light or the material can be changed. This dissertation focuses on light/matter interaction in silk fibroin and its utility for biomedical applications. Silk, a natural biocompatible, biodegradable polymer, has a large 3-photon absorption cross-section which allows modest peak intensity light to cause significant multiphoton absorption. This absorption allows voids to be formed with three dimensional control within soft, transparent silk hydrogels. A theoretical model of the void formation process is developed to allow the size of the voids to be predicted for a range of laser and sample parameters. Arbitrary 3D patterns are created in silk gels that allow cells to penetrate into the bulk of the gel both *in vitro* and *in vivo*. To explore how silk can be used to alter light, the creation of step-index optical waveguides, formed by encapsulating a silk film within a silk hydrogel, is described. These waveguides allow light to be delivered to targets through several centimeters of highly scattering biological tissue. Finally, the interaction of light with riboflavin is used to photocrosslink silk to form solid structures, rather than voids. The mechanism of crosslinking to be driven by radicalized tyrosine residues resulting in the formation of dityrosine bonds which lead to the gelation of a liquid silk solution. Riboflavin is a versatile photoinitiator and can be used to crosslink collagen as well as silk, which allows silk to be crosslinked directly to corneal collagen. When applied

to the eye, an artificial corneal layer is formed which has the potential to treat various corneal diseases and allow for risk-free laser vision correction. These studies show the versatility of light-based processing of silk for a wide variety of medical applications.

Acknowledgements

I would like to thank both my committee, and everyone in both the Omenetto and Kaplan labs who made this dissertation possible. Special thanks to Benjamin Partlow for many engaging discussions both on- and off-topic, Mark Brenckle for his ever-practical advice, Hu “Tiger” Tao for his unflagging enthusiasm, Giovanni Perotto for his ability to always see right to the heart of the problem, Carlo Alonzo for his patience and knowledge of nonlinear optics, Benedetto Marelli for his ability to connect his deep understanding of silk to practical applications, and Milva Ricci for all her help and support. I would also like to acknowledge financial support from the Stern Fellowship at Tufts University, the Tufts University Graduate Student Research Competition, and the National Science and Engineering Graduate Student Fellowship. Finally, my thanks to my partner Ariel White who’s been there for me through thick and thin.

Contents

1	Introduction	2
1.1	Structuring soft materials	4
1.2	Photomodification	5
1.3	Importance of 3D structures in medicine	6
1.3.1	Light-based methods of creating 3D structures	7
1.4	Conclusion	13
2	Background	22
2.1	Nonlinear optical susceptibility	23
2.2	Mode-locking	24
2.3	Multiphoton absorption theory	29
2.3.1	Qualitative description	30
2.3.2	Quantum mechanical description	31
2.4	Material damage	37
3	Nonlinear absorption in silk	44
3.1	Introduction	44
3.2	Materials & methods	45
3.2.1	Data Processing	48
3.3	Results	51
3.4	Discussion	53

4	Micropatterning silk	61
4.1	Model development	64
4.2	Validating the model	68
4.2.1	Sample preparation	69
4.2.2	Feature measurement	69
4.2.3	Parameter measurement	70
4.2.4	Pulse repetition frequency	71
4.2.5	Pulse energy	72
4.2.6	Pulse width	72
4.2.7	Spot size	75
4.2.8	Determining critical energy	75
4.2.9	Wavelength	79
4.3	Prediction	80
4.4	Micromachining in solid silk	82
4.5	Conclusion	85
5	Micromachining applications	89
5.1	Introduction	89
5.2	Results	92
5.3	Discussion	102
5.4	Materials & Methods	103
6	Silk waveguides	111
6.1	Introduction	111
6.2	Methods	114
6.3	Results	117
6.4	Discussion	119

7	Silk/riboflavin	125
7.1	Introduction	125
7.2	Results	128
7.3	Discussion	135
7.4	Materials & Methods	139
8	Conclusion & future directions	148
8.1	Future Directions	150
	Appendix A Model feature	158
	Appendix B ImageJ Macro	163

List of Tables

3.1	Summary of multiphoton absorption findings in silk and amino acid solutions. Cross sections are presented as the mean \pm standard error.	53
-----	---	----

List of Figures

1.1	Simulated intensity distribution of a focused beam where only the central region is above the threshold for two-photon absorption. This illustrates how regions smaller than the diffraction limited spot can be addressed.	12
2.1	The gain spectrum (solid line) plotted vs. frequency on the x-axis. Individual laser modes oscillate with a frequency spacing of $c/2d$. The total bandwidth of the gain medium $\Delta\nu$ is the spectral width of the gain medium that is capable of lasing (ie the gain is greater than the loss).	25
2.2	Plot of equation 2.3 showing the output intensity of a laser oscillating with 6 modes where A_n follows a Gaussian shape. The intensity fluctuations repeat with a period of the inverse of the intermodal spacing ($1/\partial\nu$). The highest frequency fluctuations occur with a period of $1/\Delta\nu$. The dotted line represents the average intensity of the laser.	26

2.3	Intensity profile of a laser oscillating with 6 modes whose amplitudes follow a Gaussian shape. The fixed phase relationship ensures that the modes constructively interfere at a single point in time leading to the generation of a short pulse that repeats with a frequency of $\partial\nu$. The dotted line indicates the average intensity of the laser which is the same as in Figure 2.2.	27
2.4	Illustration of the electric field in a mode locked laser. Gray lines show the modes oscillating at slightly different frequencies but with a fixed phase relationship. The sum of the modes is shown in red where the electric field of a short optical pulse can be seen.	28
2.5	Energy level diagram illustrating 2 photon absorption. The ground energy level (E_1) is separated from the excited state (E_2) by a certain amount of energy. Electrons can be excited by a single photon of light with energy $h\nu$ or by two photons with half the energy ($h\nu/2$) via a virtual state (dashed line). .	31
2.6	Evaluation of the second term of equation 2.23 for varying values of t . As t increases the peak becomes sharper and has a maximum value of t^2	36
2.7	Schematic diagram of avalanche ionization leading to material damage. Adapted from Ref. [22].	39

3.1	Schematic representation of Z-scan technique for measuring optical nonlinearity. Neutral density filters (ND) are used to control the pulse energy. Aperture (A1) spatially filters the beam. A lens (L1) focuses the beam onto the sample which is scanned along the optical axis. A second aperture (A2) can be left open to measure the imaginary part of the hyperpolarizability or closed to measure the real component. The beam is collimated by another lens (L2), split by a beamsplitter (BS) and focused onto a detector by L3. Beam block (BB) stops light transmitted by the beamsplitter.	46
3.2	Representative gel electrophoresis sample of silk boiled for 10, 30, 60, and 120 minutes.	47
3.3	Measurement of the beam waist using the knife edge method showing a FWHM of 30 μm	48
3.4	Screenshot of the custom LabView application designed to automatically run a single Z-scan experiment	49
3.5	Z-scan data analysis workflow. First high and low energy scans are taken of the sample and the solvent and normalized. These are subtracted to correct for sample imperfections and alignment issues. The 3-photon coefficient (β_2) is then calculated. The coefficients are subtracted to calculate the 3-photon cross-section.	50
3.6	Representative open aperture Z-scan data from 100 kDa silk fibroin solution with theoretical best fit curve for two-photon absorption (dashed) and three-photon absorption (solid). . . .	52

3.7	Maximum change in transmission during the Z-scan is roughly linear with respect to silk concentration. Error bars represent 1 standard deviation (n=3).	53
3.8	A) Normalized change in transmission for the solutions tested after accounting for the contribution of the solvent. TRP is tryptophan in HCl, TYR is tyrosine in HCl. SF 10mb to SF 120mb indicate the length of time the silk was boiled during degumming. Error bars indicate 95% confidence intervals. B) Plot of 3PA cross section and silk molecular weight. Error bars indicate the 95% confidence intervals. Note the y-axis is plotted on a log scale.	54
4.1	Side view of marks made in a silk hydrogel after exposure to varying numbers of ultrashort pulses taken with a phase contrast microscope. Laser was incident from the bottom of the image.	62
4.2	The laser was incident from the left to create voids at different depths below the surface of the gel. Each small square indicates the location of the feature and the large rectangles are zoomed in versions of the indicated square. Due to the large area this image is stitched together from several individual images. . . .	63
4.3	Map of the spatial intensity of a Gaussian focused beam made by solving Equation 4.1	65
4.4	Spatial map of absorbed energy made by solving Equation 4.6	67
4.5	Map of the void shape assuming $E_c=80$ pJ/molecule.	68

4.6	Plot showing estimated void volumes given various imaging exposure times. The dotted line indicates the average for each laser exposure condition. Error bars represent 1 standard deviation (n=3). Decrease in volume at 20 ms is due to pixel saturation.	71
4.7	Schematic diagram of background-free autocorrelator for ultra-short pulse measurement. The incoming beam is split into two arms one of which moves periodically. The beams are interfered inside a second harmonic generating crystal. When the pulse copies overlap the SHG intensity is at a maximum.	73
4.8	Raw SHG signal (points) and Gaussian fit to those points (line) of a ~ 160 fs pulse.	74
4.9	Change in transmitted power with displacement of a $2.5 \mu\text{m}$ FWHM spot measured with a power meter (points) and a Gaussian fit of the data (line).	76
4.10	Qualitative view of the laser produced features (A), the segmented laser produced features (B), and the simulated voids (C).	77
4.11	Measured feature volumes (points) and the simulated volumes (lines) for varying pulse energies and exposure times. Volumes were calculated using $E_c = 71$ pJ/molecule. Note that the x-axis is presented on a log scale. Error bars are +/- one standard deviation (n=6).	78
4.12	Plot showing the weighted root mean squared error as a function of critical energy. The best fit of E_c to the data is found where the error is minimized.	79

4.13	Results of splitting the 6 gels into groups of 3. Half the data was used as a training set to determine E_c and then fit to the other half of the data.	80
4.14	Plot showing normalized void size upon exposure to different wavelengths of light. Voids were normalized to 810 nm and error bars indicate +/- 1 standard deviation (n=3).	81
4.15	Simulated effect of pulse width on void size. Model assumed 10 nJ pulses exposed for 10 s.	82
4.16	Simulated effect of the spot size and pulse energy on void volume. As pulse energy increases the optimal spot size for maximum material removal shifts to less tight focusing indicating a trade off between high optical intensity and large focal volume.	83
4.17	Computer generated hologram of 3rd order Laguerre-Gaussian beam interfering with a plane wave (left). The same pattern micromachined into a silk film (right).	84
4.18	Photograph showing the diffraction pattern when a laser is passed through the patterned silk film shown in Figure 4.17.	84
5.1	Linear absorption spectrum of silk gel with background subtracted. The vertical line at 810 nm indicates the wavelength used for multiphoton micromachining. Pump/2 and Pump/3 lines indicate, roughly, the wavelengths associated with a 2-photon and 3-photon absorption process respectively. Linear absorption is driven by tyrosine and tryptophan residues in the silk. Spectrum was filtered by a 5-point moving average to reduce noise.	91

5.2 Overview of the micromachining process. (a) Schematic of the multiphoton micromachining workstation. The shutter and translation stage are both computer controlled. Inset: Photograph of the silk hydrogel showing high transparency. (b) 3D AFM image of one of the lines in panel (d). (c) Graph relating line dimensions with pulse energy. Error bars represent 1 standard deviation (n=4). (d) Microphotograph of lines machined into the upper surface of a silk gel at pulse energies ranging from 0.25 nJ (bottom) to 5 nJ (top). (e) End on view of 30 μm wide lines machined into a silk gel. Light was incident from the bottom of the image. Ruler on right side measures depth from the surface of the sample. Smearing at greater depth was caused by a reduction in write speed resulting in longer exposure time and a greater area of modification. The break in the pattern on the top was due to limits on the vertical travel of the microscope. Due to the large area involved, this image was stitched together from a series of microphotographs. Inset: detail of the cross-section of one line. 93

5.3 Amplified laser pulses incident from the bottom were used to create voids in the silk hydrogels at various pulse energies. Symmetrical features using 1 μJ pulses (left) indicate that self-focusing is negligible. Strong self-focusing effects are evident in the asymmetrical shape from 10 μJ pulses (center) and 20 μJ (right) pulse energies. All features were made by a single pulse at each location 95

- 5.4 An overview of two test patterns machined into the gel. (a) 3D model of a helical pattern input into the control program. (b) Confocal microscope image of a cross section of the helix showing the machined region in black. Scale bar represents 100 μm (c) Reslice of the confocal stack along the dashed line in panel (b). Scale bar represents 100 μm (d) 3D reconstruction of the segmented confocal data showing the machined feature. (e) 3D model of a branching pattern input into the machining control program. (f) 3D reconstruction of resulting machined region made by segmenting the confocal images. (g) Confocal slice showing a cross section of the micromachined region Scale bar represents 100 μm and also applies to panels h and i. (h-i) Cross-sections of the confocal volumes at the indicated lines. 96
- 5.5 Confocal cross section (left) of the vascular like pattern described in Fig. 5.4 using only the autofluorescence of silk fibroin for contrast. An increase in autofluorescence can be appreciated immediately surrounding the machined region which suggests that an increased density of silk is present in those locations. The right two panels are re-slices of the confocal stack along the indicated lines. The scale bar applies to all panels 97

5.6 Micromachined features *in vitro*. (a-d) Machined lines on the surface of a gel at day 1, 3, 5, and 8 respectively. Arrows indicate cells growing along the machined lines. Panel (d) shows fluorescently labeled cells growing in the lines. The scale bar is 100 μm long. Panel (d) shows a slightly different region of the gel as high cell density obscured the features at the location of the other images. (e) Cartoon showing micromachining of a gel laden with hMSCs (not to scale). Inset: Brightfield image of the machined region. Scale bar represents 250 μm . (f-h) Confocal images of the cell laden gel following live/dead staining 76 μm below, 62 μm above, and in the plane of machining respectively. Dashed lines outline the micromachined region. Scale bar represents 250 μm . (i-j) Close-up of living cells irradiated by the beam above (i) and below (j) the focal plane. 99

5.7 Cell infiltration into machined features. (a) Top: 3D model of the pattern machined into hydrogels that were subsequently seeded with cells *in vitro*. (a) Bottom: Series of confocal images of fibroblasts growing within a Y-shaped machined feature on day 9 after seeding. Each image is separated by 10 μm in the Z-direction. Scale bar indicates 100 μm (b) Top: 3D model of the pattern machined into a hydrogel that was subsequently implanted subcutaneously in mice. Lines marked (i-iii) indicate the confocal cross-sections shown in the panels below. The white circles in (i) and (ii) correspond to the main branch diameter and approximate location in the construct. The smaller circles in (iii) correspond to the secondary branch diameters. Cells had infiltrated to the bottom of the main branch (ii) and had begun extending down one of the secondary branches (iii). All scale bars represent 100 μm 101

6.1 Panel A: schematic representation of the construction of silk optical waveguides. To fabricate the core, silk solution is cast into molds (1A) and allowed to dry into films (1B). For the cladding, HRP and H₂O₂ are added to a silk solution (1B) and aspirated into a PTFE tube (2B). Prior to gelation, the film is inserted into the liquid gel precursor (3). After the gel precursor solidifies, pressure on the syringe ejects the completed waveguide (4). Panel B: photograph of a 9 cm long silk waveguide coupled to a glass optical fiber knotted to show flexibility. Scale bar indicates 1 cm. Inset: Brightfield microscope image of a cross-section of a 3 mm diameter silk waveguide. Scale bar indicates 1 mm. Arrow indicates the silk film core which is 2.9 mm wide and $\sim 40 \mu\text{m}$ thick. 115

6.2 Top: Plot showing transmitted power as a function of distance from the coupling fiber. Y-axis is presented on a log scale so the straight line of the data indicates an exponential decline in transmitted power with a consistent decay constant. Error bars indicate 1 standard deviation, n=4. Bottom: Calculated loss per centimeter as a function of distance from the tip of the coupling fiber. High loss near the tip of the coupling fiber is likely due to unguided modes. Error bars indicate 1 standard deviation, n=4. 118

6.3 Silk waveguide guiding light in tissue. Light coupled from multimode glass fiber is confined within the silk film core of a 3.5 cm long waveguide. Inset shows the core of the waveguide glowing green after closure of the incisions. 119

7.1	Cartoon depicting experimental set-up for monitoring evolution of gel stiffness. 3, 450 nm LEDs were equally spaced around the rheometer shaft and illuminated the sample with an intensity of 18.7 mW/cm ² . Green region indicates the fluorescent silk solution during crosslinking.	129
7.2	Plot showing the evolution of stiffness during illumination (white bars) and with the light off (black bar). The gel stops stiffening when light is removed.	130
7.3	Effect of different compounds on gelation rate after illumination for 1 hour. Shear modulus values are recorded for silk dissolved in deionized water (H ₂ O), deuterated water (D ₂ O), sodium azide (NaAz), and superoxide dismutase (SOD). Negative controls -RF and -Light were tested without riboflavin and without illumination respectively. Shear modulus is presented on a log scale. NS indicates a non-significant difference. All other pairs of values were significant with $p < 0.001$. N=4 for treatment groups and N=3 for control groups. All data are plotted as points with bars representing the mean of each group.	131
7.4	Fluorescence spectra of 3 solutions after 60 minutes of illumination by 450 nm light. Silk alone (black) shows no fluorescence, un-rinsed silk gels have a small dityrosine peak at 410 nm and a small riboflavin peak at 530 nm, rinsed silk gels have a strong dityrosine peak and no evidence of riboflavin fluorescence. Dark lines indicate the means of 8 samples with the standard deviations at each wavelength indicated by the shaded regions. . . .	133

7.5	Brightfield microscope image of a high-resolution pattern of silk gel produced by photolithography. Blue light was passed through a photomask and used to illuminate a mixture of silk and riboflavin. Using this setup, silk could be patterned with a resolution of $\sim 20 \mu\text{m}$	134
7.6	Schematic representation of riboflavin adherence for vision correction. Silk films doped with riboflavin are applied to a diseased eye. Following illumination, silk is selectively adhered to the eye surface. The unexposed silk can be rinsed away leaving behind an eye altered to correct vision.	134
7.7	Representative OCT images of silk films applied to deepithelialized enucleated porcine eyes. Top row: Riboflavin impregnated silk. Blue arrows indicate the layer of silk overlying the corneal collagen. Red arrows on right side indicate air bubbles in the silk prior to illumination causing shadowing. Short green arrows indicate specular reflection artifacts in the OCT image. Bottom row: Images of control film without riboflavin.	135

7.8	Silk thickness measured in 32 locations on each eye prior to application to the eye, immediately after application to the eye, following light exposure, and following a rinse with PBS. Films without riboflavin (CON) and films not exposed to light (RNL) show no ability to withstand rinsing. Riboflavin impregnated silk films exposed to light (RFL) are able to adhere to the corneal surface. All measurements are displayed. Data from individual eyes is indicated by a different shade. Heavy bars indicate the mean of all the data in that group. Stars indicate statistical significance between groups ($p < 0.05$). $n=6$ for CON and RFL, $n=4$ for RNL.	136
7.9	Histologic sections of porcine cornea treated with riboflavin doped silk films. Top: silk gels were not exposed to light and washed away. Bottom: Silk gel was illuminated and formed close association with corneal collagen.	137
7.10	Silk gels modified by excimer laser excitation. Silk hydrogels produced by horseradish peroxidase (right) or riboflavin (left) were exposed to 36 pulses each of 193 nm excimer light from a commercial PRK machine. The region of modification closely matched the spot size indicating that such gels are amenable to shaping by excimer emissions.	138
7.11	Optimizing riboflavin concentration. Top: plot showing evolution of stiffness of silk solutions containing various concentrations of riboflavin. Bottom: Numerical derivative of top plot showing that the steady-state rate of gelation is highest at a concentration of 2 mM.	140

8.1 Fluorescence image of riboflavin photocrosslinked with ultra-
short pulses of NIR light. Bright dots indicate the presence of
riboflavin only in the regions exposed to light. 156

Sculpting with light:
light/matter interactions in biocompatible polymers

Chapter 1

Introduction

The use of light in medicine traces its roots back to prehistoric times. By observing the light reflected from their patients, early doctors could see the redness of an infection, the purple of a bruise, or anomalous lumps that could indicate a tumor. Over time, the use of light in medicine has become far more sophisticated. We have learned to use light invisible to the naked eye such X-rays to see broken bones, and radio waves emitted by malignancies when exposed to varying magnetic fields. These devices have enabled diagnoses to be made with unprecedented speed and accuracy. The utility of light in medicine comes from its ability to interact with biological material. The way tissues change or distort the light can provide valuable clues as to the state of that tissue's health. However, this is not a one-way process. Biological materials can not only change light, but can be changed by light. Such modification is evident in the case of a sunburn in which exposure to ultraviolet radiation damages DNA in the skin. By harnessing the ability of light to change biological materials tremendous advances in the treatment of disease can be realized.

In this dissertation three types of light/matter interactions are presented with applications ranging from tissue engineering to ocular prostheses. The first involves harnessing the strong nonlinear absorption of silk to photostruc-

ture hydrogels in three-dimensions via multiphoton absorption. The second uses riboflavin (vitamin B2) to cross-link silk fibroin in the presence of light. The third takes advantage of the transparency of silk to guide light within scattering tissue. In this chapter, the importance of 3D structured materials for biomedical applications is introduced and techniques for creating such materials using light are reviewed. In Chapter 2 the theory of multiphoton absorption of light is outlined including a discussion of how ultrashort pulses are generated via mode locking. Chapter 3 describes work measuring the 3-photon absorption cross-section of silk fibroin using the Z-scan technique. In Chapter 4 a finite-element model of modification of soft silk hydrogels using ultrashort pulses is described. This chapter shows that void formation in silk hydrogels is not governed by diffusion of heat or other photoproducts, but can be described solely by the direct absorption of light energy. The use of ultrashort pulses to ablate solid silk films is also briefly discussed. Chapter 5 shows how large-scale (~ 0.5 mm) structures can be formed in silk hydrogels and how these structures can be used to guide cellular infiltration both *in vitro* and *in vivo*. In Chapter 6 a method of creating step-index optical waveguides by encapsulating a silk film within a silk hydrogel is described that enables visible light to be delivered through scattering media such as tissue. Chapter 7 investigates the mechanism by which linear absorption of light from inexpensive light-emitting diodes by riboflavin can be used to crosslink silk to form a hydrogel, and the results of a pilot experiment to use such gels as ocular prostheses for the treatment of myopia and corneal ectatic disorders is discussed. Finally, in Chapter 8 conclusions are drawn based on this work and possible future directions are described.

1.1 Structuring soft materials

Most biological tissue is relatively soft compared to the metals, plastics, and ceramics of consumer products. With the exception of bone, the average elastic modulus for soft tissue generally falls in the range of 5-5000 kPa [1]. This is in sharp contrast to most engineering materials which typically have elastic moduli nearly six orders of magnitude larger (1-100 GPa) [2]. Traditional manufacturing technologies have focused on shaping these stiff materials, but are unsuitable for work with soft materials comparable to human tissue. Attempting to apply conventional milling technologies to soft materials almost invariably results in material damage. Currently, there are very few techniques to shape soft materials with high resolution. The most well-known is soft lithography in which a liquid precursor is poured onto a patterned substrate and allowed to cure into a solid. Once cured, the pattern from the substrate is transferred to the material [3]. While this technique is capable of generating patterns with features as small as 30 nm, it is a two dimensional technique. To make 3D structures using lithography, multiple 2D layers must be produced, aligned, and stacked, a time-consuming and laborious process. Photolithography is also possible on certain soft materials, but has similar limitations to soft-lithography.

Only recently has it become possible to pattern soft materials in three-dimensions. Typically, light is used to crosslink a liquid monomer to create a 3D shape (section 1.3.1). However, as detailed in Chapter 4, light can also be used to induce a phase transition within a soft material leaving behind a void. This technique allows for the creation of arbitrary 3D patterns in soft materials that are extremely difficult or impossible to produce using other techniques. For large 3D patterns to be produced, the material must be transparent enough for a focal spot to be formed at the desired depth. However, 3D structures

can be produced in most biological materials so long as the depth below the surface is limited to a few hundred microns [4]. 3D structuring of soft materials is critical for the field of tissue engineering where complex cell scaffolds must be crafted from materials with mechanical properties that mimic soft tissue.

1.2 Photomodification

The photomodification of a material begins with the absorption of a photon. The photons transfer energy to the material and can induce changes through a variety of mechanisms (e.g. temperature increase or chemical modification). The result of the change can be an ablative event in which the material transitions from liquid or solid to a gas; a solidification in which liquids form solids or gels; or a melting event where solids turn to liquids. Using light to induce these modifications has several key advantages over other techniques commonly used to shape materials. Most importantly, light can be controlled higher spatial precision than nearly any mechanical system. Using inexpensive lenses and lasers, beams of light can be focused to spots $\sim 5 \mu\text{m}$ in diameter. More advanced techniques have enabled the selective polymerization of photoresists with resolutions on the order of 10 nm [5]. This technology has been perfected by the computer chip industry and has resulted in the vast increase in computing power and decreasing size of consumer electronics. In addition to precision, light is attractive because it is a non-contact technique. Unlike methods such as drilling or milling where the tool needs to come in contact with the workpiece in order to change its structure, the physical impact of light on condensed matter is minimal making it suitable for use in fragile materials. Light is also attractive for biomedical applications because it is relatively safe for biological tissue. Nearly all life on earth evolved in the presence of high

intensity visible light from the sun which forced organisms to develop a high tolerance for such radiation. For many biomedical applications near infrared (NIR) light is used to which most biological tissues are relatively transparent. Using these wavelengths, even at quite high intensities, little energy is deposited in the tissue, minimizing potential harm. This transparency allows the use of femtosecond pulses of light with peak intensities of Terawatts per square centimeter to be used to perform surgery. At the focus of the beam, energy is deposited resulting in cell death, but cells in the cone of light both upstream and downstream of the focal plane are relatively unaffected (Chapter 5 and Ref. [6]). Water is also minimally absorbing in the NIR forming a “window” of wavelengths that are particularly suited to biomedical applications [7].

1.3 Importance of 3D structures in medicine

Every cell in the body exists in a three-dimensional extracellular matrix. Yet, for decades, experiments on human cells involved culturing them in two-dimensions often on relatively stiff substrates such as polystyrene. Recently, new materials, and advances in 3D structuring, have enabled the exploration of 3D cell culture *in vitro*, though in this case the term *in vitro* which means literally “in glass”, may no longer strictly apply. This transition to soft 3D cell scaffolds has allowed researchers to observe markedly different receptor expression, transcriptional expression, cellular migration, and apoptosis of cells compared with culture on flat substrates [8]. Differences in differentiation of stem cells have also been observed based on mechanical cues from the growth matrix [9]. In 2D culture, cells experience less resistance to migration due to the lack of a surrounding extracellular matrix that can limit self-organization

[10]. The use of 3D cell culture techniques has elucidated the importance of both cell-cell and cell-matrix communication in the proliferation and differentiation of cells. Soft hydrogels with high water content have been identified as promising materials for 3D cell culture [10].

The field of tissue engineering seeks to recapitulate the natural complexity of the human body artificially. In order to do so, complex 3D cell scaffolds are needed to provide niches for different cell types, vascular structures to feed active cells, as well as ducts and glands to export hormones and other metabolic products. Numerous strategies have been investigated to achieve cell scaffolds complex enough to support organ-specific cell types with sufficient mass transport to ensure cell survival at high densities. One attractive strategy for forming 3D cell scaffolds is 3D printing (also known as additive manufacturing or solid free-form fabrication). A full review of all the 3D structuring techniques available is beyond the scope of this dissertation, but here the focus is on methods of 3D structuring materials using light, and 3D structuring modalities that are suitable for patterning biocompatible materials. Where available, biomedical applications of each of these technologies are highlighted.

1.3.1 Light-based methods of creating 3D structures

The first light-based 3D patterning technology was stereolithography (SLA) which was developed in the 1986 [11]. This technology used materials that solidify when exposed to ultraviolet (UV) radiation. The SLA system works in a layer-by-layer fashion in which cross-sections of the object are serially created one on top of the other to build up a 3D structure. The key components of a SLA system are a reservoir of UV-curing resin, a platform capable of being raised and lowered, a way to reliably spread new UV curing resin over the

surface of the part, a method of controlling the illumination such as a laser scanning system or digital mirror array, and a light source. To create a 3D structure the spreader spreads a thin film of UV-curing resin over the platform. The light source is energized and the thin layer of resin is selectively exposed to the light to solidify it. The platform descends and a fresh layer of resin is spread over the part. Once all the layers are built up, the part is removed and excess resin washed away. Most SLA systems make use of a second curing step to ensure that the resin has been fully cured. The resolution of this process is limited in the plane of illumination by the resolution of the mask or tightness of focusing, and in height by the minimum thickness of the UV-resin that can be reliably spread. There is a trade-off between the achievable resolution and the size of the finished part. Large parts (~ 10 cm) can be produced with resolutions of ~ 200 μm using low-cost commercially available desktop SLA printers [12]. Micro-stereolithography (μ -SLA) systems are capable of making small parts with 1.2 μm resolution [13]. Two-photon polymerization allows even higher resolutions and is described later in this chapter.

SLA has seen application in the field of mandibular reconstruction. Using medical imaging, perfectly complimentary facial prostheses can be printed and implanted following tumor resection [14]. This has the advantage of being customized to the patient which ensures a better fit than off the shelf components. UV curing materials can be fabricated in a wide range of stiffnesses from 200 MPa [15] to poly(ethylene glycol) diacrylate hydrogels that can be as soft as 4 kPa [16]. In these soft hydrogels, cells can be mixed into the pre-cured solution and are able to survive the curing process [16, 17]. These materials show promise for tissue engineering applications [18].

Selective laser sintering (SLS) is a 3D patterning technique similar to SLA except it uses powdered materials as a substrate rather than a liquid resin. A

thin layer of powder is spread over a stage and a laser is used to fuse the powdered grains together. The laser energy is carefully controlled to prevent the powdered material from fully melting. After each layer the stage descends and a new layer of powder is spread over the part. While originally used to produce metal parts [19], this technique has also been used to create 3D structures from a wide variety of other materials such as poly(d,l)-lactic acid [20], polycaprolactone [21], polyvinyl alcohol/hydroxyapatite [22], polyamide [23], and cellulose [24]. Similarly to SLA these materials tend to be quite stiff so this technique is typically used to engineer scaffolds for bone tissue regeneration. Due to the dry environment and high temperatures involved, this technique is not suitable for direct cell encapsulation, but rather relies on cell seeding after fabrication for creation of artificial tissues. Porous titanium and nitinol scaffolds have been produced using this technique that are biocompatible, will not degrade over time, and allow for the ingrowth of native, functioning, cells [25].

Direct metal laser sintering (DMLS), and selective laser melting (SLM) are nearly identical to SLS in that they use a laser to fuse together grains of a powdered material. As the name suggests DMLS is essentially SLS, but is restricted to metal powders. DMLS, since the material is never fully melted, can be used for alloys as well as pure metals. In SLM, however, the grains are heated until they melt into a homogeneous material. This technique is preferable when working with pure metals as it leaves behind a smoother surface than SLS [26]. The resolution of these systems is limited by the spot size of the laser and the minimum thickness of powdered metal that can be spread over the surface. An important advantage of these techniques is that the part is always fully surrounded and supported by the powdered metal bed during fabrication. This obviates the need for removable supporting structures that

may be required with SLA systems. Once the part is finished it can be removed from the device and the remaining powdered metal reused to make the next part. In the biomedical field, SLS and SLM have attracted interest for making artificial bones due to the strength of the finished parts. Using these systems, joint replacements can be crafted from existing bone based on 3D imaging modalities such as X-ray computed tomography. Because the metal is fully melted in SLM the finished parts have higher surface quality and lower porosity than SLS making it suitable for applications where mechanical strength is more important than cellular infiltration [27]. Despite this, porous metal structures have been created using SLM that can support cellular ingrowth [28, 29] Using biocompatible metals, this process could also be suitable for complex dental prostheses [30].

SLA, SLS, and similar technologies have somewhat limited spatial resolution. To make extremely fine features, holographic techniques can also be used to form 3D structures in amenable materials [31]. A hologram is produced by the interference of two identical beams of light, one of which has interacted with an object. The result is a 3D interference pattern which, when projected into a photocrosslinkable substrate, will create a solid replica of the pattern. This technique is capable of rapidly patterning large areas with a maximum resolution of half the wavelength of light used. Interestingly, this technique can also be applied to electron beams [32] which, due to their extremely short wavelength, can be used to create structures with nanometer resolution [33]. Holographic photolithography is well suited to creating periodic structures such as photonic crystals, but lacks the ability to create arbitrary structures possible with stereolithography and SLS/SLM.

Two-photon polymerization (2PP) is another technique for creating 3D structures using light. This process takes advantage of the intensity-dependent

nature of multiphoton absorption. In 2PP a pulsed laser is used to create a beam with extremely high peak power. In the focal volume, the high photon density allows the material to absorb wavelengths to which it is normally transparent. Using ultrashort (< 200 fs) pulses two (or more) low energy photons can be absorbed simultaneously such that their combined energy exceeds the band gap in the material. When this happens energy is transferred to the lattice which can result in localized material modification. Further details on multiphoton absorption can be found in Chapter 2. The amount of energy absorbed in a two-photon absorption process is proportional to the intensity of light squared. This means that by carefully controlling the pulse energy and the focusing conditions volumes smaller than the diffraction limited spot can be directly addressed (Figure 1.1). If two-photon absorption occurs in a material that polymerizes when exposed to light it is possible to solidify almost arbitrarily small volumes of the polymerizable resin [34, 35, 36]. Resolution can be further improved by using a shaped depletion beam to reduce the volume of interaction in a manner analogous to stimulated emission depletion (STED) microscopy [37]. 2PP has been used to create cell scaffolds and to produce chemical gradients in hydrogels to guide cell migration and behavior [38, 39].

Direct laser writing (DLW), unlike the previous methods discussed, is a subtractive technique to write 3D structures inside solid materials. Like 2PP, this technique utilizes multiphoton absorption of light to modify a substrate. However, DLW is not limited to photopolymerizable resins. Rather, given sufficient intensity almost any material can be patterned by DLW. Formation of sub-diffraction limited structures within materials is also possible by tuning the intensity of the beam such that only a small portion of it is above the threshold intensity needed to initiate multiphoton absorption. DLW has been

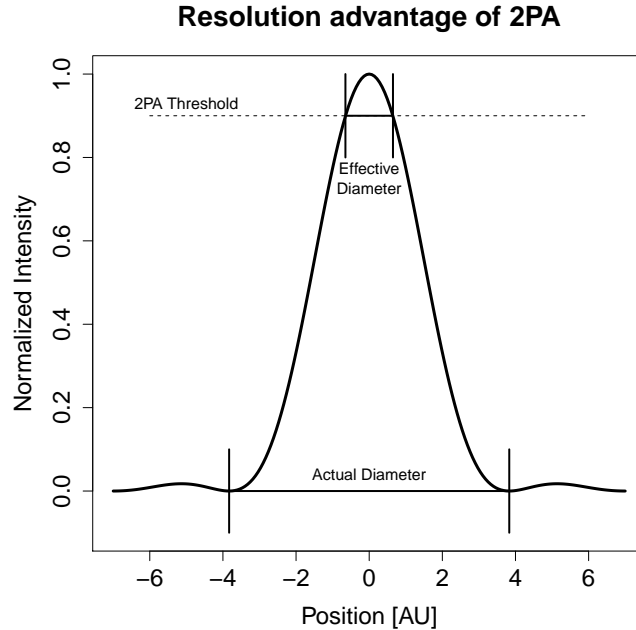


Figure 1.1: Simulated intensity distribution of a focused beam where only the central region is above the threshold for two-photon absorption. This illustrates how regions smaller than the diffraction limited spot can be addressed.

extensively investigated in quartz and borosilicate glass. In these materials focused ultrashort pulses can form high density structures in glass which can be used as waveguides [40, 41, 42], as well as a wide range of optical devices [43]. The ability to pattern waveguides and other optical devices in 3-dimensions holds particular promise for optical computing and integrated photonics applications. Such a system could allow easy coupling of light from an external source onto an optical computer chip without the need for fragile and difficult to handle optical fibers. DLW has also been applied to materials with photolabile bonds. Upon exposure to light the material will depolymerize leaving behind a void. This strategy has been used to promote cell spreading and attachment [44].

A final technique for creating 3D structures using light that will be described is laser induced forward transfer (LIFT). This technique uses a pulsed

laser focused onto a metal ribbon coated with the material to be printed. When a pulse hits the metal it vaporizes launching a piece of the ribbon's coating onto a collection substrate. The ribbon can be coated with a wide variety of substances including hydrogels [45], enzymes, DNA, and living cells without significant damage [46, 47]. Though the height of features that can be produced using this technique is limited, recent work has demonstrated the ability to build high aspect ratio 3D structures by sequentially launching pieces of copper or silver at the same location to form a tower [48]. This technique has been used in biomedical applications to seed multiple cell types in different locations on a 3D scaffold [49]. While true 3D patterning of biological material using LIFT has yet to be realized, it is a powerful quasi-2D technique for building up layers of biomaterials.

1.4 Conclusion

Recent years have seen a huge upsurge in the number and popularity of 3D structuring modalities. These technologies are poised to revolutionize fields as diverse as airplane manufacturing and medical prostheses. However, true 3D printing in a soft, biocompatible material with high resolution remains challenging. Such a technique would allow the production of custom cell scaffolds with complex biofunctional architecture. In the next several chapters photostructuring of silk fibroin using ultrashort pulses of near infrared light is described and the use of this structuring to create complex, high-resolution patterns suitable for guiding cells *in vitro* and *in vivo* explored. In chapter 7 a method for photocrosslinking silk using riboflavin as a photoinitiator to create 2D structures and conformally attach silk to corneal collagen is presented. Preliminary results indicate that this method is suitable for ocular prostheses

which can alter the curvature of the eye and correct common vision problems such as myopia. In the next chapter, the theoretical foundations of ultrashort pulse generation and the interaction of these pulses with matter are reviewed.

Bibliography

- [1] C. T. McKee, J. a. Last, P. Russell, and C. J. Murphy, “Indentation versus tensile measurements of Young’s modulus for soft biological tissues.,” *Tissue engineering. Part B, Reviews*, vol. 17, no. 3, pp. 155–164, 2011.
- [2] C. Hartsuijker and J. W. Welleman, *Engineering Mechanics, Vol. 2*. Dordrecht: Springer, 2007.
- [3] G. M. Xia, Younan; Whitesides, “Soft Lithography,” *Angewandte Chemie - International Edition*, no. 12, 1998.
- [4] M. Oujja, S. Pe’rez, E. Fadeeva, J. Koch, B. N. Chichkov, and M. Castillejo, “Three dimensional microstructuring of biopolymers by femtosecond laser irradiation,” *Applied Physics Letters*, vol. 95, no. 26, p. 263703, 2009.
- [5] B. Wu and A. Kumar, “Extreme ultraviolet lithography: A review,” *Journal of Vacuum Science & Technology B: Microelectronics and Nanometer Structures*, vol. 25, no. 6, p. 1743, 2007.
- [6] J. P. Mondia, D. S. Adams, R. D. Orendorff, M. Levin, and F. G. Omenetto, “Patterned femtosecond-laser ablation of *Xenopus laevis* melanocytes for studies of cell migration, wound repair, and developmental processes.,” *Biomedical optics express*, vol. 2, no. 8, pp. 2383–2391, 2011.

- [7] R. Weissleder, “A clearer vision for in vivo imaging.,” 2001.
- [8] J. W. Haycock, “3D Cell Culture: A Review of Current Approaches and Technique,” in *3D Cell Culture: Methods and Protocols*, vol. 695, pp. 1–15, 2011.
- [9] D. Huh, G. a. Hamilton, and D. E. Ingber, “From 3D cell culture to organs-on-chips,” *Trends in Cell Biology*, vol. 21, no. 12, pp. 745–754, 2011.
- [10] M. W. Tibbitt and K. S. Anseth, “Hydrogels as extracellular matrix mimics for 3D cell culture,” *Biotechnology and Bioengineering*, vol. 103, no. 4, pp. 655–663, 2009.
- [11] F. Melchels, J. Feijen, and D. Grijpma, “A review on stereolithography and its applications in biomedical engineering,” *Biomaterials*, vol. 31, no. 24, pp. 6121–6130, 2010.
- [12] Formlabs, “Formlabs form2 3D printer,” 2015.
- [13] X. Zhang, X. N. Jiang, and C. Sun, “Micro-stereolithography of polymeric and ceramic microstructures,” *Sensors and Actuators, A: Physical*, vol. 77, no. 2, pp. 149–156, 1999.
- [14] A. Cohen, A. Laviv, P. Berman, R. Nashef, and J. Abu-Tair, “Mandibular reconstruction using stereolithographic 3-dimensional printing modeling technology.,” *Oral surgery, oral medicine, oral pathology, oral radiology, and endodontics*, vol. 108, pp. 661–6, nov 2009.
- [15] M. N. Cooke, J. P. Fisher, D. Dean, C. Rimnac, and A. G. Mikos, “Use of stereolithography to manufacture critical-sized 3D biodegradable scaffolds

- for bone ingrowth.” *Journal of biomedical materials research. Part B, Applied biomaterials*, vol. 64, no. 2, pp. 65–69, 2003.
- [16] V. Chan, P. Zorlutuna, J. H. Jeong, H. Kong, and R. Bashir, “Three-dimensional photopatterning of hydrogels using stereolithography for long-term cell encapsulation,” *Lab on a Chip*, vol. 10, no. 16, p. 2062, 2010.
- [17] L. Elomaa, C.-C. Pan, Y. Shanjani, A. Malkovskiy, J. V. Seppälä, and Y. Yang, “Three-dimensional fabrication of cell-laden biodegradable poly(ethylene glycol-co-depsipeptide) hydrogels by visible light stereolithography,” *J. Mater. Chem. B*, vol. 3, no. 42, pp. 8348–8358, 2015.
- [18] V. Chan, J. H. Jeong, P. Bajaj, M. B. Collens, T. A. Saif, H. Kong, and R. Bashir, “Multi-material bio-fabrication of hydrogel cantilevers and actuators with stereolithography,” *Lab on a Chip*, vol. 12, no. 1, pp. 88–98, 2012.
- [19] A. Mazzoli, “Selective laser sintering in biomedical engineering,” *Medical & Biological Engineering & Computing*, vol. 51, no. 3, pp. 245–256, 2013.
- [20] J. M. Kanczler, S.-H. Mirmalek-Sani, N. a. Hanley, A. L. Ivanov, J. J. a. Barry, C. Upton, K. M. Shakesheff, S. M. Howdle, E. N. Antonov, V. N. Bagratashvili, V. K. Popov, and R. O. C. Oreffo, “Biocompatibility and osteogenic potential of human fetal femur-derived cells on surface selective laser sintered scaffolds,” *Acta biomaterialia*, vol. 5, no. 6, pp. 2063–71, 2009.
- [21] J. M. Williams, A. Adewunmi, R. M. Schek, C. L. Flanagan, P. H. Krebsbach, S. E. Feinberg, S. J. Hollister, and S. Das, “Bone tissue engineering

- using polycaprolactone scaffolds fabricated via selective laser sintering,” *Biomaterials*, vol. 26, no. 23, pp. 4817–4827, 2005.
- [22] C. K. Chua, K. F. Leong, K. H. Tan, F. E. Wiria, and C. M. Cheah, “Development of tissue scaffolds using selective laser sintering of polyvinyl alcohol/hydroxyapatite biocomposite for craniofacial and joint defects,” *Journal of Materials Science: Materials in Medicine*, vol. 15, no. 10, pp. 1113–1121, 2004.
- [23] S. Kenzari, D. Bonina, J. Dubois, and V. Fournée, “Quasicrystal–polymer composites for selective laser sintering technology,” *Materials & Design*, vol. 35, pp. 691–695, 2012.
- [24] G. V. Salmoria, P. Klauss, R. a. Paggi, L. a. Kanis, and A. Lago, “Structure and mechanical properties of cellulose based scaffolds fabricated by selective laser sintering,” *Polymer Testing*, vol. 28, no. 6, pp. 648–652, 2009.
- [25] I. V. Shishkovsky, L. T. Volova, M. V. Kuznetsov, Y. G. Morozov, and I. P. Parkin, “Porous biocompatible implants and tissue scaffolds synthesized by selective laser sintering from Ti and NiTi,” *Journal of Materials Chemistry*, vol. 18, no. 12, p. 1309, 2008.
- [26] J. Kruth, L. Froyen, J. Van Vaerenbergh, P. Mercelis, M. Rombouts, and B. Lauwers, “Selective laser melting of iron-based powder,” *Journal of Materials Processing Technology*, vol. 149, no. 1-3, pp. 616–622, 2004.
- [27] S. Amin Yavari, R. Wauthle, J. van der Stok, A. Riemsdag, M. Janssen, M. Mulier, J. Kruth, J. Schrooten, H. Weinans, and A. A. A. Zadpoor, “Fatigue behavior of porous biomaterials manufactured using selective

- laser melting,” *Materials Science and Engineering: C*, vol. 33, no. 8, pp. 4849–4858, 2013.
- [28] L. Mullen, R. C. Stamp, P. Fox, E. Jones, C. Ngo, and C. J. Sutcliffe, “Selective laser melting: A unit cell approach for the manufacture of porous, titanium, bone in-growth constructs, suitable for orthopedic applications. II. Randomized structures,” *Journal of Biomedical Materials Research - Part B Applied Biomaterials*, vol. 92, pp. 178–188, 2010.
- [29] D. K. Pattanayak, A. Fukuda, T. Matsushita, M. Takemoto, S. Fujibayashi, K. Sasaki, N. Nishida, T. Nakamura, and T. Kokubo, “Bioactive Ti metal analogous to human cancellous bone: Fabrication by selective laser melting and chemical treatments,” *Acta Biomaterialia*, vol. 7, no. 3, pp. 1398–1406, 2011.
- [30] B. Vandenbroucke and J.-P. Kruth, “Selective laser melting of biocompatible metals for rapid manufacturing of medical parts,” *Rapid Prototyping Journal*, vol. 13, no. 4, pp. 196–203, 2007.
- [31] a. J. Turberfield, “Fabrication of photonic crystals for the visible spectrum by holographic lithography,” *Nature*, vol. 404, no. March, pp. 53–56, 2000.
- [32] K. Ogai, Y. Kimura, R. Shimizu, J. Fujita, and S. Matsui, “Nanofabrication of grating and dot patterns by electron holographic lithography,” *Applied Physics Letters*, vol. 66, no. 12, p. 1560, 1995.
- [33] R. E. Dunin-Borkowski, T. Kasama, A. Wei, S. L. Tripp, M. J. Hytch, E. Snoeck, R. J. Harrison, and A. Putnis, “Off-axis electron holography of magnetic nanowires and chains, rings, and planar arrays of magnetic nanoparticles,” *Microscopy Research and Technique*, vol. 64, no. 5-6, pp. 390–402, 2004.

- [34] J. Serbin, A. Ovsianikov, and B. Chichkov, “Fabrication of woodpile structures by two-photon polymerization and investigation of their optical properties.,” *Optics express*, vol. 12, pp. 5221–8, oct 2004.
- [35] L. L. Erskine, A. a. Heikal, S. M. Kuebler, M. Rumi, X.-l. Wu, S. R. Marder, and J. W. Perry, “Two-photon polymerization initiators for three- dimensional optical data storage and microfabrication,” *Solid State Physics*, vol. 398, no. March, pp. 51–54, 1999.
- [36] M. Deubel, G. von Freymann, M. Wegener, S. Pereira, K. Busch, and C. M. Soukoulis, “Direct laser writing of three-dimensional photonic-crystal templates for telecommunications,” *Nature Materials*, vol. 3, no. 7, pp. 444–447, 2004.
- [37] J. Fischer and M. Wegener, “Three-dimensional direct laser writing inspired by stimulated-emission-depletion microscopy,” *Optical Materials Express*, vol. 1, no. 4, pp. 2363–2366, 2011.
- [38] S.-H. Lee, J. J. Moon, and J. L. West, “Three-dimensional micropatterning of bioactive hydrogels via two-photon laser scanning photolithography for guided 3D cell migration.,” *Biomaterials*, vol. 29, pp. 2962–8, jul 2008.
- [39] M. Hahn, J. Miller, and J. West, “Three-Dimensional Biochemical and Biomechanical Patterning of Hydrogels for Guiding Cell Behavior,” *Advanced Materials*, vol. 18, pp. 2679–2684, oct 2006.
- [40] C. B. Schaffer, A. Brodeur, J. F. García, and E. Mazur, “Micromachining bulk glass by use of femtosecond laser pulses with nanojoule energy.,” *Optics letters*, vol. 26, no. 2, pp. 93–95, 2001.
- [41] R. Gattass and E. Mazur, “Femtosecond laser micromachining in transparent materials,” *Nature photonics*, vol. 2, pp. 219–225, 2008.

- [42] M. K. Bhuyan, F. Courvoisier, H. S. Phing, O. Jedrkiewicz, S. Recchia, P. Trapani, and J. M. Dudley, “Laser micro- and nanostructuring using femtosecond Bessel beams,” *The European Physical Journal Special Topics*, vol. 199, pp. 101–110, dec 2011.
- [43] G. Della Valle, R. Osellame, and P. Laporta, “Micromachining of photonic devices by femtosecond laser pulses,” *Journal of Optics A: Pure and Applied Optics*, vol. 11, no. 1, p. 013001, 2009.
- [44] A. M. Kloxin, A. M. Kasko, C. N. Salinas, and K. S. Anseth, “Photodegradable Hydrogels for Dynamic Tuning of Physical and Chemical Properties,” *Science*, vol. 324, pp. 59–63, apr 2009.
- [45] C. Unger, M. Gruene, L. Koch, J. Koch, and B. N. Chichkov, “Time-resolved imaging of hydrogel printing via laser-induced forward transfer,” *Applied Physics A: Materials Science and Processing*, vol. 103, no. 2, pp. 271–277, 2011.
- [46] B. Hopp, T. Smausz, N. Kresz, N. Barna, Z. Bor, L. Kolozsvári, D. B. Chrisey, A. Szabó, and A. Nógrádi, “Survival and proliferative ability of various living cell types after laser-induced forward transfer,” *Tissue engineering*, vol. 11, no. 11-12, pp. 1817–1823, 2005.
- [47] P. Serra, M. Colina, J. M. Fernández-Pradas, L. Sevilla, and J. L. Morenza, “Preparation of functional DNA microarrays through laser-induced forward transfer,” *Applied Physics Letters*, vol. 85, no. 2004, pp. 1639–1641, 2004.
- [48] C. W. Visser, R. Pohl, C. Sun, G.-W. Römer, B. Huis in ‘t Veld, and D. Lohse, “Toward 3D Printing of Pure Metals by Laser-Induced Forward Transfer,” *Advanced Materials*, vol. 27, no. 27, pp. 4087–4092, 2015.

- [49] A. Ovsianikov, M. Gruene, M. Pflaum, L. Koch, F. Maiorana, M. Wilhelm, A. Haverich, and B. Chichkov, “Laser printing of cells into 3D scaffolds,” *Biofabrication*, vol. 2, no. 1, p. 014104, 2010.

Chapter 2

Background

In Chapter 1 a variety of ways in which light can be used to make three dimensional structures in materials as well as some potential applications in biomedicine were described. Most, if not all, of these technologies make use of lasers. Today, inexpensive, high-powered lasers are readily available in a wide range of wavelengths that are suitable for tight focusing which results in very high intensities in the focal volume. The high intensity allows for rapid material modification increasing the speed of the 3D structuring. Further increases in intensity can be realized using ultrafast laser sources. These lasers are powerful enough to drive the nonlinear optical effects that are able to confine light-matter interactions to sub-diffraction limited volumes. In this chapter, the nonlinear polarizability of materials is introduced. Next, a method for generating femtosecond pulses containing the necessary power to drive nonlinear optical behavior is described. Finally, an expression for the rate of multiphoton absorption (MPA) is derived from Schrödinger's equation. Finally, various mechanisms by which absorption of light can lead to material modification are discussed.

2.1 Nonlinear optical susceptibility

As Maxwell deduced in 1864, light travels as an oscillating electric and magnetic field. When such a wave interacts with an atom, the charged components of the atom (electrons and protons) experience a force. At high frequencies associated with visible light (~ 100 THz) the mass of the nucleus is too large to respond to the field and can be considered stationary [1]. Electrons, however, are more free to respond, and are accelerated by the incident electric field. The acceleration of the charged electron leads to the creation of a new electromagnetic wave with the same frequency as the incoming wave, but with a small phase delay. This phase delay gives rise to the slower phase velocity of light in materials known as the index of refraction. At low electric field strengths, the polarization of the atom can be described as:

$$P(t) = p_0 + \epsilon_0 \chi^{(1)} E(t) \quad (2.1)$$

Where P is the relative polarization, p_0 the polarization in the absence of an external electric field, ϵ_0 is the permittivity of free-space, $E(t)$ is the applied electric field, and the proportionality constant $\chi^{(1)}$ is the linear optical susceptibility. Equation 2.1 can be generalized as a power series in field strength as:

$$P(t) = p_0 + \epsilon_0 [\chi^{(1)} E(t) + \chi^{(2)} E^2(t) + \chi^{(3)} E^3(t) + \dots] \quad (2.2)$$

Each of the higher order terms $\chi^{(2)}$, $\chi^{(3)}$, etc. are known as nonlinear susceptibilities because the degree to which they affect the polarization of the material is non-linear with respect to the electric field. In most materials, the nonlinear susceptibilities are quite low and, for relatively weak electric fields, can be ignored. However, the invention of the laser in the 1960s allowed

the generation of beams of light with extremely high electric field strengths allowing these higher order susceptibilities to be explored experimentally for the first time. The use of ultrafast pulsed lasers (see Sec. 2.2) which became increasingly widespread in the 1990s, proved capable of generating peak powers on the order of Gigawatts allowing even higher order nonlinearities to be investigated.

Long before these discoveries, in 1931, Maria Goeppert-Mayer developed a theoretical framework for the nonlinear optical phenomenon of multiphoton absorption [2]. She postulated that in the presence of a large number of low energy photons, a material could absorb two (or more) of those photons simultaneously to lift an electron from the ground to the excited electronic state. Her work was impossible to verify until the invention of the laser enabled sufficiently intense beams of light to be generated [3].

2.2 Mode-locking

In order to investigate high order optical nonlinearities experimentally, a method of generating extremely high light intensities was required. One strategy would be to increase the power of the laser, but this results in material damage to the laser's optical components long before the necessary power is reached. By compressing the output of a laser into short pulses, sufficient intensities can be realized while using relatively low average powers. There are various strategies for compressing light into pulses: Q-switching, cavity dumping, gain switching, etc. Mode locked solid state lasers, however, provided a very robust and reliable tool for routine availability of sub-picosecond pulses and high peak-powers. The following mathematical description of mode-locking has been adapted from Ref. [4].

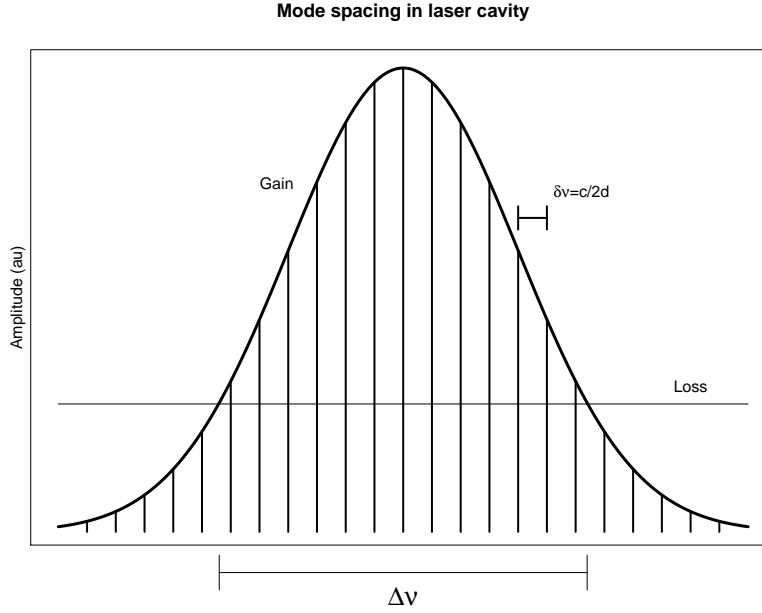


Figure 2.1: The gain spectrum (solid line) plotted vs. frequency on the x-axis. Individual laser modes oscillate with a frequency spacing of $c/2d$. The total bandwidth of the gain medium $\Delta\nu$ is the spectral width of the gain medium that is capable of lasing (ie the gain is greater than the loss).

When pumped above the threshold power a laser will oscillate at a number of different frequencies (i.e. modes) depending on the losses in the laser cavity as well as the bandwidth of the gain medium (Figure 2.1). Individual modes are able to oscillate at wavelengths where the length of the cavity is an integer multiple of half of the wavelength of light.

The total output of the laser can be written as the superposition of all the oscillating modes

$$E(z, t) = \sum_{m=-N/2}^{N/2} A_n \exp\left[-i2\pi\nu_n\left(t - \frac{z}{c} + i\phi_n\right)\right] \quad (2.3)$$

Where N is the integer value of the number of modes oscillating in the laser cavity, A_n is the amplitude of the n -th mode, and ν_n and ϕ_n its frequency and phase respectively. The output intensity is proportional to the square of the

electric field and is given by

$$\begin{aligned}
 I(t) = K|E(t)|^2 = K \sum_{n=-N/2}^{N/2} |A_n|^2 + \\
 K \sum_{n \neq m} \sum_m A_n A_m^* \exp[-i2\pi(\nu_n - \nu_m)(t - \frac{z}{c}) + i(\phi_n + \phi_m)] \quad (2.4)
 \end{aligned}$$

Solving the equation for intensity, it is apparent that the intensity profile repeats with a period of $1/\partial\nu$, the intermodal spacing. (Figure 2.2)

$$I(t) = I(t + 1/\partial\nu) \quad (2.5)$$

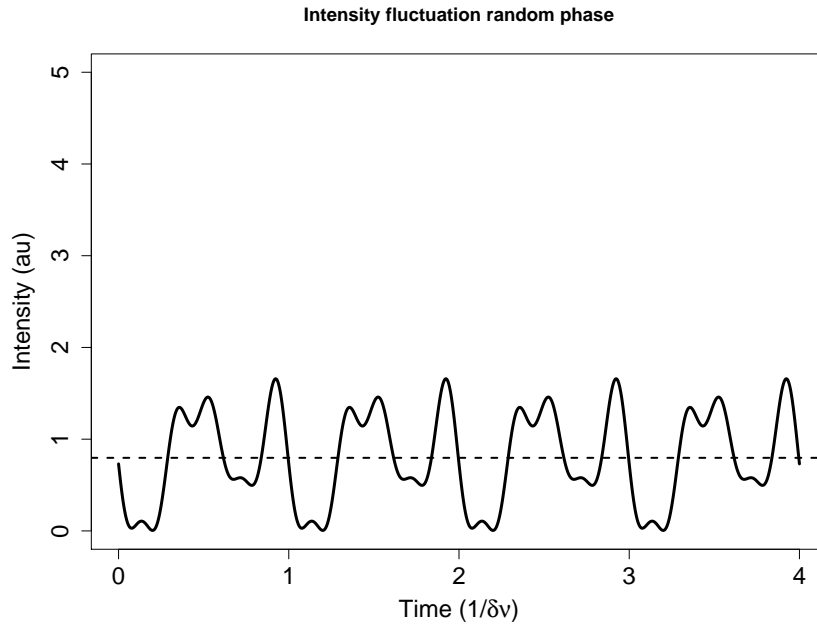


Figure 2.2: Plot of equation 2.3 showing the output intensity of a laser oscillating with 6 modes where A_n follows a Gaussian shape. The intensity fluctuations repeat with a period of the inverse of the intermodal spacing ($1/\partial\nu$). The highest frequency fluctuations occur with a period of $1/\Delta\nu$. The dotted line represents the average intensity of the laser.

If, instead of a random phase, all of the modes in the resonator have the same phase, equation 2.3 can again be solved and squared to give the intensity

profile seen in Figure 2.3. The fixed phase relationship allows constructive interference to occur between all of the modes leading to the formation of a single pulse (Figures 2.3, 2.4), where the width of the pulse can be approximated as:

$$\tau_p \approx \frac{1}{N\partial\nu} = 1/\Delta\nu \quad (2.6)$$

From this equation it is clear that a necessary condition for producing ultrashort pulses is a broad gain bandwidth with many oscillating modes.

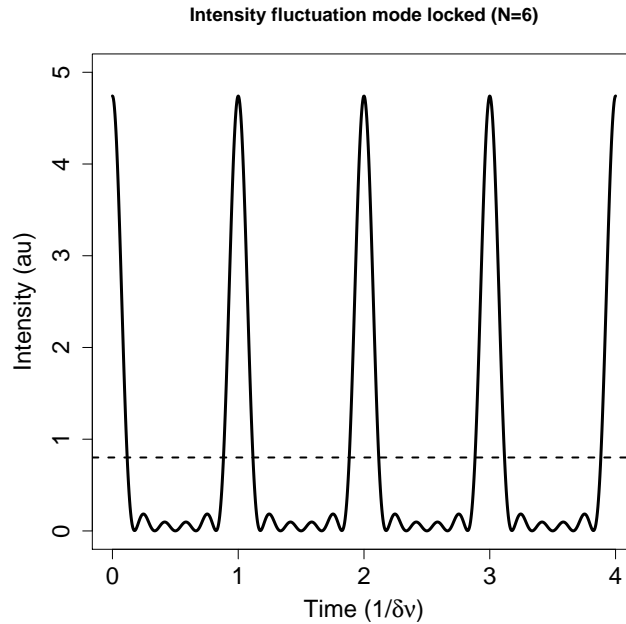


Figure 2.3: Intensity profile of a laser oscillating with 6 modes whose amplitudes follow a Gaussian shape. The fixed phase relationship ensures that the modes constructively interfere at a single point in time leading to the generation of a short pulse that repeats with a frequency of $\partial\nu$. The dotted line indicates the average intensity of the laser which is the same as in Figure 2.2.

The titanium sapphire ($\text{Ti:Al}_2\text{O}_3$) laser, first demonstrated in 1986 operating in continuous wave mode with a maximum output power of 1.6 W at 770 nm [5]. In 1991 Spence, et al. demonstrated mode locking of a $\text{Ti:Al}_2\text{O}_3$ laser generating 60 fs pulses [6]. This technology is now widely used for the production of ultrashort pulses. $\text{Ti:Al}_2\text{O}_3$ has a number of desirable characteristics

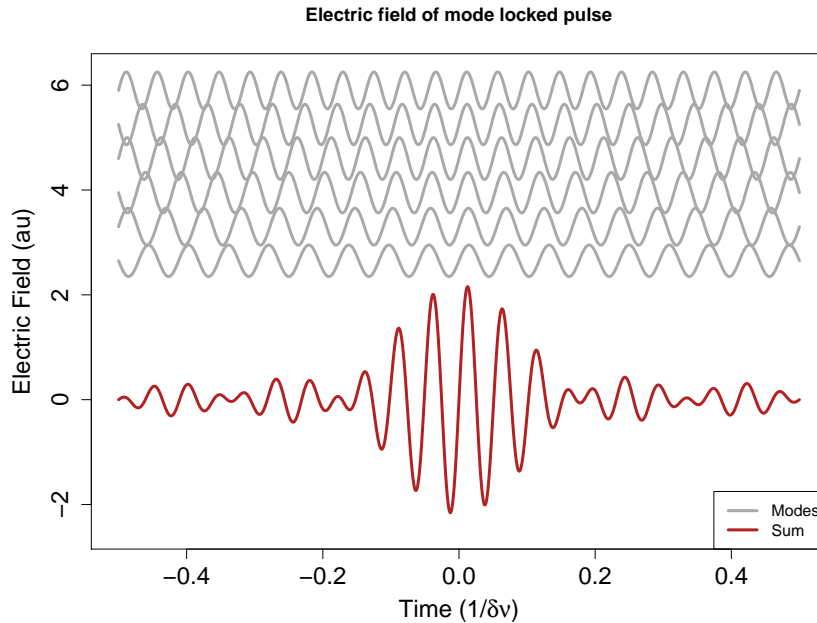


Figure 2.4: Illustration of the electric field in a mode locked laser. Gray lines show the modes oscillating at slightly different frequencies but with a fixed phase relationship. The sum of the modes is shown in red where the electric field of a short optical pulse can be seen.

for a laser gain medium. Especially important is the broad gain bandwidth, high saturation threshold, and thermal conductivity which allow a large number of modes to lase simultaneously. As described above, the large number of oscillating modes is a necessary requirement for ultrashort pulses of light to be generated.

Accompanying the ability of the laser gain medium and cavity to support a large number of oscillating modes is the ability to synchronize the relative phases of these oscillating modes. There are a variety of strategies for fixing this phase relationship. Broadly speaking these strategies can be broken down into two strategies: active and passive. Both of these methods are designed to add highly controlled losses in a laser cavity. In general, lasing will occur where losses are minimized. This is why introducing spatial loss in a cavity can force a laser to oscillate in different spatial modes [7]. The same principle

can be applied to the phase of temporal modes. When properly mode locked, there is a single pulse inside the cavity bouncing back and forth between the two cavity mirrors. In active mode locking schemes, periodic loss is added to the cavity using an acousto-optic modulator. These devices are capable of either allowing light to pass through unimpeded, or deflecting it. By only allowing light to pass at certain times, all of the oscillating modes can be forced to have a maximum during the period of low loss resulting in the formation of an ultrashort pulse. Passive methods can also be used in the form of a saturable absorber. At low light intensities, these materials absorb a portion of the light passing through them. However, at high intensities, the amount of light they absorb is reduced. This ensures that the modes with the lowest loss will have high light intensity at the saturable absorber and, over a few cycles, results in the production of a mode locked pulse. Using Ti:Al₂O₃ laser pulses as short as 5.4 fs have been generated directly from the laser oscillator [8], with 4.5 fs pulses possible using external compression [9]. The extremely high peak intensity of the ultrashort pulses has allowed the investigation of a wide variety of optical nonlinear processes including multiphoton absorption.

2.3 Multiphoton absorption theory

As the term “photon” in the name suggests, multiphoton absorption is best understood through a quantum mechanical lens. While the phenomenon has been described classically via a system of anharmonic oscillators, the quantum mechanical description is more intuitive.

2.3.1 Qualitative description

In the late 19th and early 20th centuries, the classical understanding of physics predicted that a black body would radiate infinite energy in the ultraviolet region of the spectrum. Clearly, this prediction violates the conservation of energy, so a new theory needed to be developed [10]. It was discovered in the early 20th century that the energy an atom was capable of radiating was quantized, disallowing the radiation of extremely high energy photons, and leading directly to the idea of the atom consisting of discrete energy levels. At rest, atoms exist with their electrons populating the ground state having the lowest allowable energy. Upon excitation these electrons can be promoted to an excited state. For each atom there is a gap between the ground and excited state that requires a certain energy to exceed. Light with energies smaller than this gap are incapable of being absorbed by the material, whereas higher energy light can be absorbed with its energy going to promote the electron to the excited state. The excited electron can lose energy by emitting a new photon or decay non-radiatively back to the ground state transforming the absorbed energy into molecular or lattice vibrations. While lower energy photons can interact with the atom, they are not able to promote an electron from the ground state to the excited state. Instead they do promote electrons to a “virtual state” with an energy between the ground and excited states. These virtual states are very short lived with electron lifetimes on the order of a few femtoseconds. What Goeppert-Mayer discovered was that if a second low energy photon interacts with the atom while an electron is in the virtual state the electron can reach the excited electronic state. Under normal conditions the chances of two photons striking the same atom within a few femtoseconds of each other is vanishingly small. But by confining light spatially through focusing, and temporally by using an ultrafast source, the (near)-simultaneous

absorption of two (or more) photons becomes highly probable. The unlikelihood of multiphoton absorption (MPA) under ordinary illumination (e.g. CW or low-peak power lasers) allows the process to be limited to the volume where photon density is the highest. By carefully adjusting the laser power and focal volume, the volume of material experiencing MPA can be reduced to sub-diffraction limited dimensions. Such precision has found application for imaging biomolecules using two-photon excited fluorescence microscopy [11], for generating nanoscale structures via two-photon lithography [12], and for sub wavelength nanodissection of human chromosomes [13].

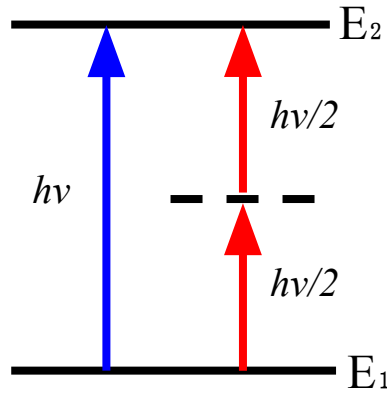


Figure 2.5: Energy level diagram illustrating 2 photon absorption. The ground energy level (E_1) is separated from the excited state (E_2) by a certain amount of energy. Electrons can be excited by a single photon of light with energy $h\nu$ or by two photons with half the energy ($h\nu/2$) via a virtual state (dashed line).

2.3.2 Quantum mechanical description

Single photon absorption

In this section a derivation of the rate of multiphoton absorption is presented that is adapted from Ref. [14]. To begin, we assume that the system undergoing MPA can be described by the atomic wavefunction ($\psi(r, t)$) which is a

solution to the time-dependent Schrödinger equation:

$$i\hbar \frac{\partial \psi}{\partial t} = \hat{H}\psi \quad (2.7)$$

Where \hat{H} is the Hamiltonian operator which can be written as the sum of the Hamiltonian for a free atom \hat{H}_0 and an interaction Hamiltonian $\hat{V}(t)$ which describes the interaction of the atom with an electromagnetic field as:

$$\hat{H} = \hat{H}_0 + \hat{V}(t) \quad (2.8)$$

When no external field is applied $\hat{H} = \hat{H}_0$ and the solutions to Schrödinger's equation have the form:

$$\psi_n(r, t) = u_n(r)e^{-i\omega_n t} \quad (2.9)$$

When inserted into the Schrödinger equation, the spatially varying component of the wavefunction ($u_n(r)$) must satisfy the eigenvalue equation:

$$\hat{H}_0 u_n(r) = E_n u_n(r) \quad (2.10)$$

where $E_n = \hbar\omega_n$ and the subscript n is used to denote different solutions to this equation which is the time-independent Schrödinger equation. The eigenvalues ($u_n(r)$) represent the various electronic energy levels of the system under consideration.

Then, it is assumed that the solutions are chosen such that they form a complete orthonormal set satisfying the orthonormality condition:

$$\int u_m^* u_n d^3r = \delta_{mn} \quad (2.11)$$

Where δ_{mn} is the Kronecker delta function ($\delta_{mn} = 0$, $m \neq n$ and $\delta_{mn} = 1$, $m = n$). Because the eigenvalues form a complete basis the wavefunction can be written as a linear combination of these solutions:

$$\psi(r, t) = \sum_l a_l(t) u_l(r) e^{-i\omega_l t} \quad (2.12)$$

This sum can be directly substituted into the time-dependent Schrödinger equation (Eq. 2.7) which yields:

$$\begin{aligned} i\hbar \sum_l \frac{da_l}{dt} u_l(r) e^{-i\omega_l t} + i\hbar \sum_l (-i\omega_l) a_l(t) u_l(r) e^{-i\omega_l t} \\ = \sum_l a_l(t) E_l u_l(r) e^{-i\omega_l t} + \sum_l a_l(t) \hat{V} u_l(r) e^{-i\omega_l t} \end{aligned} \quad (2.13)$$

By inspection, remembering that $E_l = \hbar\omega_l$, the second and third terms cancel and left-multiplying both sides by u_m^* and integrating gives:

$$i\hbar \int \sum_l u_m^* \frac{da_l}{dt} u_l(r) e^{-i\omega_l t} d^3r = \int \sum_l a_l(t) u_m^* \hat{V} u_l(r) e^{-i\omega_l t} d^3r \quad (2.14)$$

On the left side, the orthonormality condition (Eq. 2.11) sifts out the value at $l = m$. Using this relationship and rearranging some terms gives:

$$i\hbar \frac{da_m}{dt} = \sum_l a_l(t) V_{ml} e^{-i\omega_{lm} t} \quad (2.15)$$

Where $\omega_{lm} = \omega_l - \omega_m$ and

$$V_{ml} = \int u_m^* \hat{V} u_l d^3r \quad (2.16)$$

In most cases Equation 2.15 can't be solved directly and perturbation theory needs to be applied. To do so, an expansion parameter (λ) is introduced which

varies continuously from 0 to 1 and V_{ml} is replaced by λV_{ml} . The physical situation corresponds to the case where $\lambda = 1$, and $\lambda = 0$ is the case where there is no interaction of the atom with the electric field. Using λ , a_m can be written as powers of the interaction:

$$a_m(t) = a_m^{(0)}(t) + \lambda a_m^{(1)}(t) + \lambda^2 a_m^{(2)}(t) + \dots \quad (2.17)$$

Next, by equating powers of λ , the following set of equations is realized:

$$\frac{da_m^{(N)}(t)}{dt} = \sum_l a_l^{(N-1)} V_{ml} e^{-i\omega_l m t}, \quad N = 1, 2, 3, \dots \quad (2.18)$$

Setting $N = 1$ this equation can be used to describe linear absorption. Multiphoton absorption can then be described using the results of the $N = 1$ case to solve for $N = 2$ (two photon absorption), which can be used to solve for three photon absorption ($N = 3$), and so-on.

Assuming electrons initially occupying the ground state in the absence of an external electric field:

$$a_g^{(0)}(t) = 1, \quad a_l^{(0)}(t) = 0 \quad \text{for } l \neq g \quad (2.19)$$

for all time t recalling that a_l is the coefficient of the l^{th} eigenvalue in the linear combination of eigenvalues that are used to describe the atomic wavefunction ψ . For simplicity, the exciting electric field is taken to be a monochromatic plane wave which means the interaction term of the Hamiltonian can be written as:

$$V_{mg} = -\mu_{mg}(Ee^{-i\omega t} + E^*e^{i\omega t}) \quad (2.20)$$

where $\mu_{mg} = -er_{mg}$ with e representing the charge of the electron and r_{mg} is the distance between states g and m .

Substituting this expression for V_{mg} into Equation 2.18 gives:

$$\frac{da_m^{(1)}}{dt} = -(i\hbar)^{-1}\mu_{mg}[Ee^{-i(\omega_{mg}-\omega)t} + E^*e^{i(\omega_{mg}+\omega)t}] \quad (2.21)$$

Which can be integrated with respect to time:

$$a_m^{(1)}(t) = \frac{\mu_{mg}E}{\hbar(\omega_{mg} - \omega)}[e^{i(\omega_{mg}-\omega)t} - 1] + \frac{\mu_{mg}E^*}{\hbar(\omega_{mg} + \omega)}[e^{i(\omega_{mg}+\omega)t} - 1] \quad (2.22)$$

Typically, the second term in this equation is dropped because it describes stimulated emission and not absorption. This approximation is known as the rotating wave approximation. Since a_m is a probability amplitude it must be squared to find the probability of an atom being in state g or state m at time t :

$$\begin{aligned} p_m(t) &= |a_m^{(1)}(t)|^2 = \frac{|\mu_{mg}E|^2}{\hbar^2} \left| \frac{e^{i(\omega_{mg}-\omega)t} - 1}{\omega_{mg} - \omega} \right|^2 \\ &= \frac{|\mu_{mg}E|^2}{\hbar^2} \frac{4 \sin^2[(\omega_{mg} - \omega)t/2]}{(\omega_{mg} - \omega)^2} \end{aligned} \quad (2.23)$$

For large values of t the second term becomes sharply peaked (Figure 2.6) with a maximum value of t^2 and a width of $2\pi/t$. This means that the area is on the order of $2\pi t$. This function can then be approximated by a Dirac delta function so the probability amplitude becomes:

$$\lim_{t \rightarrow \infty} p_m^{(1)}(t) = 2\pi t \delta(\omega_{mg} - \omega) \quad (2.24)$$

In a real physical system the transition between levels m and g are not precise, but are rather spread into a continuous distribution, but for simplicity it will continue to be represented as a delta function. The equation for the probability of an atom transitioning from state g to m via single photon

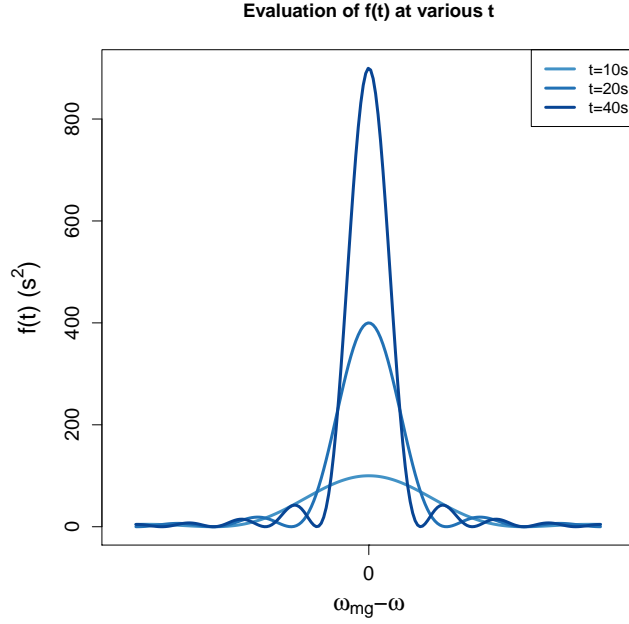


Figure 2.6: Evaluation of the second term of equation 2.23 for varying values of t . As t increases the peak becomes sharper and has a maximum value of t^2 .

absorption can be written as a rate:

$$R_{mg}^{(1)} = \frac{p_m^{(1)}(t)}{t} = \frac{|\mu_{mg}E|^2 t}{\hbar^2} \delta(\omega_{mg} - \omega) \quad (2.25)$$

Multi-photon absorption

To find the rate of transition from the ground state to an excited state via two photon absorption equation 2.18 must be solved for $N = 1$ and $N = 2$. The $N = 1$ case describes linear absorption as above. For $N = 2$ the linear absorption results are substituted into equation 2.18. The equation is solved analogously to above and leads to the rate equation:

$$R_{ng}^{(2)} = \left| \sum_m \frac{\mu_{nm}\mu_{mg}E^2}{\hbar^2(\omega_{mg} - \omega)} \right|^2 2\pi \delta(\omega_{ng} - 2\omega) \quad (2.26)$$

Similarly the rate of three-photon absorption can be described by:

$$R_{og}^{(3)} = \left| \sum_m \frac{\mu_{on}\mu_{nm}\mu_{mg}E^3}{\hbar^3(\omega_{ng} - 2\omega)(\omega_{mg} - \omega)} \right|^2 2\pi\delta(\omega_{og} - 3\omega) \quad (2.27)$$

2.4 Material damage

The transfer of energy to a material whether via single or multiphoton process can result in material damage. Laser induced damage can be broken down into three different regimes based on how the energy is delivered: continuous wave (CW), relatively long (> 100 ps) pulses, and ultrashort (< 100 ps) pulses. CW lasers output light at a constant power over time. Damage from these beams occurs through linear absorption of the light leading to heating and cracking of the material. This absorption, even in materials that are nominally transparent, is sufficient to heat and cause damage given sufficient intensity and exposure time [15]. This mechanism results in significant damage surrounding the focal volume of the light incident on the material due to heat diffusion out of the irradiated region.

Lasers delivering light in pulses of hundreds of nanoseconds to hundreds of picoseconds cause damage through avalanche breakdown. Under these conditions quasi-free seed electrons found randomly in the material, or concentrated in defects, are heated by incoming photons. This heating results in high energy electrons that then transfer energy to ground state electrons via collisions, promoting them to a quasi-free state (Figure 2.7). The process is repeated on both the original and newly freed electrons creating a cascade that rapidly increases the density of free electrons forming a plasma [14]. With these relatively long pulses, the plasma is formed while light having high intensity is present in the material. The plasma is then able to absorb light from the pulse,

sharply increasing the energy transferred into the material. Damage occurs when the excited electrons transfer their energy to the material lattice resulting in melting or boiling. The rapid increase in energy deposition from the absorbing plasma makes it difficult to precisely control damage in this regime [16].

For ultrashort pulses (<10 ps) the intensities are sufficiently high for multiphoton ionization to play a dominant role. Here, no free seed electrons are needed because they are created via multiphoton absorption or quantum tunneling [17]. Rates of quantum tunneling increase in the presence of a strong electric field which can distort the band structure of the material [18]. Both processes result in free electrons which are accelerated by the laser field and can subsequently free ground-state electrons by collisions in a process similar to the long-pulse case [19]. Because the pulses are so short, there is limited time for such a cascade to produce additional free electrons before the pulse has passed, meaning that free electron density can be controlled by altering the intensity of the pulses [16]. Damage occurs when the free electrons cool, transferring their energy to the lattice. Precise control over free electron density allows fine localization of material damage. The extremely high field intensities combined with the fact that a cascade can arise from relatively few seed electrons by free-carrier absorption means that this technique is relatively insensitive to the bandgap of the material being exposed [20].

The use of short and ultrashort pulses of light to modify materials has a number of distinct advantages over CW illumination. As the pulses get shorter the average power used to disrupt materials can be reduced. Shorter pulses reduce the uncontrolled production of free electrons which helps confine the damage only to the focal volume and limiting the heat affected zone around the desired feature [21].

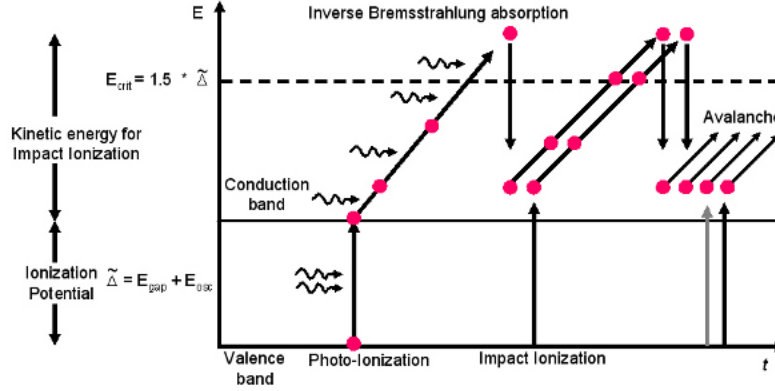


Figure 2.7: Schematic diagram of avalanche ionization leading to material damage. Adapted from Ref. [22].

The previous paragraphs focused solely on direct laser induced damage and not on cumulative effects. Femtosecond oscillators typically produce pulse trains at pulse repetition rates on the order of 10^7 pulses per second. In this case, in addition to the effect of individual pulses, there is a cumulative effect as well. The most prominent effect is thermal as the heat from cooling electrons from a pulse does not have time to diffuse out of the focal volume before the arrival of the next pulse [23]. This results in an accumulation of heat in the focal volume which can lead to local material modification by melting or boiling.

High energy electrons excited by optical fields can also have a direct chemical effect on materials. Such electrons can be trapped by molecules which increases the distance between adjacent nuclei. This increased distance can lead to molecular dissociation [22]. Indirect chemical effects are also possible. If water and oxygen are present, free electrons generated by high intensity laser radiation can form hydroxyl radicals directly, or can react with dissolved oxygen to form superoxide ions (O_2^-) [24]. Superoxide ions react with water to form hydrogen peroxide and further react with hydrogen peroxide to produce hydroxyl radicals ($OH\cdot$). The hydroxyl radical producing step is a Fenton re-

action requiring the presence of trace amounts of transition metal ions such as iron or manganese. The hydroxyl radical is an extremely potent oxidizer and can cause damage to proteins, lipids, and DNA [25]. In the following chapters a series of experiments to measure multiphoton absorption in silk fibroin and characterize the breakdown of silk as it absorbs light energy will be presented.

Bibliography

- [1] M. Born and R. Oppenheimer, “Zur quantentheorie der molekeln,” *Annalen der Physik*, vol. 389, no. 20, pp. 457–484, 1927.
- [2] M. Göppert-Mayer, “Über elementarakte mit zwei quantensprünge,” *Annalen der Physik*, vol. 401, no. 3, pp. 273–294, 1931.
- [3] W. Kaiser and C. Garrett, “Two-Photon Excitation in CaF₂:Eu²⁺,” *Physical Review Letters*, vol. 7, no. 6, pp. 229–231, 1961.
- [4] K. Thyagarajan and A. K. Ghatak, *Lasers theory and applications*. New York, NY: Plenum Press, 1981.
- [5] a. Sanchez, R. E. Fahey, a. J. Strauss, and R. L. Aggarwal, “Room-temperature continuous-wave operation of a Ti:Al₂O₃ laser,” *Optics letters*, vol. 11, no. 6, pp. 363–4, 1986.
- [6] D. E. Spence, P. N. Kean, and W. Sibbett, “60-fsec pulse generation from a self-mode-locked Ti:sapphire laser,” *Optics letters*, vol. 16, no. 1, pp. 42–44, 1991.
- [7] K. Kano, Y. Kozawa, and S. Sato, “Generation of a purely single trans-

- verse mode vortex beam from a He-Ne laser cavity with a spot-defect mirror,” *International Journal of Optics*, vol. 2012, pp. 1–7, 2012.
- [8] U. Morgner, F. X. Kärtner, S. H. Cho, Y. Chen, H. a. Haus, J. G. Fujimoto, E. P. Ippen, V. Scheuer, G. Angelow, and T. Tschudi, “Sub-two-cycle pulses from a Kerr-lens mode-locked Ti:sapphire laser.,” *Optics letters*, vol. 24, no. 6, pp. 411–413, 1999.
- [9] M. Nisoli, S. De Silvestri, O. Svelto, R. Szipöcs, K. Ferencz, C. Spielmann, S. Sartania, and F. Krausz, “Compression of high-energy laser pulses below 5 fs.,” *Optics letters*, vol. 22, no. 8, pp. 522–524, 1997.
- [10] D. A. McQuarrie and J. D. Simon, *Physical Chemistry: A Molecular Approach*. Sausalito, CA: University Science Books, 1 ed., 1997.
- [11] W. R. Zipfel, R. M. Williams, and W. W. Webb, “Nonlinear magic: multiphoton microscopy in the biosciences.,” *Nature biotechnology*, vol. 21, pp. 1369–77, nov 2003.
- [12] S. Juodkazis, V. Mizeikis, K. K. Seet, M. Miwa, and H. Misawa, “Two-photon lithography of nanorods in SU-8 photoresist,” *Nanotechnology*, vol. 16, no. 6, p. 846, 2005.
- [13] K. König, I. Riemann, and W. Fritzsche, “Nanodissection of human chromosomes with near-infrared femtosecond laser pulses,” *Optics letters*, vol. 26, no. 11, pp. 819–821, 2001.
- [14] R. W. Boyd, “Optically Induced Damage and Multiphoton Absorption,” *Nonlinear Optics*, pp. 543–560, 2008.
- [15] R. Wood, “Laser induced damage thresholds and laser safety levels. Do

- the units of measurement matter?,” *Optics & Laser Technology*, vol. 29, no. 8, pp. 517–522, 1998.
- [16] A. Vogel, J. Noack, G. Hüttman, and G. Paltauf, “Mechanisms of femtosecond laser nanosurgery of cells and tissues,” *Applied Physics B: Lasers and Optics*, vol. 81, pp. 1015–1047, 2005.
- [17] M. D. Perry, B. C. Stuart, P. S. Banks, M. D. Feit, V. Yanovsky, and a. M. Rubenchik, “Ultrashort-pulse laser machining of dielectric materials,” *Journal of Applied Physics*, vol. 85, no. 9, p. 6803, 1999.
- [18] L. V. Keldysh, “Ionization in the field of a strong electromagnetic wave,” *Journal of Experimental and Theoretical Physics*, vol. 20, no. 5, pp. 1307–1314, 1965.
- [19] R. Osellame, G. Cerullo, and R. Ramponi, *Femtosecond Laser Micromachining: Photonic and Microfluidic Devices in Transparent Materials*. Springer, 2012.
- [20] R. Gattass and E. Mazur, “Femtosecond laser micromachining in transparent materials,” *Nature photonics*, vol. 2, pp. 219–225, 2008.
- [21] B. Chichkov, C. Momma, S. Nolte, F. von Alvensleben, and A. Tunnermann, “Femtosecond, picosecond and nanosecond laser ablation of solids,” *Applied Physics A: Materials Science and Processing*, vol. 63, pp. 109–115, 1996.
- [22] A. Vogel, J. Noack, G. Hüttmann, and G. Paltauf, “Femtosecond-laser-produced low-density plasmas in transparent biological media: a tool for the creation of chemical, thermal, and thermomechanical effects below the optical breakdown threshold,” *Spie*, vol. 4633, pp. 23–37, 2002.

- [23] R. R. Gattass, L. R. Cerami, and E. Mazur, “Micromachining of bulk glass with bursts of femtosecond laser pulses at variable repetition rates.,” *Optics express*, vol. 14, no. 12, pp. 5279–5284, 2006.
- [24] D. N. Nikogosyan, A. a. Oraevsky, and V. I. Rupasov, “Two-Photon Ionization and dissociation of liquid water by powerful UV radiation,” *Chemical Physics*, vol. 77, pp. 131–143, 1983.
- [25] E. Cabiscol, J. Tamarit, and J. Ros, “Oxidative stress in bacteria and protein damage by reactive oxygen species,” *International Microbiology*, vol. 3, no. 1, pp. 3–8, 2000.

Chapter 3

Nonlinear absorption in silk

3.1 Introduction

With the increasing availability of commercial ultrafast lasers, the study of optical nonlinearities in materials has received a great deal of attention [1]. Nonlinear interaction of light with materials has enabled the highly precise patterning of metals, semiconductors, and dielectrics. High resolution and smooth walls are due to the non-thermal nature of the ablation process when ultrashort pulses are used [2]. In addition, intensity dependent change in index of refraction of inorganic materials have been studied for use in optical switching applications [1]. However, the investigation of absorptive nonlinearities such as two-photon absorption (2PA) and three-photon absorption (3PA) in organic materials has been less well studied. Previous investigations of biologicals have been undertaken for the food industry, but materials of medical significance have been largely ignored [3]. Silk fibroin is an attractive material for tissue engineering, due to its relative lack of immune response upon implantation; optical engineering, thanks to its exceptional clarity; and drug delivery, for its ability to stabilize biologically relevant chemicals [4, 5, 6, 7].

In this chapter the multiphoton absorption of solutions of reconstituted silk fibroin is demonstrated and characterized using the open aperture (OA) Z-scan technique. Characterization of the nonlinear properties of biologically compatible materials has applications in laser ablation and three-dimensional micromachining of tissue scaffolds to guide cell growth [8, 9], and as a general purpose tool to shape soft materials.

3.2 Materials & methods

The Z-scan technique is a single beam method for determining optical nonlinearity in transparent samples [10]. It has been described extensively elsewhere, but the main idea is to translate a sample through the focus of a Gaussian beam and measure the amount of transmitted light in the far field (Figure 3.1). As the sample approaches the beam's focus, the peak intensity of the light rises, increasing the likelihood of multiphoton absorption. This absorption is detected in the far-field as a decrease in transmitted light. After the focal plane, the peak intensity decreases and multiphoton absorption becomes unlikely resulting in a return to the initial transmitted intensity. This technique has been used to characterize a breathtaking variety of materials in both solid and liquid phases [11, 12, 3, 13, 14].

Reconstituted silk fibroin was prepared as previously described [15]. Briefly, cocoons from domesticated silk worms were cut and boiled in a solution of 0.02 M sodium carbonate to remove the glue-like sericin protein. The resulting fibroin was dissolved in lithium bromide for 4 hours, and the solution dialyzed against water for two days. Solutions of 4 different molecular weights were prepared (270, 210, 100, and 67 kDa) by boiling for 10, 30, 60, or 120 minutes respectively (Figure 3.2). Three batches of each of the silk solutions were made

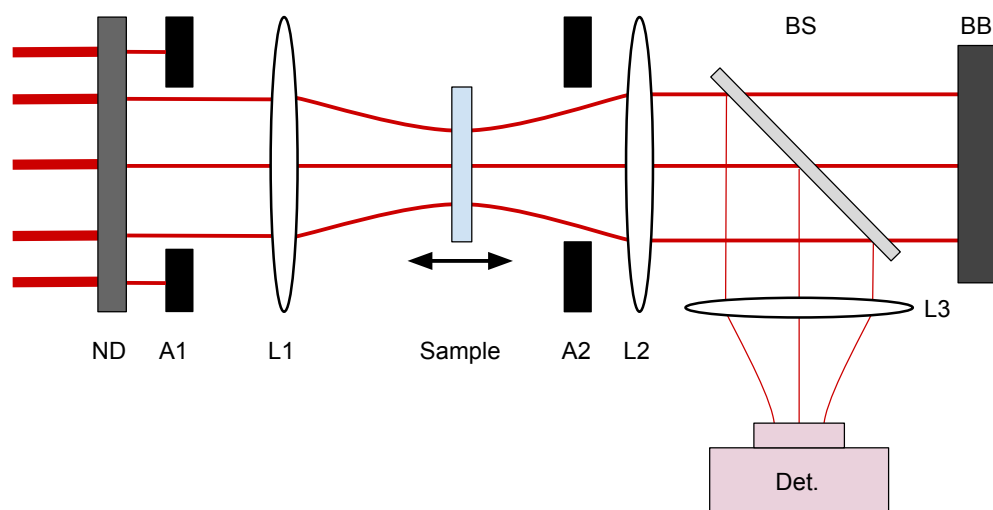


Figure 3.1: Schematic representation of Z-scan technique for measuring optical nonlinearity. Neutral density filters (ND) are used to control the pulse energy. Aperture (A1) spatially filters the beam. A lens (L1) focuses the beam onto the sample which is scanned along the optical axis. A second aperture (A2) can be left open to measure the imaginary part of the hyperpolarizability or closed to measure the real component. The beam is collimated by another lens (L2), split by a beamsplitter (BS) and focused onto a detector by L3. Beam block (BB) stops light transmitted by the beamsplitter.

and tested. The protein concentration of each solution was standardized to 5% (wt/vol) by dilution with deionized water. The molecular weights of the silk solutions were measured by gel electrophoresis using a 4-12% Bis-Tris gel (Invitrogen, Grand Island, NY).

Samples were illuminated with 150 fs pulses of 810 nm light with a pulse repetition rate of 80 MHz provided by a mode-locked titanium sapphire laser (Tsunami, Spectra Physics). The light was focused onto the sample by a 10 cm focal length lens to a minimum FWHM diameter of $30 \mu\text{m}$ measured by the knife edge method (Figure 3.3). Solutions were placed in a 1 mm pathlength glass cuvette (Starna Cells, Atascadero, CA) prior to scanning. The short path

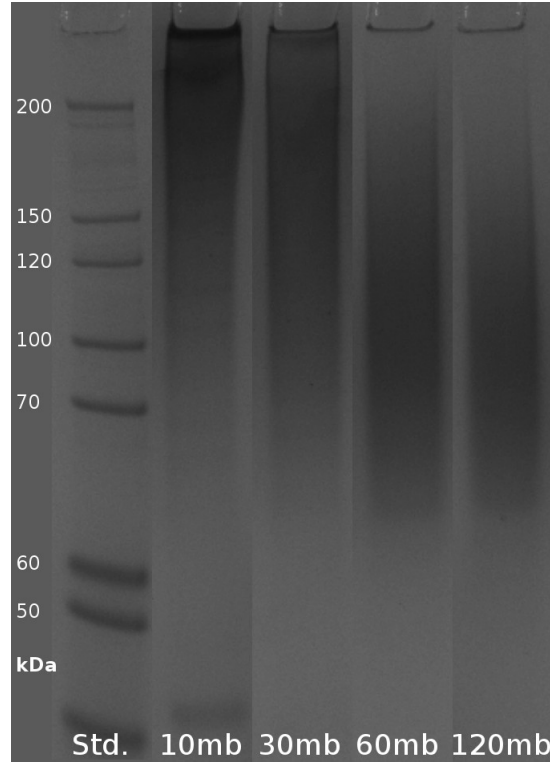


Figure 3.2: Representative gel electrophoresis sample of silk boiled for 10, 30, 60, and 120 minutes.

length cuvette ensured that the sample length was shorter than the Rayleigh length of the beam ($z_R \approx 3.5$ mm) satisfying the thin sample condition. The beam was re-collimated by a second 10 cm focal length lens, passed through a beamsplitter to attenuate the power, and focused onto a silicon photo detector (Thor Labs, Newton, NJ). Samples were translated along the beam path at a constant rate of 2 mm/s by a computer controlled linear stage. This translation rate allowed the transmitted intensity to be recorded about every 10 μm . A custom LabVIEW application was used to control the sample position and record the photodiode voltage (Figure 3.4).

Both high and low power scans were collected for each sample using pulse energies of 12.5 nJ and 0.5 nJ respectively. Laser power was controlled using neutral density filters. During data analysis, the normalized low power scan was subtracted from the normalized high power scan to reduce the effects of

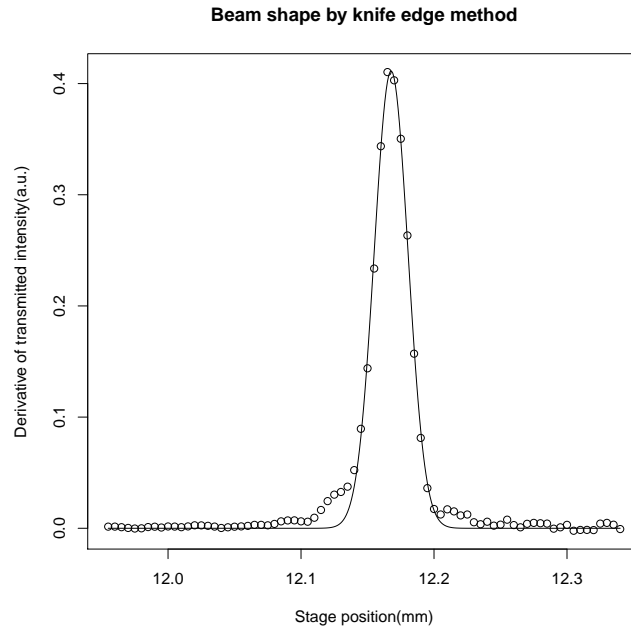


Figure 3.3: Measurement of the beam waist using the knife edge method showing a FWHM of $30 \mu\text{m}$

sample wedge and surface imperfections [10]. Scans were collected from 3 independent batches of silk as well as solutions of L-tyrosine at concentrations of 250 and 35 mM, and L-tryptophan at a concentration of 500 mM. The amino acid solutions were dissolved in 1 M hydrochloric acid (HCl). Cuvettes filled with water and 1 M HCl were also scanned to measure the background signal due to the solvent. Amino acids were purchased from Sigma-Aldrich and used without modification.

3.2.1 Data Processing

Collected transmission data were processed to remove artifacts due to sample wedge and surface imperfections and fit to a theoretical model of transmission (Figure 3.5). The theoretical models of two- and three-photon absorption for open aperture Z-scans are well documented in literature [16]. It can be shown that the far field transmission for two- and three-photon absorption processes,

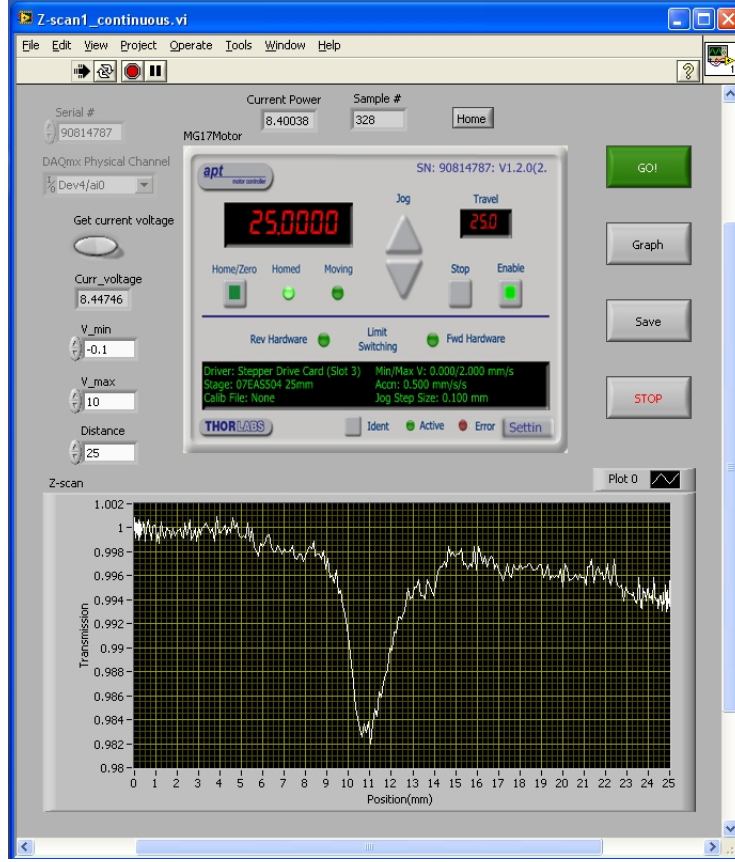


Figure 3.4: Screenshot of the custom LabView application designed to automatically run a single Z-scan experiment

assuming a pulse that is Gaussian in both space and time, are respectively:

$$T_2(x, \Psi_1) = \ln(1 + \psi_1)/\psi_1 \quad (3.1)$$

$$T_3(x, \Psi_2) = \sinh^{-1}(\psi_2)/(\psi_2) \quad (3.2)$$

Where $\psi_n = \Psi_n/(1 + x^2)$. Here, $x = z/z_R$ where z is the distance from the focus and z_R the Rayleigh range of the beam. Ψ_n is the peak phase shift: $\Psi_n = (n\beta_n I_0^n L_{eff}^{(n)})^{1/n}$ where β_n is the $n + 1$ photon absorption coefficient, I_0 the peak intensity of the beam, and $L_{eff}^{(n)}$ the effective sample length given an $n + 1$ photon absorption process. $L_{eff}^{(n)} = [1 - \exp(-n\alpha_0 L)]/n\alpha_0$ where α_0 is the linear absorption and L the sample length.

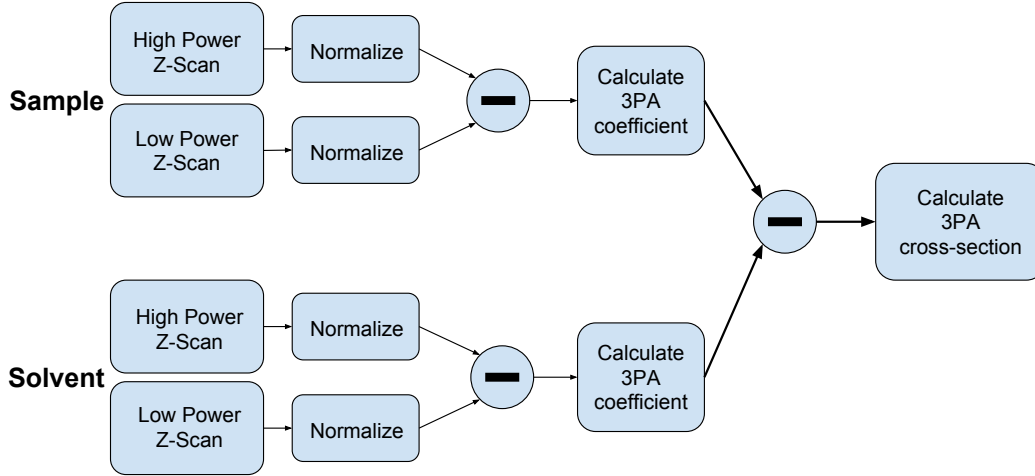


Figure 3.5: Z-scan data analysis workflow. First high and low energy scans are taken of the sample and the solvent and normalized. These are subtracted to correct for sample imperfections and alignment issues. The 3-photon coefficient (β_2) is then calculated. The coefficients are subtracted to calculate the 3-photon cross-section.

Transmission curves from each scan were fit to the above three-photon theoretical model using least squares estimation and β_2 determined using the R [17]. For isotropic liquids such as silk solution, this three-photon absorption coefficient can be related to the three-photon cross section (σ') by the formula [18]:

$$\sigma'_3 = \frac{\beta_2}{N_A \cdot d_0 \cdot 10^{-3}} \left(\frac{hc}{\lambda} \right)^2 \quad (3.3)$$

Here, N_A is Avogadro's number and d_0 the molar concentration of the solution. hc/λ is the photon energy with h , c , and λ representing Planck's constant, the speed of light in vacuum, and the wavelength respectively. The factor 10^{-3} converts liters to cubic centimeters. The 3PA cross-section is independent of sample concentration.

Background scans of water and HCl were collected and analyzed identically to the silk and amino acid solutions. The β_2 of the background was subtracted from the estimated β_2 of each observation of silk and amino acid

solution. This normalization was used to account for any day-to-day laser or instrumental variation as well as remove potential influences from the cuvette and solvent. Following background subtraction, comparison between groups was accomplished via analysis of variance. Tukey’s test was used to determine significant differences between groups.

3.3 Results

Silk fibroin is almost totally transparent to visible light with a strong absorption peak around 270 nm [19]. This peak makes a three-photon absorption process far more likely than other non-linear absorption processes. The presence of three-photon absorption in silk fibroin was verified by fitting OA Z-scan transmission curves to theoretical models corresponding to two-photon (Eq. (3.1)) and three-photon absorption (Eq. (3.2)) [16]. Under the test conditions, the three-photon model was found to be a better fit to the data than the two-photon model (Fig. 3.6).

The OA Z-scans collected from silk with molecular weights of approximately 270, 210, 95, and 67 kDa corresponding to boil times of 10, 30, 60, and 120 minutes respectively were analyzed and the three-photon absorption coefficient for each of these was calculated after accounting for the contribution of the solvent as previously described. As shown in Fig. 3.8(A), each of the silk solutions was significantly different from background ($p < 0.05$). Solutions of tyrosine at a concentration equal to that found in silk (~ 35 mM) as well as a higher concentration (250 mM) were not found to be significantly different from background. A relatively high concentration (500 mM) of tryptophan was also scanned and found to have a larger three-photon coefficient than the other solutions save the highest molecular weight silk. Silk boiled

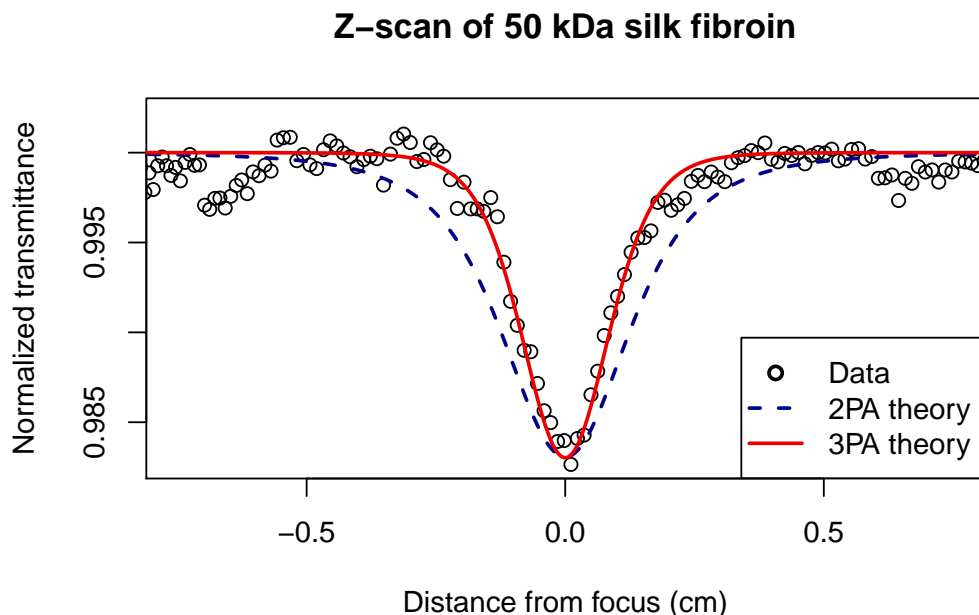


Figure 3.6: Representative open aperture Z-scan data from 100 kDa silk fibroin solution with theoretical best fit curve for two-photon absorption (dashed) and three-photon absorption (solid).

for 10 minutes had a significantly higher three-photon absorption coefficient than silk boiled for 60 minutes. This difference is better explained using a concentration independent measure of nonlinear susceptibility.

The three-photon absorption coefficient can be misleading in solutions due to its dependence on concentration. As expected, increasing the concentration of both the silk fibroin and the amino acid solutions resulted in a linear increase in three-photon coefficient (Figure 3.7) [10]. Although the same amount of protein is present in each of the silk solutions, the molar concentration varies greatly due to the change in molecular weight with changing boil times. The three-photon cross section of each of the solutions was calculated by Eq. (3.3) to ultimately obtain a concentration-independent measure of three-photon absorption. The 3PA cross section was found to increase exponentially with increasing molecular weight (Figure 3.8(B)). Estimated cross sections are tab-

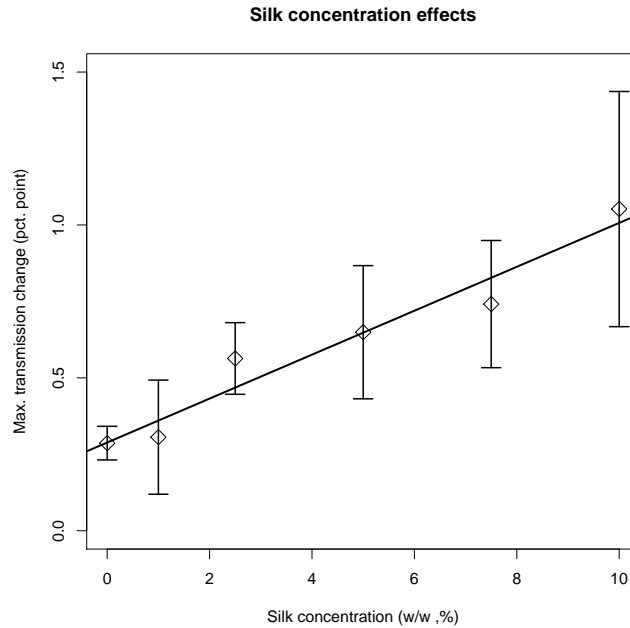


Figure 3.7: Maximum change in transmission during the Z-scan is roughly linear with respect to silk concentration. Error bars represent 1 standard deviation (n=3).

ulated in Table 3.1.

Table 3.1: Summary of multiphoton absorption findings in silk and amino acid solutions. Cross sections are presented as the mean \pm standard error.

Material	Mol. weight (kDa)	Concentration (mM)	3PA cross-section (σ') $\times 10^{-77} (cm^6 s^2 / ph^2)$
Tryptophan	0.2	500	0.019 ± 0.003
Tyrosine	0.1	250	—
SF10	270	0.76	38 ± 5
SF30	210	0.55	25 ± 2
SF60	100	0.24	8.6 ± 0.1
SF120	67	0.19	7.1 ± 0.9

3.4 Discussion

Tryptophan accounts for only 0.5% of the amino acid content of silk fibroin by weight [20]. However, the observed linear absorption and fluorescence of silk

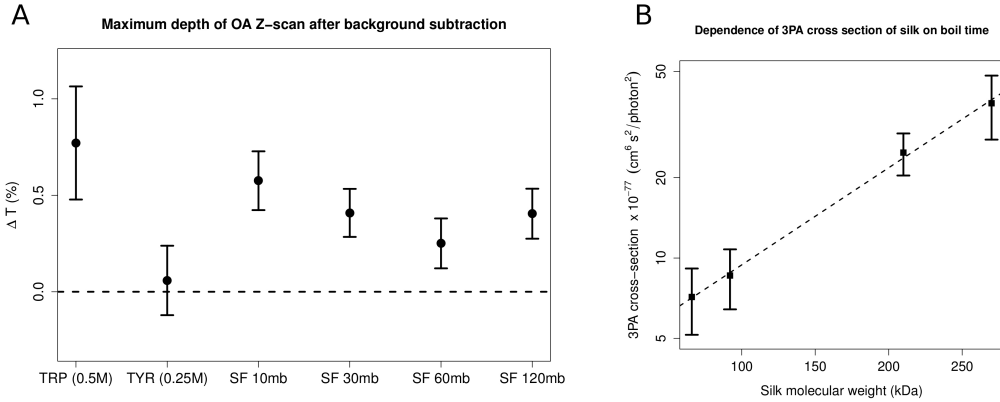


Figure 3.8: A) Normalized change in transmission for the solutions tested after accounting for the contribution of the solvent. TRP is tryptophan in HCl, TYR is tyrosine in HCl. SF 10mb to SF 120mb indicate the length of time the silk was boiled during degumming. Error bars indicate 95% confidence intervals. B) Plot of 3PA cross section and silk molecular weight. Error bars indicate the 95% confidence intervals. Note the y-axis is plotted on a log scale.

is dominated by tryptophan [21, 22]. Previous work has also shown that the number of tryptophan residues in a protein is strongly correlated with its 2PA cross-section [23]. For this reason, it is likely the 3PA exhibited by silk is, in large part, due to tryptophan. We attribute the enhancement of 3PA cross-section over free tryptophan to the micellar structure of silk fibroin in solution with water. Tryptophan is hydrophobic and is found at the centers of these micelles resulting in locally high concentrations and a concomitant increase of 3PA cross-section [24, 25]. Given the markedly larger cross-section of silk compared with free tryptophan, it is likely that interactions such as FRET, $\pi - \pi$ stacking, or covalent bonding between elements of the silk protein are occurring, resulting in an increased nonlinear susceptibility.

The molecular weight dependence on 3PA cross-section is suspected to be due to the degradation of tryptophan residues during degumming. Tryptophan can degrade when exposed to temperatures above 90°C [26]. Such degradation would result in the observed trend of decreasing 3PA with increasing boil times.

The estimated three-photon cross section of tryptophan measured in this

work is roughly three orders of magnitude larger than that found in previous work using fluorescence techniques [27]. Nonlinear transmission methods of measuring multi-photon absorption, such as the Z-scan, have been shown to overestimate three-photon cross sections by approximately this amount due to excited state absorption, self-focusing, and other nonlinear mechanisms that can reduce the intensity of transmitted light [28]. This uncertainty means that the Z-scan technique yields an ensemble measurement of non-linear absorption processes. Normalizing the measured three-photon cross section of silk fibroin by the measured cross section of tryptophan, this work found that silk has a cross section between 100 and 1000 times larger than the amino acid alone.

This normalized estimation is predicated on tryptophan being the only optically active substance in the silk fibroin, given that other nonlinear processes, such as self-focusing, are similar in both the tryptophan and silk fibroin solutions. It has been shown that tryptophan is the only optically active component of silk fibroin at 810 nm along with evidence to support the assertion that tryptophan concentration is not directly correlated with refractive index nonlinearities which result in self-focusing [29]. One assumption here is that excited state absorption effects are small in comparison to nonlinear absorption. Characterization of these effects would rely on modified experimental approaches [30, 31] and will be the subject of continuing research.

A potential application for the high multiphoton absorption of silk fibroin is the direct laser writing (DLW) of three-dimensional patterns within any form of silk that is optically accessible (e.g. films, gels, fibers, blocks, etc.). DLW relies on the fact that multiphoton absorption will only occur when photon densities exceed a material dependent threshold. By focusing light into a material, the location of absorbed photons can be precisely controlled in three dimensions. Silk fibroin gels can be created using a variety of techniques [15],

and are promising materials for cell scaffolds. Methods of patterning soft gels are currently limited mainly to soft lithography. Contact techniques typically result in damage to the material limiting their utility for producing small-scale features. The addition of high-resolution, three-dimensional micromachining could have substantial impact on future tissue engineering applications. In the next chapter a technique to create voids in silk hydrogels is described that takes advantage of the large multiphoton cross section of silk. Further evidence for the purely three-photon nature of multiphoton absorption by silk in the near infrared is found by the development of a finite element model to describe the void formation.

Bibliography

- [1] A. Zakery and S. R. Elliott, “Optical properties and applications of chalcogenide glasses: a review,” *Journal of Non-Crystalline Solids*, vol. 330, pp. 1–12, nov 2003.
- [2] X. Liu, D. Du, and G. Mourou, “Laser ablation and micromachining with ultrashort laser pulses,” *IEEE Journal of Quantum Electronics*, vol. 33, no. 10, pp. 1706–1716, 1997.
- [3] R. A. Ganeev, G. S. Boltaev, R. I. Tugushev, and T. Usmanov, “Investigation of nonlinear optical properties of various organic materials by the Z-scan method,” *Optics and Spectroscopy*, vol. 112, pp. 906–913, jun 2012.
- [4] H. Tao, D. L. Kaplan, and F. G. Omenetto, “Silk materials - a road to sustainable high technology.,” *Advanced materials*, vol. 24, pp. 2824–2837, jun 2012.

- [5] H. Tao, J. M. Kainerstorfer, S. M. Siebert, E. M. Pritchard, A. Sassaroli, B. J. B. Panilaitis, M. A. Brenckle, J. J. Amsden, J. Levitt, S. Fantini, D. L. Kaplan, and F. G. Omenetto, “Implantable, multifunctional, bioresorbable optics,” *Proceedings of the National Academy of Sciences*, vol. 109, no. 48, pp. 19584–19589, 2012.
- [6] F. G. Omenetto and D. L. Kaplan, “A new route for silk,” *Nature Photonics*, vol. 2, no. 11, pp. 641–643, 2008.
- [7] X. Wang, T. Yucel, Q. Lu, X. Hu, and D. L. Kaplan, “Silk nanospheres and microspheres from silk/pva blend films for drug delivery,” *Biomaterials*, vol. 31, pp. 1025–1035, mar 2010.
- [8] A. M. Kloxin, A. M. Kasko, C. N. Salinas, and K. S. Anseth, “Photodegradable Hydrogels for Dynamic Tuning of Physical and Chemical Properties,” *Science*, vol. 324, pp. 59–63, 2009.
- [9] M. B. Applegate, J. Coburn, B. P. Partlow, J. E. Moreau, J. P. Mondia, B. Marelli, D. L. Kaplan, and F. G. Omenetto, “Laser-based three-dimensional multiscale micropatterning of biocompatible hydrogels for customized tissue engineering scaffolds,” *Proceedings of the National Academy of Sciences*, vol. 112, pp. 12052–12057, sep 2015.
- [10] M. Sheik-Bahae, A. A. Said, T.-H. Wei, D. J. Hagan, and E. W. Van Stryland, “Sensitive measurement of optical nonlinearities using a single beam,” *IEEE Journal of Quantum Electronics*, vol. 26, pp. 760–769, apr 1990.
- [11] R. A. Ganeev, “Nonlinear refraction and nonlinear absorption of various media,” *Journal of Optics A: Pure and Applied Optics*, vol. 7, pp. 717–733, dec 2005.

- [12] M. Samoc, A. Samoc, B. Luther-Davies, Z. Bao, L. Yu, B. Hsieh, and U. Scherf, “Femtosecond Z-scan and degenerate four-wave mixing measurements of real and imaginary parts of the third-order nonlinearity of soluble conjugated polymers,” *Journal of the Optical Society of America B*, vol. 15, p. 817, feb 1998.
- [13] J. He, Y. Qu, H. Li, J. Mi, and W. Ji, “Three-photon absorption in ZnO and ZnS crystals,” *Optics express*, vol. 13, pp. 9235–9247, nov 2005.
- [14] D. Rativa, S. J. S. da Silva, J. Del Nero, A. S. L. Gomes, and R. E. de Araujo, “Nonlinear optical properties of aromatic amino acids in the femtosecond regime,” *Journal of the Optical Society of America B*, vol. 27, p. 2665, nov 2010.
- [15] D. N. Rockwood, R. C. Preda, T. Yücel, X. Wang, M. L. Lovett, and D. L. Kaplan, “Materials fabrication from *Bombyx mori* silk fibroin,” *Nature protocols*, vol. 6, pp. 1612–1631, oct 2011.
- [16] B. Gu, J. Wang, J. Chen, Y.-X. Fan, J. Ding, and H.-T. Wang, “Z-scan theory for material with two- and three-photon absorption,” *Optics express*, vol. 13, pp. 9230–9234, nov 2005.
- [17] R Core Team, *R: A Language and Environment for Statistical Computing*. R Foundation for Statistical Computing, Vienna, Austria, 2015.
- [18] F. E. Hernández, K. D. Belfield, and I. Cohanoschi, “Three-photon absorption enhancement in a symmetrical charge transfer fluorene derivative,” *Chemical Physics Letters*, vol. 391, pp. 22–26, jun 2004.
- [19] a. Sionkowska and a. Planecka, “The influence of UV radiation on silk fibroin,” *Polymer Degradation and Stability*, vol. 96, pp. 523–528, 2011.

- [20] R. Apweiler, M. J. Martin, C. O'Donovan, M. Magrane, Y. Alam-Faruque, E. Alpi, R. Antunes, J. Arganiska, E. B. Casanova, B. Bely, and Others, "Update on activities at the Universal Protein Resource (UniProt) in 2013," *NUCLEIC ACIDS RESEARCH*, vol. 41, no. D 1, pp. D43—D47, 2013.
- [21] D. B. Wetlaufer, "Ultraviolet spectra of proteins and amino acids," *Adv. Protein Chem*, vol. 17, pp. 303–390, 1962.
- [22] I. Georgakoudi, I. Tsai, C. Greiner, C. Wong, J. Defelice, and D. Kaplan, "Intrinsic fluorescence changes associated with the conformational state of silk fibroin in biomaterial matrices.," *Optics express*, vol. 15, pp. 1043–1053, feb 2007.
- [23] Y. P. Meshalkin, "Two-photon absorption cross sections of aromatic amino acids and proteins," *Quantum Electronics*, vol. 536, pp. 536–538, 1996.
- [24] H.-J. Jin and D. L. Kaplan, "Mechanism of silk processing in insects and spiders.," *Nature*, vol. 424, pp. 1057–1061, aug 2003.
- [25] P. Chen, H. S. Kim, C.-Y. Park, H.-S. Kim, I.-J. Chin, and H.-J. Jin, "pH-Triggered transition of silk fibroin from spherical micelles to nanofibrils in water," *Macromolecular Research*, vol. 16, pp. 539–543, aug 2008.
- [26] J. C. Cuq and J. C. Cheftel, "Tryptophan degradation during heat treatments: Part 1 The degradation of free tryptophan," *Food Chemistry*, vol. 12, pp. 1–14, jan 1983.
- [27] M. Drobizhev, A. Karotki, and M. Kruk, "Uncovering coherent domain structure in a series of π -conjugated dendrimers by simultaneous three-

- photon absorption,” *The Journal of Physical Chemistry B*, vol. 108, no. 14, pp. 0–5, 2004.
- [28] Z. Suo, M. Drobizhev, C. W. Spangler, N. Christensson, and A. Rebane, “New fluorophores based on trifluorenylamine with very large intrinsic three-photon absorption cross sections.,” *Organic letters*, vol. 7, pp. 4807–4810, oct 2005.
- [29] V. P. Leppanen, T. J. Haring, T. Jaaskelainen, E. Vartiainen, S. Parkkinen, and J. P. S. Parkkinen, “The intensity dependent refractive index change of photochromic proteins,” *Optics communications*, vol. 163, no. 4, pp. 189–192, 1999.
- [30] R. J. Malone, A. M. Miller, and B. Kohler, “Singlet Excited-state Lifetimes of Cytosine Derivatives Measured by Femtosecond Transient Absorption,” *Photochemistry and photobiology*, vol. 77, no. 2, pp. 158—164, 2003.
- [31] J.-M. L. Pecourt, J. Peon, and B. Kohler, “DNA excited-state dynamics: ultrafast internal conversion and vibrational cooling in a series of nucleosides,” *Journal of the American Chemical Society*, vol. 123, no. 42, pp. 10370–10378, 2001.

Chapter 4

Multiphoton micromachining in silk

In Chapter 3 it was shown that silk has a 3-photon cross-section that is unexpectedly large given the amino acid composition of the protein. It was hypothesized from that research that silk might be an attractive material for photoinitiator-free multiphoton patterning. In this chapter, the concept of multiphoton micromachining in silk hydrogels is introduced, and a mechanism by which voids can be produced via multiphoton absorption proposed. The development of a finite-element model that estimates the absorbed energy within the silk gel and is capable of predicting the volume of the voids that are produced under different exposure conditions is also discussed. Finally, the use of ultrashort light pulses to ablate solid silk to create diffractive structures is described.

In 2014 a new class of transparent silk hydrogels was developed that are easily formed by adding horseradish peroxidase and hydrogen peroxide to a silk solution [1]. The result is an elastic gel with exceptional transparency to visible light. By focusing ultrashort pulses of near infrared light into the

hydrogels a visible mark could be formed within the gel (Figure 4.1). To confirm that these marks were restricted to the focal volume, side-view images of the marks were collected using a phase contrast microscope. These showed that altering the focal plane of the beam changed the location of the marks within the gel (Figure 4.2, and Figure 5.2). The maximum depth at which features were visible was found to be approximately 1 cm which is more than ten-times deeper than multiphoton void formation reported in other materials [2]. Previous investigations have been limited by self-focusing, when amplified femtosecond pulses are used, or by limitations in working distance due to the need for tight focusing ($NA > 1$). In the phase-contrast images, the marks themselves appeared lighter than the background region indicating a reduction of the index of refraction [3]. These images hinted that the marks were, in fact, voids that had been formed within the gel. This hypothesis was later confirmed both by atomic force microscopy and by seeding cells on a gel that had been exposed to the laser and observing cellular infiltration into the laser-produced features [4]. These experiments are detailed in Chapter 5.

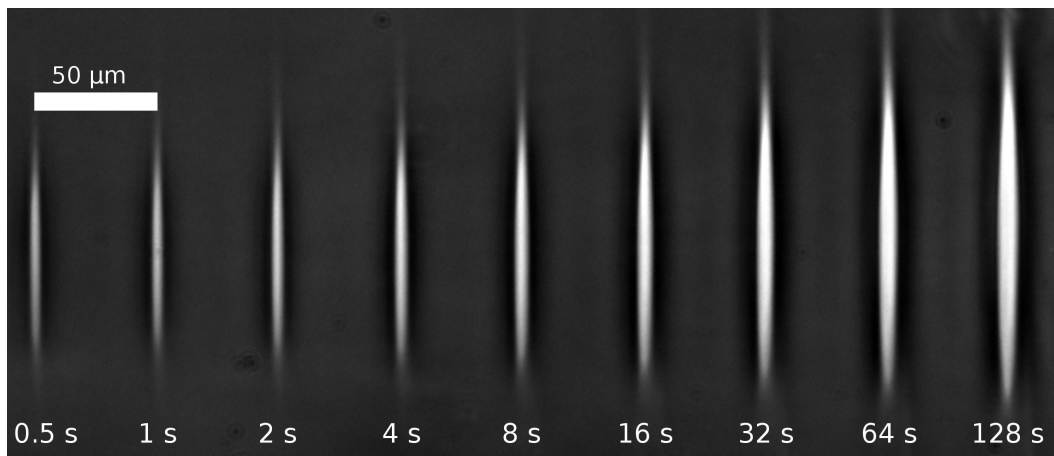


Figure 4.1: Side view of marks made in a silk hydrogel after exposure to varying numbers of ultrashort pulses taken with a phase contrast microscope. Laser was incident from the bottom of the image.

Multiphoton-induced void formation has been previously investigated in

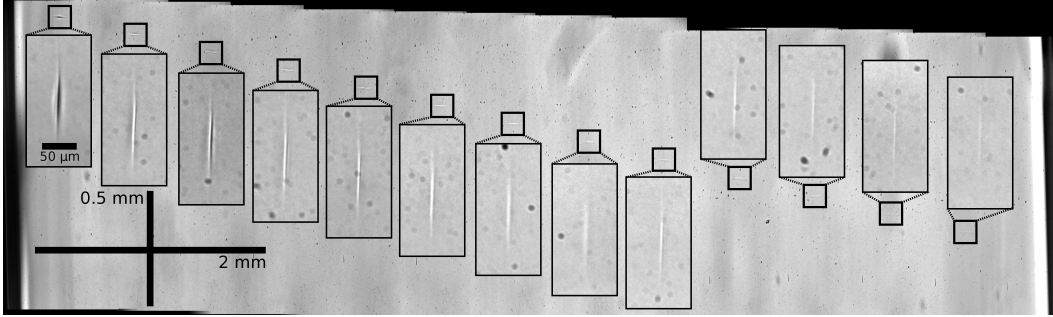


Figure 4.2: The laser was incident from the left to create voids at different depths below the surface of the gel. Each small square indicates the location of the feature and the large rectangles are zoomed in versions of the indicated square. Due to the large area this image is stitched together from several individual images.

optical materials such as fused silica [5, 6, 7]. At high pulse repetition-rate using low energy pulses the mechanism of void formation in glass has been determined to be due to thermal accumulation. It was discovered that the heat produced from the absorption of a single optical pulse does not have sufficient time to diffuse out of the focal volume before the arrival of a subsequent pulse. This leads to a build up of energy at the focal spot eventually leading to the melting or evaporation of the material [8, 5, 9]. In biological materials, heat accumulation does not seem to play a significant role as the energies needed to ablate tissue are too low to induce significant heating. It is hypothesized that these materials are chemically disrupted by a low-density plasma that forms at the focus of the beam [10].

Qualitatively, the voids appear to grow more quickly along the optical axis than radially. This anisotropy hints that, unlike in glass, the diffusion of heat or other photoproducts probably does not play a significant role in void formation. Observing the voids, it appears that they roughly follow the shape of a focused beam. These qualities imply that the void formation is due directly to absorbed light energy and thus could be modeled computationally by deriving an expression for energy absorption in a focused Gaussian beam.

4.1 Model development

Having a computational model of void formation would be useful for two main reasons. First, it would provide information about the process of void formation (i.e. its mechanism, and the order of the nonlinear process). Second, it would provide a rapid way to test various focusing and exposure conditions to optimize the micromachining process. To develop the model a cylindrical coordinate space where z denoted the optical axis and r represented the radial distance from that axis was defined. Under this coordinate system, each voxel is a ring with area $2\pi r dr$ and height dz where dr and dz are the mesh spacing in the r and z directions respectively. Using the Gaussian beam equation [12] the intensity can be written as:

$$I(r, z, t) = \frac{2P(t)}{\pi w_z^2} \exp\left(\frac{-2r^2}{w_z^2}\right) e^{-\alpha d} \quad (4.1)$$

Where $P(t)$ is the instantaneous power, w_0 is the beam HW(1/e²)M waist, w_z is the beam radius at position z given by: $w_z = w_0 \sqrt{1 + (\frac{z}{z_R})^2}$. Where z_R is the Rayleigh range defined as $z_R = \frac{\pi w_0^2}{\lambda}$. The $-\alpha d$ term represents losses due to scattering and linear absorption within the gel where d is the depth of the focal plane below the surface of the gel.

For a pulse that is temporally sech^2 , the instantaneous power is:

$$P(t) = 0.88 \frac{E_p}{\tau_p} \text{sech}^2(1.76t/\tau_p) \quad (4.2)$$

E_p and τ_p are the pulse energy and temporal pulse width (FWHM) respectively. The above equations allowed the intensity at any point in space and time to be determined provided the beam waist (w_0), pulse width (τ_p), and pulse energy (E_p), and linear absorption (α) were known (Figure 4.3). As-

Simulated Intensity

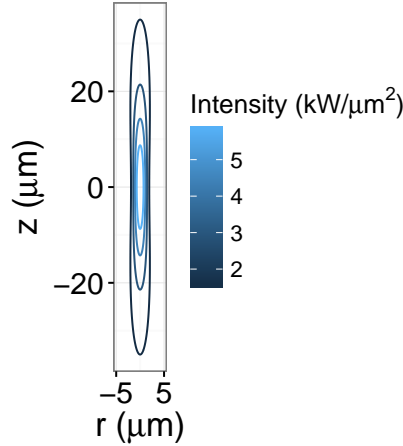


Figure 4.3: Map of the spatial intensity of a Gaussian focused beam made by solving Equation 4.1

suming a purely 3-photon absorption process, the change in intensity during propagation is:

$$dI = \frac{\sigma(\lambda)I^3 N_0 dz}{(h\nu)^2} \quad (4.3)$$

Where, $\sigma(\lambda)$ is the molecular 3-photon coefficient, N_0 is the number of absorbing molecules in the irradiated volume, and $h\nu$ is the photon energy. An expression for the energy absorbed can be written by substituting the intensity from Eq. 4.1, and multiplying by both the area over which the intensity is present and by time.

$$E = \sigma(\lambda) \frac{8P(t)^3}{\pi^3 w_z^6} \exp\left(\frac{-6r^2}{w_z^2}\right) e^{-3\alpha d} \left(\frac{N_0}{(h\nu)^2}\right) 2\pi r dr dz \quad (4.4)$$

In the above equation the area of each voxel experiencing the intensity at a point r (assuming that dr is small relative to r) is $2\pi r dr$. To find the energy absorbed during a single ultrashort pulse Equation 4.4 is integrated over all time. In reality the sample is exposed to a train of pulses, but calculating

the energy absorbed per pulse and multiplying by the number of pulses yields the total absorbed energy in the exposure. Practically, the pulse repetition frequency multiplied by the exposure time is used to calculate the number of pulses incident on the sample.

$$\frac{E_{abs}}{\text{pulse}} = \frac{8\sigma(\lambda)}{\pi^3 w_z^6} \exp\left(\frac{-6r^2}{w_z^2}\right) e^{-3\alpha d} \left(\frac{N_0}{(h\nu)^2}\right) 2\pi r dr dz \times 0.68 \left(\frac{E_p}{\tau_p}\right)^3 \int_{-\infty}^{\infty} \text{sech}^6(1.76t/\tau_p) dt \quad (4.5)$$

The integral has an analytical solution which, when substituted into the above equation yields an expression for the absorbed energy per pulse:

$$\frac{E_{abs}}{\text{pulse}} = \frac{\sigma(\lambda)N_0}{(h\nu)^2} \times \frac{8}{\pi^3 w_z^6} \exp\left(\frac{-6r^2}{w_z^2}\right) e^{-3\alpha d} 2\pi r dr dz \times 0.68 \left(\frac{E_p}{\tau_p}\right)^3 \frac{16\tau_p}{(15 * 1.76)} \quad (4.6)$$

The model can also be easily modified for pulses with a Gaussian temporal pulse shape. In this case the instantaneous power is:

$$P(t) = 0.94 \frac{E_p}{\tau_p} \exp\left(\frac{-t^2}{\tau_p/4\sqrt{2\ln(2)}}\right) \quad (4.7)$$

After cubing and integration over time the temporal term of Equation 4.6 becomes:

$$\int_{-\infty}^{\infty} P(t)^3 dt = .83 \left(\frac{E_p}{\tau_p}\right)^3 \frac{\tau_p}{2\sqrt{2\ln(2)}} \sqrt{\frac{2\pi}{3}} \quad (4.8)$$

For each spatial location (r, z) the absorbed energy can be calculated (Figure 4.4 provided some basic information about the sample and the laser and sample are known).

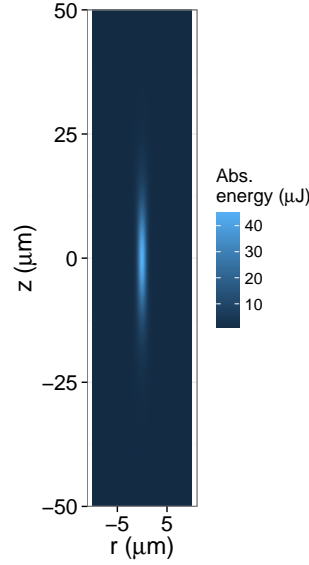


Figure 4.4: Spatial map of absorbed energy made by solving Equation 4.6

When solving Equation 4.6 the amount of energy in each voxel is calculated. However, the volume of each voxel changes depending on the r position. Recall that $V = 2\pi r dr dz$, where dr and dz are the distance between points in the finite element space. Since the volume is changing, the number of absorbers (N_0) is also changing. To calculate the number of silk molecules in each voxel the following equation is used:

$$N_0 = \frac{c_{sf} * 2\pi r dr dz}{m_{sf}/N_A} \quad (4.9)$$

Where c_{sf} is the concentration of silk in the gel, m_{sf} is the molar mass of silk, and N_A is Avogadro's number. The molecular weight of silk depends on the amount of time it is boiled for during sericin extraction. For all of the following studies an extraction time of 60 minutes was used which translates to a molecular weight of approximately 55 kDa [13]. To determine if the voxel has become a void a critical energy (E_c) that must be absorbed in order to denature a single silk molecule was defined. If $E_{abs} > E_c * N_0$ in a voxel it is marked as a void (Figure 4.5). To calculate the total volume that has been removed,

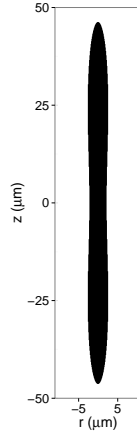


Figure 4.5: Map of the void shape assuming $E_c=80$ pJ/molecule.

the volume of each voxel marked as a void is summed together. Interestingly, the number of absorbers increases the energy absorbed, but also means more energy must be absorbed to become a void canceling out its effects, implying that void formation is independent of silk concentration in the gel. The model outlined above was implemented as a function in the R Programming language [14]. The full function can be found in Appendix A.

4.2 Validating the model

In order to test the performance of the computational model in the previous section, it was necessary to see if the model could explain the observed variation in void size. In order for predictions to be made, the molecular three-photon cross-section (σ), scattering coefficient (α), depth of the focal plane below the surface (d), pulse energy (E_p), pulse width (τ_p), wavelength (λ), and beam waist (w_0) must be known. A reliable method of measuring the size of the voids must also be developed.

4.2.1 Sample preparation

In order to facilitate imaging of the laser-produced features from all sides, gels were formed inside polystyrene “semi-micro” spectrophotometer cuvettes. Each cuvette was filled with 700 μL of silk solution filtered through a 0.22 μm pore filter. The silk used in these experiments was boiled for 60 minutes prior to dissolution in lithium bromide. The 60 minute boil time has improved optical properties and improved stability over silk solutions extracted for shorter amounts of time [15]. 7 units of type VI horseradish peroxidase was added to the solution and mixed thoroughly. Finally 7 μL of 1% hydrogen peroxide was added to the cuvette and mixed thoroughly. The cuvette was then sealed with Parafilm® to prevent evaporation and set aside for at least 3 hours to allow the gelation reaction to complete.

4.2.2 Feature measurement

It is clear from figure 4.1 that the more pulses the material is exposed to, the larger the features that will be produced. In order to quantify how the feature size changes under different conditions it is necessary to measure the feature size in a standardized way. After exposing the gels to the laser, side-view images were collected using the 20x objective of a phase-contrast microscope. These images were subsequently imported into ImageJ [11] for analysis. To control for varying lighting conditions, a background gray value was measured by averaging pixels in a region containing only background. The image was then segmented using a value 11% larger than the background value as a threshold. The value of 11% was based on manual segmentation of a randomly selected series of images. Here, a threshold value was set by the analyst as the “best” value. This value was then compared to the average background value. It was found that a value of around 11% brighter than background was most

often chosen during manual segmentation and so was used in all subsequent automatic analysis. Once segmented, a best-fit ellipse was fit to each of the segmented voids and the major and minor axes of the ellipse recorded. To estimate the volume of removed material cylindrical symmetry was assumed and the volume of the ellipsoid calculated: $V = (4/3)\pi Rr^2$. Where V is the volume, R is the length of the semi-major axis, and r is the length of the semi-minor axis. This entire procedure was encapsulated in an ImageJ macro to allow for rapid, semi-autonomous analysis requiring only the selection of a background region by the user. The code for the macro is reproduced in Appendix B. The robustness of the analysis to changes in illumination conditions was tested by imaging a single set of features and varying the exposure time of the imaging camera. The images that were exposed for longer appeared brighter than the images with a shorter exposure time. The volume of the features was estimated using the ImageJ macro to estimate the ability of the macro to deliver a consistent estimation of void volume under variable lighting conditions. For a range of features, the calculated void size was nearly identical no matter what the exposure time was set to (Figure 4.6) indicating that the method of segmenting the images relative to the average background value is robust to changes in exposure time. The only exception to this is the case of extremely long exposures where the pixels become saturated.

4.2.3 Parameter measurement

The molecular three-photon cross-section of silk solution at 810 nm was determined in Chapter 3 to be $\sim 5 \times 10^{-77} \text{ cm}^6 \text{ s}^2 \text{ photon}^{-2}$. The scattering coefficient was measured to be 0.05 mm^{-1} by measuring the change in transmitted intensity of a low-power, continuous-wave, 532 nm laser beam through first the short arm (5 mm) and then the long arm (10 mm) of the spectropho-

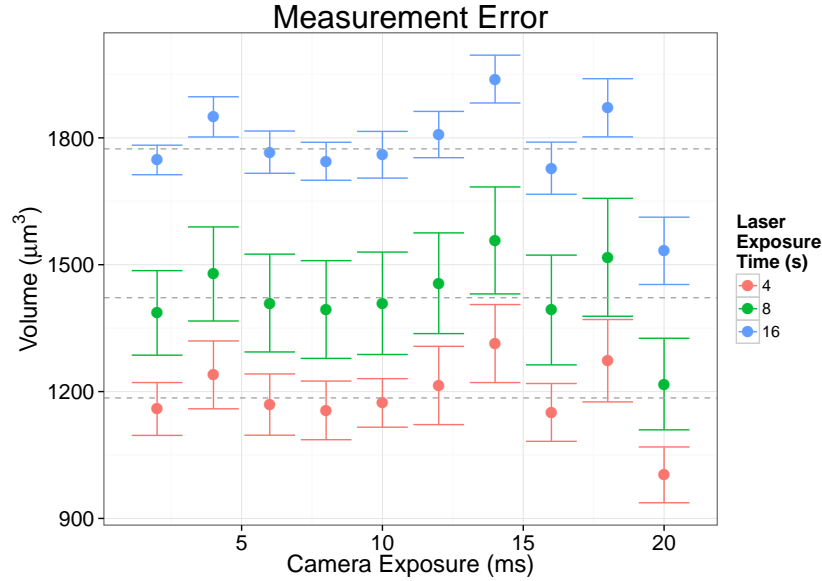


Figure 4.6: Plot showing estimated void volumes given various imaging exposure times. The dotted line indicates the average for each laser exposure condition. Error bars represent 1 standard deviation ($n=3$). Decrease in volume at 20 ms is due to pixel saturation.

tometer cuvette. The scattering coefficient could then be calculated using the difference in transmission over the known distance. There is negligible linear absorption in silk at 532 nm, so the power lost was likely due to scattering within the gel.

The depth of the focal plane below the surface of the gel was controlled by adjusting the distance between the the microscope objective and the sample. At the start of each session the laser was focused on the outer wall of the cuvette. The depth of focus was set relative to the outer wall of the cuvette by rotating the focus knob a fixed number of rotations.

4.2.4 Pulse repetition frequency

The pulse repetition frequency is constantly monitored by the laser’s “Lock-to-clock” electronics and can be changed by adjusting the cavity length of the laser. Each day the pulse repetition frequency was set to 80.00 MHz.

4.2.5 Pulse energy

The pulse energy was measured by measuring the average power using a pyrometer type power meter and dividing by the pulse repetition frequency. This method of measuring pulse energy assumes that there is no light emitted between pulses.

$$E_p = \frac{P_{ave}}{f_{rep}} \quad (4.10)$$

4.2.6 Pulse width

The temporal pulse width was measured using a background-free autocorrelator [16] illustrated schematically in Figure 4.7. The first stage of the autocorrelator uses a beamsplitter (BS) to produce two copies of an incoming pulse. One copy is reflected from a flat mirror and is directed by the splitter to a parabolic mirror. The other copy is reflected from a corner cube retroreflector glued to a speaker coil. When supplied with an AC voltage the speaker coil moves back and forth changing the pathlength of the light along this arm. The second pulse copy is incident on the parabolic mirror, slightly offset from the first copy. The parabolic mirror focuses the two beams within a thin β -barium borate (BBO) crystal. When exposed to high peak intensity laser pulses and properly phase matched, the BBO crystal produces blue light at half the wavelength of the incoming radiation in a process known as second harmonic generation (SHG). When the pulses from both arms overlap inside the crystal, interference leads to the production of a third beam of SHG light that propagates at an angle halfway between the angle of the two interfering beams. After filtering out the residual NIR light, this third beam is focused onto a detector to measure the intensity of the SHG light produced while the original two beams are blocked. When the pulses do not overlap inside the crystal this third beam is not present. The intensity of the SHG light is pro-

portional to the peak intensity of the light inside the crystal. When the two pulses perfectly overlap (i.e. the pathlength difference between the two arms is zero) the maximum amount of SHG light is observed. As the pathlength difference increases, the peak intensity inside the crystal is lower, and a reduction in SHG signal is observed. If the displacement of the retroreflector is known, the amount of time the two pulses overlap inside the crystal can be derived from the SHG signal on the detector.

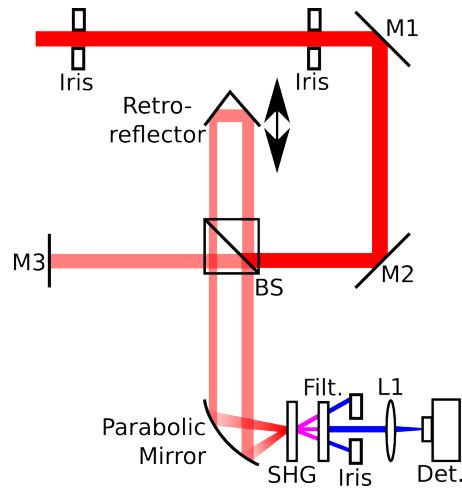


Figure 4.7: Schematic diagram of background-free autocorrelator for ultra-short pulse measurement. The incoming beam is split into two arms one of which moves periodically. The beams are interfered inside a second harmonic generating crystal. When the pulse copies overlap the SHG intensity is at a maximum.

A function generator was used to supply voltage to the speaker coil using a sine-wave pattern with a peak-to-peak voltage of 3 V and a frequency of 3 Hz. The maximum displacement of the speaker coil was measured using a micrometer by translating the reference mirror until the maximum SHG signal was seen at the positive and negative voltage peaks. The maximum SHG signal occurs when the pathlength difference is zero, so noting the micrometer position at both extremes yields the total displacement of the speaker coil during one cycle. The speaker coil displacement can then be written as:

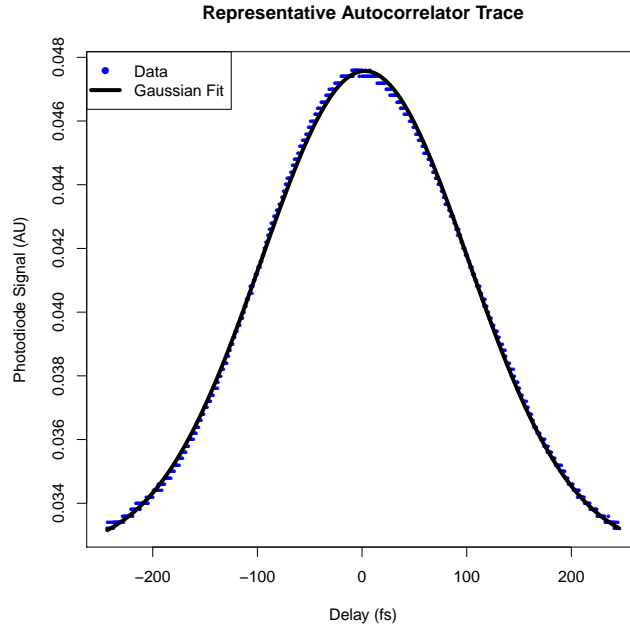


Figure 4.8: Raw SHG signal (points) and Gaussian fit to those points (line) of a ~ 160 fs pulse.

$$d = D \sin(2\pi ft) \quad (4.11)$$

where D is the total displacement of the speaker, f is the frequency of oscillation, and t is the time. The delay between copies of the pulse, then is:

$$t_d = \frac{2d}{c} \quad (4.12)$$

where c is the speed of light in air and the factor of 2 accounts for the fact that the light must travel the length of the interferometer arm twice. The SHG signal from the detector can be plotted vs. the delay time to measure the pulse width (Figure 4.8). This curve was then fit with a Gaussian function to estimate the width of the autocorrelator trace. Depending on the pulse shape the pulse width can be related to the autocorrelator trace by a constant factor: 0.707 for a Gaussian pulse or 0.65 for a sech^2 pulse.

4.2.7 Spot size

The spot size of the beam was measured using the knife edge technique. This technique involves translating a razor blade across the path of the beam and measuring the transmitted power. The width of the beam can be determined from the known position of the knife edge and the transmitted intensity. A 3-axis translation stage (Ludl Electronic Products, Hawthorne, NY) was used to translate the knife edge across the beam in increments of 1 μm . The transmitted power was measured using a power meter from ThorLabs (PM100D) with a silicon photodiode probe protected with a neutral density filter. The translation stage and recording of the power was coordinated using LabView. Prior to focusing, a 2x telescope was used to expand the beam to a diameter that fully filled the back aperture of the microscope objective to minimize the spot size. A representative knife edge plot is presented in Figure 4.9. For an accurate estimation of the beam waist the knife edge must intersect the narrowest portion of the beam. To ensure that this plane was measured the microscope objective was translated along the optical axis in both directions and the minimum measured spot size was used. The raw transmitted power has the shape of an error function, the derivative of which is a Gaussian. To find the beam width, the numerical derivative of the error function was taken and fit it with a Gaussian curve. From the Gaussian, the FWHM could be easily calculated and the $\text{HW}(1/e^2)\text{M}$ beam waist derived from the FWHM.

4.2.8 Determining critical energy

Qualitatively, the simulated features produced by the model are very similar to the phase contrast images (Figure 4.10). For a quantitative determination of the energy needed to disrupt a silk molecule (E_c), the laser and sample parameters must be measured using the techniques above. Once these are

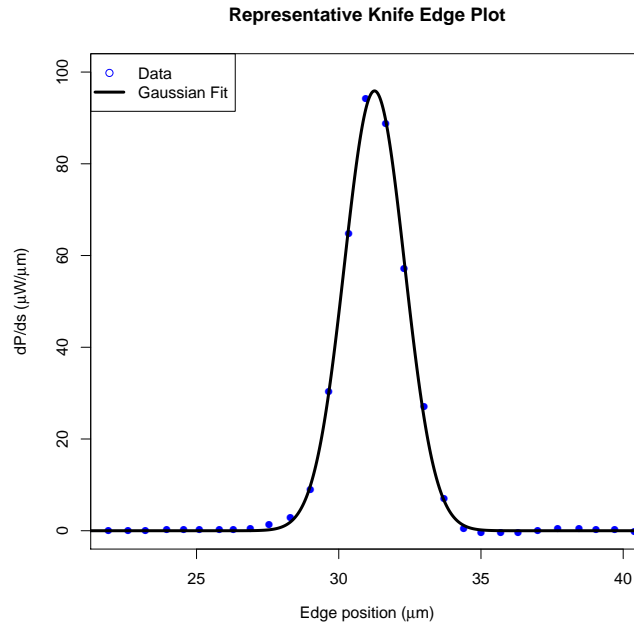


Figure 4.9: Change in transmitted power with displacement of a $2.5 \mu\text{m}$ FWHM spot measured with a power meter (points) and a Gaussian fit of the data (line).

known, E_c is the only floating parameter in the model. To estimate that energy, the volume of the laser produced voids was measured at pulse energies of 5, 10, and 15 nJ and exposure times ranging from 1 to 64 seconds. To account for day-to-day and gel-to-gel variation a fresh gel was made and exposed each day for 6 consecutive business days. Prior to the exposure the wavelength and pulse repetition rate were verified, and the pulse width measured. The average power was measured prior to each set of exposures. The depth was set to 2.06 mm below the surface of the cuvette. Labview was configured to expose 3 locations to 1 s, 2 s, 4 s, 8 s, 16 s, 32 s and 64 s of light. After each set of exposures the pulse energy was checked to ensure it had not drifted from the originally set value. Once exposed, images of the features were collected and measured as previously described. For analysis, the average of the three locations exposed to one set of conditions was taken as the “gel average.” The

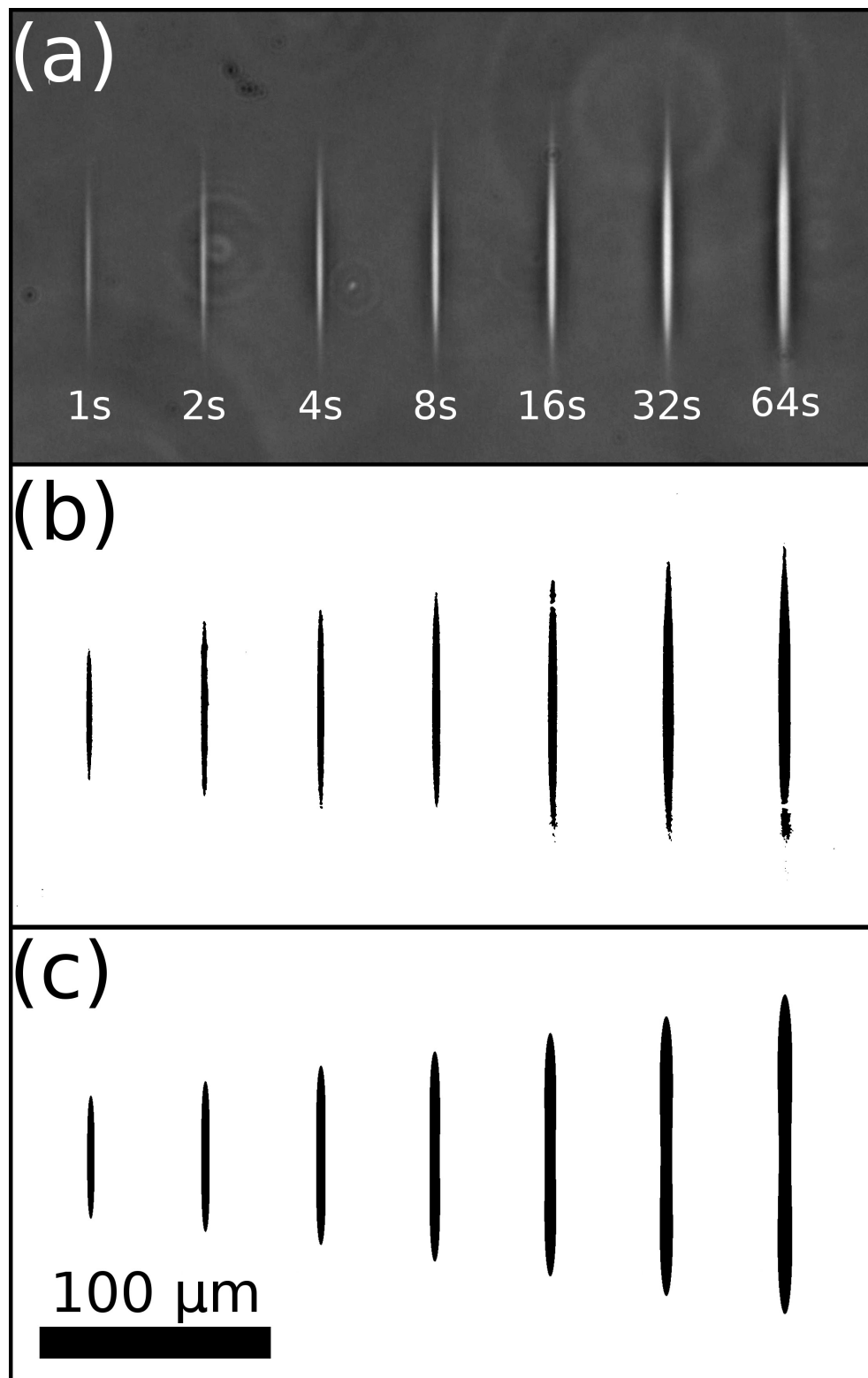


Figure 4.10: Qualitative view of the laser produced features (A), the segmented laser produced features (B), and the simulated voids (C).

6 gel averages were averaged together to obtain an estimate for the average removed volume of material. The critical energy was selected to minimize the weighted root mean squared error (WRMSE) between the measured, and simulated volumes (Figure 4.11). The samples were weighted based on the inverse of the variance of the data under each set of conditions:

$$WRMSE = \sqrt{\frac{1}{n} \sum_{i=1}^n \frac{1}{\sigma_i^2} (\hat{Y}_i - Y_i)^2} \quad (4.13)$$

Where σ_i^2 is the variance of the measured volume, \hat{Y}_i is the estimated volume based on a specific value of E_c , and Y_i is the measured volume under each set of conditions i . The $WRMSE$ was calculated for a range of critical energies to find the minimum (Figure 4.12). Using this procedure we estimated the energy that must be absorbed to denature a single silk molecule was 56 pJ/molecule.

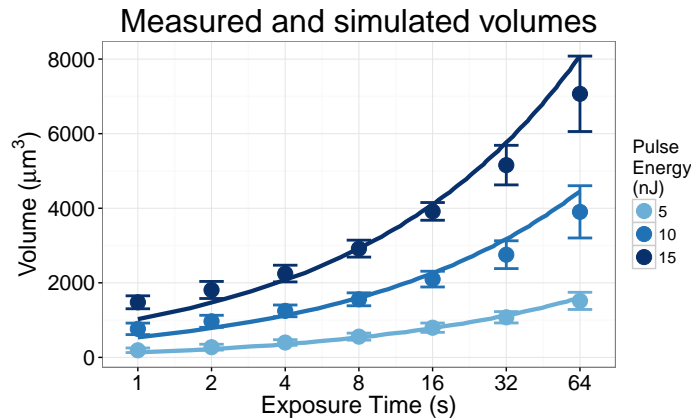


Figure 4.11: Measured feature volumes (points) and the simulated volumes (lines) for varying pulse energies and exposure times. Volumes were calculated using $E_c = 71$ pJ/molecule. Note that the x-axis is presented on a log scale. Error bars are +/- one standard deviation ($n=6$).

To verify the robustness of this analysis the data were split into two groups. In the first case, gels 1-3 were used to estimate E_c . This value for E_c was used to predict the removed volumes for the second set of gels. This procedure was then repeated in reverse. E_c was estimated from the second set of gels and

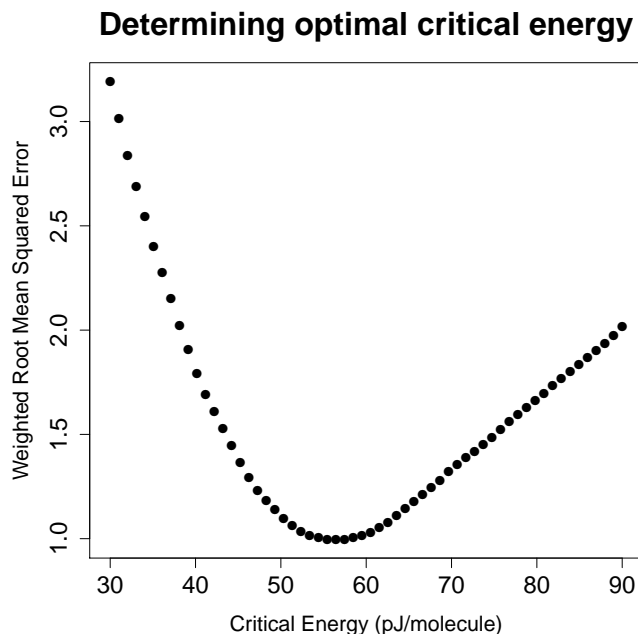


Figure 4.12: Plot showing the weighted root mean squared error as a function of critical energy. The best fit of E_c to the data is found where the error is minimized.

then used to predict the volumes of the first set. The optimum value for E_c using all the data was 56 pJ/molecule. When only the first 3 gels were used the optimum value of E_c was found to be 55 pJ/molecule. When only the second 3 gels were used, the optimum value of E_c was 60 pJ/molecule (Figure 4.13). The fact that even data not included in the model can be predicted is an indication of the robustness of the modeling process.

4.2.9 Wavelength

The absorption spectrum of materials varies with wavelength. To determine the efficiency of void formation across the NIR spectrum, gels were exposed to various wavelengths of light and the void size measured. The gels were exposed to 10 nJ pulses of wavelengths ranging from 740 to 880 nm. Three gels were exposed on 3 different days to account for day-to-day variation. Prior

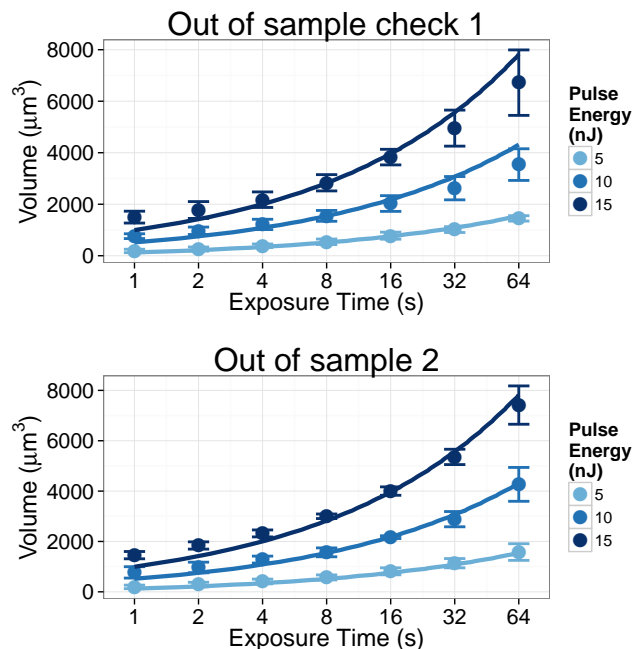


Figure 4.13: Results of splitting the 6 gels into groups of 3. Half the data was used as a training set to determine E_c and then fit to the other half of the data.

to each exposure, the power, pulse width, and repetition rate were checked. After exposure, the voids were measured according to the protocol described above. There were significant differences in the void size as a function of wavelength (Figure 4.14) with 740 nm light producing the largest voids in the material, while 800 nm light produced the smallest all else being equal. There was an intermediate increase in efficiency of machining at 810-820 nm. It is possible that wavelengths shorter than 740 nm result in even more efficient micromachining, but these wavelengths were unavailable due to the limited bandwidth of the mirrors inside the laser cavity.

4.3 Prediction

The ability to accurately model the formation of voids inside silk hydrogels makes it possible to sweep through various parameters quickly *in silico* in

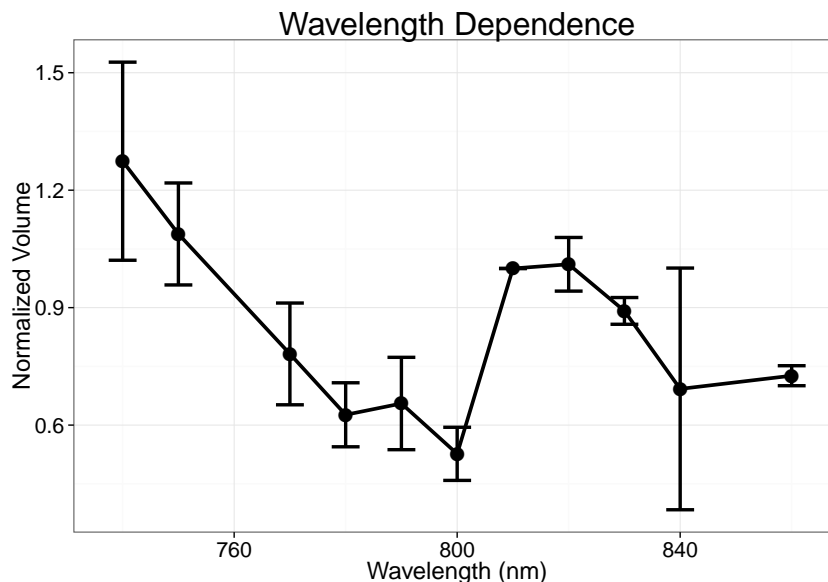


Figure 4.14: Plot showing normalized void size upon exposure to different wavelengths of light. Voids were normalized to 810 nm and error bars indicate ± 1 standard deviation ($n=3$).

order to maximize resolution or efficiency. Parameters such as pulse energy and exposure time have been fully explored in previous sections. This section focuses on parameters that are more difficult to vary experimentally. The first such is the influence of pulse width on void size. Unsurprisingly, the shorter pulses lead to the prediction of larger voids all else being equal (Figure 4.15). The higher peak intensity of very short pulses leads to increased energy absorption in the gel.

The effect of spot size and pulse energy also bears further investigation. If the goal is to maximize the volume of material removed there is a trade off between high optical intensity and large focal volume. With relatively loose focusing the peak intensity within the focal volume is reduced, but the focal volume is large. Conversely with very tight focusing extremely high intensity can be produced, but only within a small volume. To remove material most efficiently, both the spot size and pulse energy must be considered. As pulse

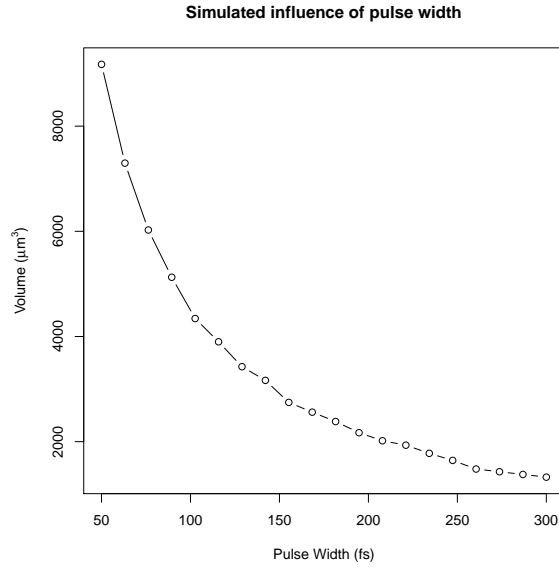


Figure 4.15: Simulated effect of pulse width on void size. Model assumed 10 nJ pulses exposed for 10 s.

energy increases, it is more efficient to use less tight focusing while lower pulse energies require a tighter focus (Figure 4.16).

4.4 Micromachining in solid silk

Micromachining is not limited to silk hydrogels. Even solid forms of silk, such as silk films, are amenable to laser processing. This section outlines one example of the laser machining of diffractive structures in silk films to create “optical vortexes.” An optical vortex is a donut shaped beam of light that is rotating about the axis of propagation. Interestingly, these beams carry orbital angular momentum and, when focused, can be used to rotate microbeads in a manner analogous to optical tweezers. This ability to rotate trapped particles has given rise to the name “optical spanners” to describe these beams. Mathematically, these beams can be described by solving the paraxial wave equation in cylindrical or polar coordinates resulting in “Laguerre-Gaussian” modes.

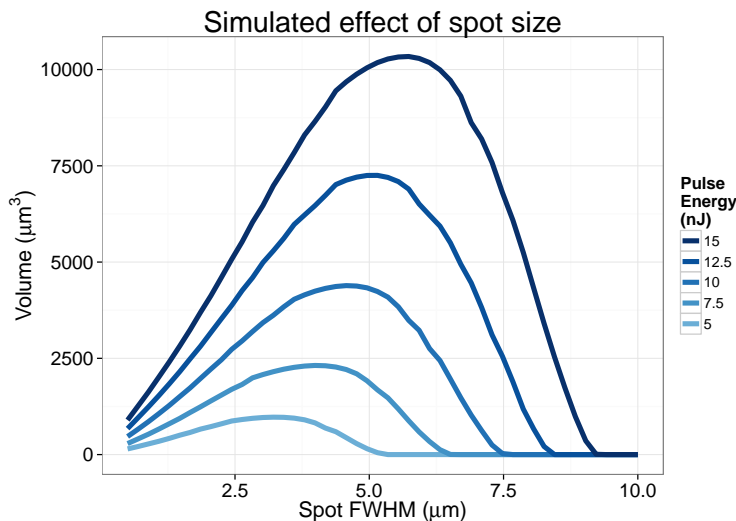


Figure 4.16: Simulated effect of the spot size and pulse energy on void volume. As pulse energy increases the optimal spot size for maximum material removal shifts to less tight focusing indicating a trade off between high optical intensity and large focal volume.

The creation of optical vortex beams can happen inside a laser cavity or can be produced via diffraction. Suitable diffractive structures can be generated by simulating the interference between a plane wave and a Laguerre-Gaussian beam (Figure 4.17). By passing a plane wave through this computer generated hologram (CHG), an optical vortex is the result.

A thin layer of silk was used to ensure high fidelity transfer of the CHG pattern. Spin coating was used to ensure a uniform layer of silk to minimize optical distortion. Briefly, 200 μL of 3% w/w silk solution was deposited on a glass slide and mounted on a spin coater. The silk was spread by rotating at 600 rpm for 30s, followed by 2 minutes of rotation at 2000 rpm. The result was an evenly spread thin layer of silk that was approximately 1 μm thick. When ultrashort pulses of 810 nm light were focused on the sample the silk was ablated away leaving behind clean glass. To create the optical vortexes out of silk the CHG was programmed into an XY translation stage synchronized with a mechanical shutter. The stage rastered over the image and the shutter

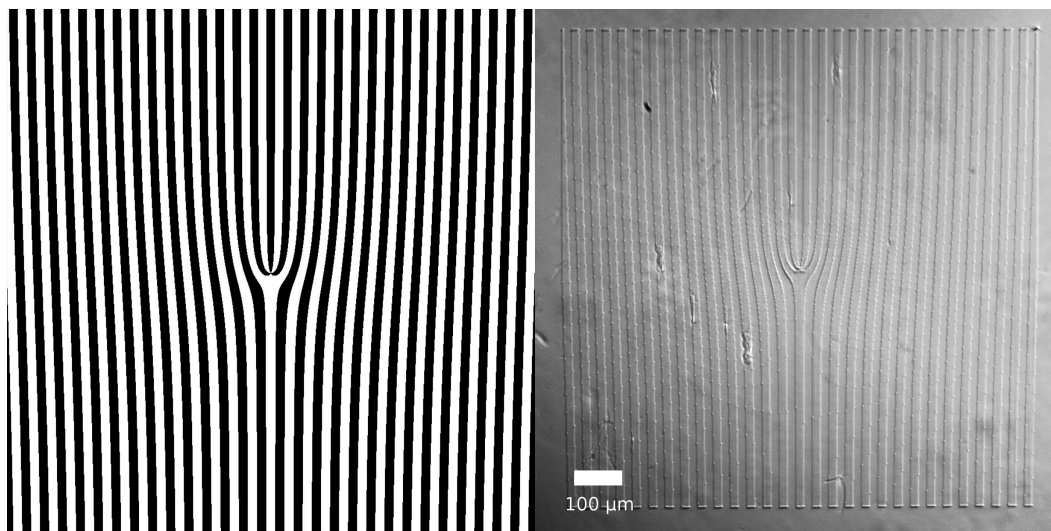


Figure 4.17: Computer generated hologram of 3rd order Laguerre-Gaussian beam interfering with a plane wave (left). The same pattern micromachined into a silk film (right).

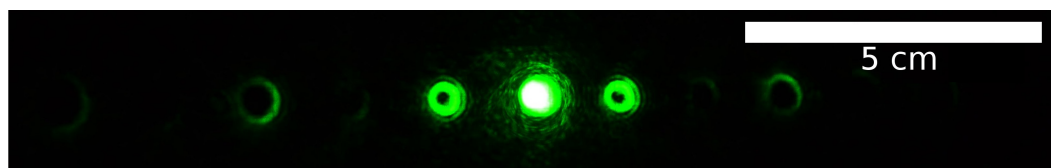


Figure 4.18: Photograph showing the diffraction pattern when a laser is passed through the patterned silk film shown in Figure 4.17.

exposed all of the white pixels to the laser, remaining closed for the dark pixels.

To test the fidelity of pattern transfer, a low powered green laser was passed through the pattern machined into the silk and the result was, as expected, a series of optical vortex beams including a central Hermite-Gaussian spot (Figure 4.18). These patterns could be subsequently transferred to polydimethylsiloxane (PDMS) by casting the PDMS onto the silk surface. After curing, the resulting diffraction pattern was identical, indicating accurate pattern transfer. This application illustrates how versatile multiphoton micromachining can be. Arbitrary patterns can be directly written into silk and easily transferred to other materials. This enables rapid prototyping of any 2D structure and can be used to generate master masks from PDMS or other materials. The large

multiphoton cross-section of silk enables this patterning to be done rapidly and, theoretically, with nanometer resolution.

4.5 Conclusion

The finite element model described in this chapter is useful for predicting void volume, revealing the physical underpinnings of void formation, and for optimizing exposure conditions to maximize volume removed or optimize resolution. Using this model, the void volume can be predicted provided information about the focusing and laser exposure conditions are known. The model was tested across a wide variety of exposure times and pulse energies to demonstrate the predictive value of this modeling method. The model was also used to estimate the amount of light energy that must be absorbed to denature a single silk molecule. Based on this work, it appears that value was approximately 60 pJ/molecule. Furthermore, the fact that this model accurately predicts void volume over such a wide range of conditions can help determine the physical processes at work during void formation. Unlike in glass, there was no evidence that pulse repetition frequency had an effect on void size. This allowed us to rule out the diffusion of heat, free radical species, or other photoproducts as a mechanism. Although it is likely that thermal deposition does occur, we believe the silk molecules cease to absorb energy from the laser once they are denatured. This limits the amount of heat deposited and limits the impact of heat diffusion. It is also possible that direct photochemical denaturation is occurring. Future work will examine exposed gels for degraded silk photoproducts to determine if direct chemical effects are responsible for void formation. Finally, the use of this model shows that at the pulse energies and wavelengths examined the nonlinear absorption in silk is purely a 3-photon

process, since accurate predictions can be made using only I^3 scaling.

Unlike other modeling techniques such as finite difference time domain simulations, the model described here is very computationally efficient. Using only a single thread of an Intel i7-2600 desktop PC, the average time needed to calculate the volume of a void is 77 ms. This allows large numbers of conditions to be tested extremely rapidly and fully optimized in a matter of minutes. Currently the model is only implemented for Gaussian focusing. However, it may be that other focusing geometries (Bessel beams, multifocal beams, etc.) yield more efficient material removal. This model can be easily extended to these more esoteric focusing geometries. In the next chapter the micron scale voids described here are linked together to form larger structures that are subsequently used to guide cell growth.

Bibliography

- [1] B. P. Partlow, C. W. Hanna, J. Rnjak-Kovacina, J. E. Moreau, M. B. Applegate, K. A. Burke, B. Marelli, A. N. Mitropoulos, F. G. Omenetto, and D. L. Kaplan, “Highly Tunable Elastomeric Silk Biomaterials,” *Advanced Functional Materials*, pp. 4615–4624, apr 2014.
- [2] M. Oujja, S. Pe’rez, E. Fadeeva, J. Koch, B. N. Chichkov, and M. Castillejo, “Three dimensional microstructuring of biopolymers by femtosecond laser irradiation,” *Applied Physics Letters*, vol. 95, no. 26, p. 263703, 2009.
- [3] F. Rost and R. Oldfield, *Photography with a Microscope*. Cambridge University Press, 2000.
- [4] M. B. Applegate, J. Coburn, B. P. Partlow, J. E. Moreau, J. P. Mon-

- dia, B. Marelli, D. L. Kaplan, and F. G. Omenetto, “Laser-based three-dimensional multiscale micropatterning of biocompatible hydrogels for customized tissue engineering scaffolds,” *Proceedings of the National Academy of Sciences*, vol. 112, pp. 12052–12057, sep 2015.
- [5] S. Eaton, H. Zhang, P. Herman, F. Yoshino, L. Shah, J. Bovatsek, and A. Arai, “Heat accumulation effects in femtosecond laser-written waveguides with variable repetition rate.,” *Optics express*, vol. 13, no. 12, pp. 4708–4716, 2005.
- [6] a. M. Streltsov and N. F. Borrelli, “Fabrication and analysis of a directional coupler written in glass by nanojoule femtosecond laser pulses.,” *Optics letters*, vol. 26, no. 1, pp. 42–43, 2001.
- [7] G. Della Valle, R. Osellame, and P. Laporta, “Micromachining of photonic devices by femtosecond laser pulses,” *Journal of Optics A: Pure and Applied Optics*, vol. 11, no. 1, p. 013001, 2009.
- [8] C. B. Schaffer, A. Brodeur, J. F. García, and E. Mazur, “Micromachining bulk glass by use of femtosecond laser pulses with nanojoule energy.,” *Optics letters*, vol. 26, no. 2, pp. 93–95, 2001.
- [9] R. R. Gattass, L. R. Cerami, and E. Mazur, “Micromachining of bulk glass with bursts of femtosecond laser pulses at variable repetition rates.,” *Optics express*, vol. 14, no. 12, pp. 5279–5284, 2006.
- [10] A. Vogel, J. Noack, G. Hüttman, and G. Paltauf, “Mechanisms of femtosecond laser nanosurgery of cells and tissues,” *Applied Physics B: Lasers and Optics*, vol. 81, pp. 1015–1047, 2005.
- [11] C. A. Schneider, W. S. Rasband, K. W. Eliceiri, and Others, “NIH Image

- to ImageJ: 25 years of image analysis,” *Nat methods*, vol. 9, no. 7, pp. 671–675, 2012.
- [12] E. Hecht, *Optics (4th Edition)*. Addison Wesley, 4 ed., aug 2001.
- [13] L. S. Wray, X. Hu, J. Gallego, I. Georgakoudi, F. G. Omenetto, D. Schmidt, and D. L. Kaplan, “Effect of processing on silk-based biomaterials: reproducibility and biocompatibility,” *Journal of biomedical materials research. Part B, Applied biomaterials*, vol. 99, pp. 89–101, oct 2011.
- [14] R Core Team, *R: A Language and Environment for Statistical Computing*. R Foundation for Statistical Computing, Vienna, Austria, 2015.
- [15] S. Zhao, Y. Chen, B. P. Partlow, A. S. Golding, P. Tseng, J. Coburn, M. B. Applegate, J. E. Moreau, F. G. Omenetto, and D. L. Kaplan, “Bio-functionalized silk hydrogel microfluidic systems,” *Biomaterials*, vol. 93, pp. 60–70, 2016.
- [16] J.-C. Diels and W. Rudolph, “9 - Diagnostic Techniques,” in *Ultra-short Laser Pulse Phenomena (Second Edition)* (J.-C. D. Rudolph, ed.), pp. 457–489, Burlington: Academic Press, second edi ed., 2006.

Chapter 5

Applications of multiphoton micromachining

5.1 Introduction

The ability to controllably shape soft biomaterials on the microscale in two, and especially three dimensions is important given the ability of these structures to guide cellular growth, differentiation, gene expression, and regeneration [1, 2, 3, 4]. The use of such materials, however, poses challenges in fabrication due to their mechanical characteristics. Widely adopted biomaterial microfabrication techniques such as soft- and photo-lithography are limited to two dimensions. The recent advent of 3D printing technology has exploited the interaction of light with materials to rapidly prototype parts for a variety of industries, and has expanded to significantly impact the biomedical field [5, 6, 7]. Micro-scale 3D printing has also shown promise for tissue engineering and regenerative medicine applications with the eventual goal of printing entire organs [8, 9]. In this chapter, a technique for generating voids as small as $5\ \mu\text{m}$ in diameter within a biocompatible hydrogel using multiphoton ab-

sorption (MPA) of light is described that shares many similarities with 3D printing. Furthermore, this technique functions in the absence of exogenous photoinitiators or chemical crosslinkers, thereby avoiding potentially biologic incompatibility that can otherwise limit the utility of such processes.

MPA is a process that occurs under extremely intense illumination where two or more low-energy photons are absorbed simultaneously by a material Ref. [10] and Section 2.3. To achieve photon densities high enough for MPA, very short laser pulses must be tightly focused within a material. If the material is transparent to the low-energy photons, very little of the light is absorbed at the surface, allowing a focal spot to be formed, and MPA to occur, deep within the material. Multiphoton induced structural modification leading to void formation has been investigated in a variety of biocompatible materials including collagen, poly(vinyl-alcohol) (PVA), poly(methyl methacrylate), and gelatin hydrogels [11, 12, 13]. Poly (ethylene glycol) hydrogels crosslinked with a photolabile bond can be selectively degraded to induce 3D structures [14]. 3D patterning in collagen gels is limited to a few tens of microns below the surface due to scattering [15]. Transparent materials such as PVA have very high threshold power requirements necessitating the use of high numerical aperture objectives, or amplified femtosecond pulses to initiate MPA for void formation. Extremely high light intensities found in these amplified pulses can locally change a material's refractive index resulting in self-focusing of the beam [16]. Self-focusing limits the depth at which a tight focal spot can be formed and has limited MPA induced void formation to less than 200 μm below the surface of the material [12]. Some natural proteins including amyloid [17] and silk fibroin [18] are much more efficient multiphoton absorbers than their amino acid composition would suggest (Chapter 3). The hypothesis here was that the large multiphoton cross-section of these natural materials would

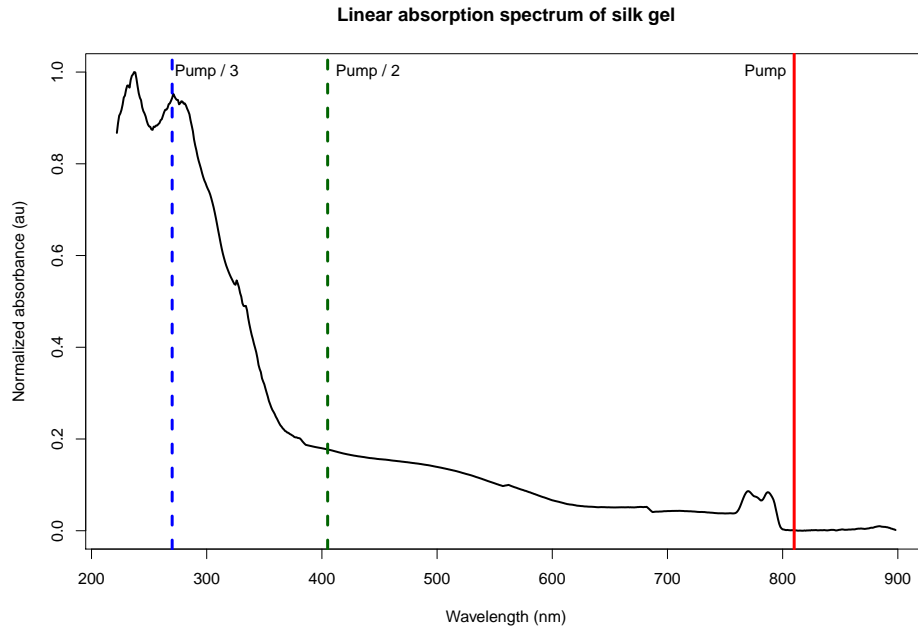


Figure 5.1: Linear absorption spectrum of silk gel with background subtracted. The vertical line at 810 nm indicates the wavelength used for multiphoton micromachining. Pump/2 and Pump/3 lines indicate, roughly, the wavelengths associated with a 2-photon and 3-photon absorption process respectively. Linear absorption is driven by tyrosine and tryptophan residues in the silk. Spectrum was filtered by a 5-point moving average to reduce noise.

allow the initiation of MPA at low threshold powers, potentially reducing the effects of self-focusing and enabling multiphoton micromachining to occur at unprecedented depth.

Silk fibroin collected from the domesticated *Bombyx mori* silkworm has been under steady investigation for decades because of its suitability as a material for biomaterials and tissue engineering. Silk is cytocompatible, biodegradable, and able to stabilize labile compounds such as enzymes and drugs [19]. Silk fibroin has also been studied as a novel optical material due to its transparency to visible light (Figure 5.1), and low surface roughness, giving it the ability to conform to nano-scale structures such as diffraction gratings [20, 21, 22], or to generate 3D photonic crystals [23]. Previous work involving photomodification of silk has thus far only considered surface modification of

dried films [24]. Extending this work into the third dimension requires silk to take on a different form. Recently, a highly transparent elastomeric silk fibroin hydrogel has been developed which is ideally suited to multiphoton laser micromachining (Figure 5.2a inset) [25]. These gels are robust enough to be easily handled, amenable to cell growth, and well tolerated upon implantation. Importantly, these gels are greater than 90% water which allows material disrupted during MPA to be deposited around the outside of the machined region without fouling.

Here, the exploration of laser induced void formation in silk hydrogels is presented. It is found that relatively low energy (sub 2 nJ/pulse) infrared ($\lambda=810$ nm) pulses at a high repetition rate (80 MHz) can be used to form voids within the hydrogels in three-dimensions. The gels have a linear absorption peak at 270 nm suggesting this to be a 3 photon absorption process (Figure 5.1). The voids formed survive the rigors of handling, cell growth, and subdermal implantation. It is possible to form voids within the gels nearly 1 cm below the gel surface which, to our knowledge, represents the greatest depth of multiphoton induced void generation reported, exceeding by 1.5 orders of magnitude the deepest ablation in any material yet tested [12].

5.2 Results

A custom built 3D laser writing workstation was constructed to study multiphoton micromachining (Figure 5.2a). Ultrashort (~ 125 fs) laser pulses at a pulse repetition frequency of 80 MHz were focused into the bulk of a silk hydrogel using a 10x (NA=0.3) microscope objective. The sample was mounted on a 3-axis micropositioning stage. The sample could then be moved so the beam was focused in different locations within the material. Generation of

complex 3D patterns within the material was achieved by computer control over the stage translation.

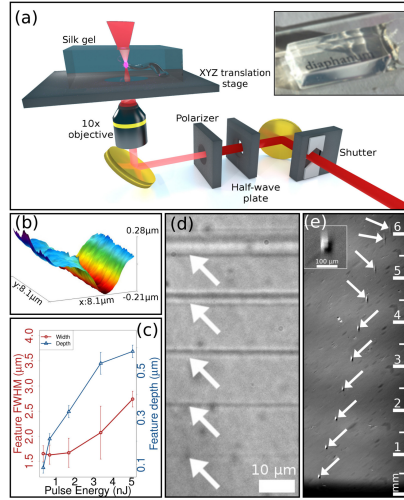


Figure 5.2: Overview of the micromachining process. (a) Schematic of the multiphoton micromachining workstation. The shutter and translation stage are both computer controlled. Inset: Photograph of the silk hydrogel showing high transparency. (b) 3D AFM image of one of the lines in panel (d). (c) Graph relating line dimensions with pulse energy. Error bars represent 1 standard deviation ($n=4$). (d) Microphotograph of lines machined into the upper surface of a silk gel at pulse energies ranging from 0.25 nJ (bottom) to 5 nJ (top). (e) End on view of 30 μm wide lines machined into a silk gel. Light was incident from the bottom of the image. Ruler on right side measures depth from the surface of the sample. Smearing at greater depth was caused by a reduction in write speed resulting in longer exposure time and a greater area of modification. The break in the pattern on the top was due to limits on the vertical travel of the microscope. Due to the large area involved, this image was stitched together from a series of microphotographs. Inset: detail of the cross-section of one line.

The relationship between pulse energy and void size was characterized by micromachining a series of lines on the top surface of a gel approximately 1 mm thick (Figure 5.2d). Each line was made by a single pass of the laser at a constant speed of 50 $\mu\text{m}/\text{s}$ with varying pulse energies. After machining, the lines were imaged via atomic force microscopy (AFM). The minimum pulse energy necessary to observe structural changes in the silk gel was approximately 0.25 nJ/pulse. At this power, the average trench dimensions were 1.5 μm full-width

at half maximum (FWHM) in width and 100 nm in depth. These dimensions increased to 2.5 μm FWHM and 600 nm in depth when the pulse energy was raised to 5 nJ (Figure 5.2c). AFM measurements confirmed that the change in appearance of the machined region was due to material removal and not local changes in refractive index (Figure 5.2b).

The depth at which features could be micromachined was tested by forming a gel inside a polystyrene spectrophotometer cuvette. Features were micromachined inside the gel at various depths and subsequently imaged by rotating the cuvette 90 degrees and examining the features using brightfield microscopy (see also Chapter 4). Visible features were found in the gel up to 8 mm below the surface (Figure 5.2e). Deeper features should be possible using a longer working distance objective with a similar numerical aperture. This large maximum machining depth was attributed to the clarity of the silk and the large multiphoton cross-section of the protein which allows low powered pulses to be used to initiate MPA without significant self-focusing. Using amplified femtosecond pulses, the critical power for self-focusing was estimated to be greater than 6 MW which is more than 100 times more power than is found in the pulses used for micromachining (Figure 5.3). This combination of qualities is, to the best of our knowledge, unique to silk and enables multiphoton micromachining to occur at such extreme depths. Deep, high-resolution features such as these, combined with the ability to dope the silk with growth factors and other compounds could be used for the generation of complex 3D patterned cell scaffolds to form microenvironments for different cell types within the same scaffold. With maximum penetration depth of nearly 1 cm and a lateral resolution on the order of 5 μm , silk hydrogels are an excellent substrate for multiphoton micromachining. Given the limits of travel of the micropositioning stage, the total addressable volume of our workstation was greater than

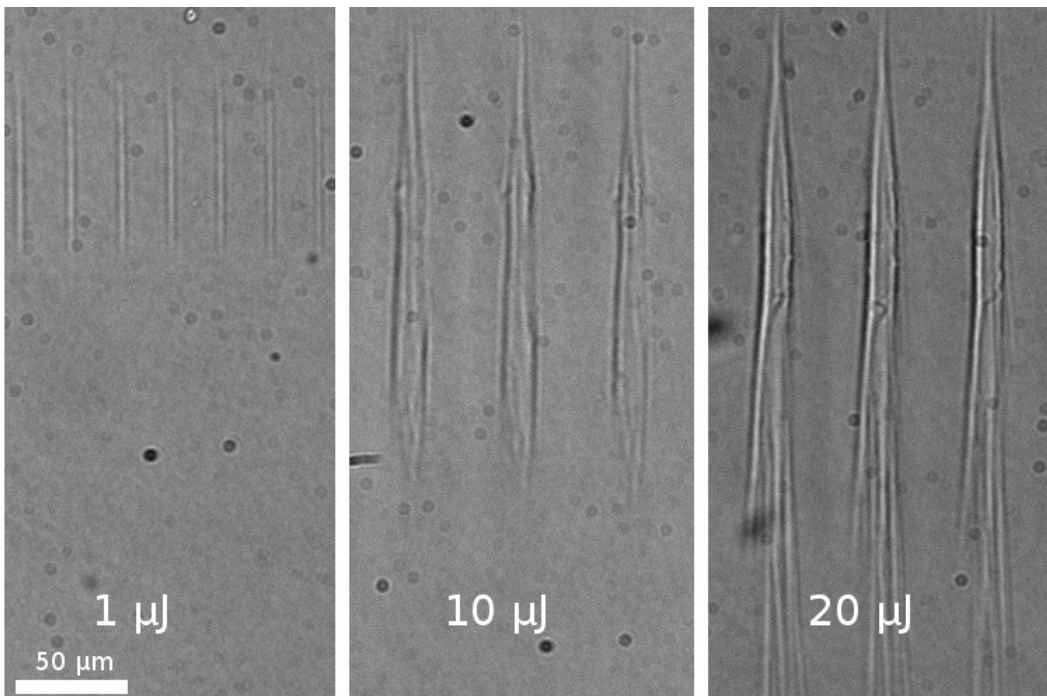


Figure 5.3: Amplified laser pulses incident from the bottom were used to create voids in the silk hydrogels at various pulse energies. Symmetrical features using $1 \mu\text{J}$ pulses (left) indicate that self-focusing is negligible. Strong self-focusing effects are evident in the asymmetrical shape from $10 \mu\text{J}$ pulses (center) and $20 \mu\text{J}$ (right) pulse energies. All features were made by a single pulse at each location

100 cm^3 . Within this volume, individual voxels as small as $125 \mu\text{m}^3$ could be removed at will with the removed material deposited along the outer edges of the machined regions.

To explore the practicality of this technique to generate complex 3D structures, test patterns were micromachined into the bulk of the silk gel. The first was a helix consisting of two turns with an outer diameter of $200 \mu\text{m}$ (Figure 5.4a). The structure started roughly $500 \mu\text{m}$ below the surface and extended $400 \mu\text{m}$ farther into the gel. The second pattern chosen was a blood vessel-like branching pattern (Figure 5.4e). This structure was situated $300 \mu\text{m}$ from the surface and had a vertical extent of $100 \mu\text{m}$. To image these patterns, the silk was stained with Rhodamine B after multiphoton micromachining

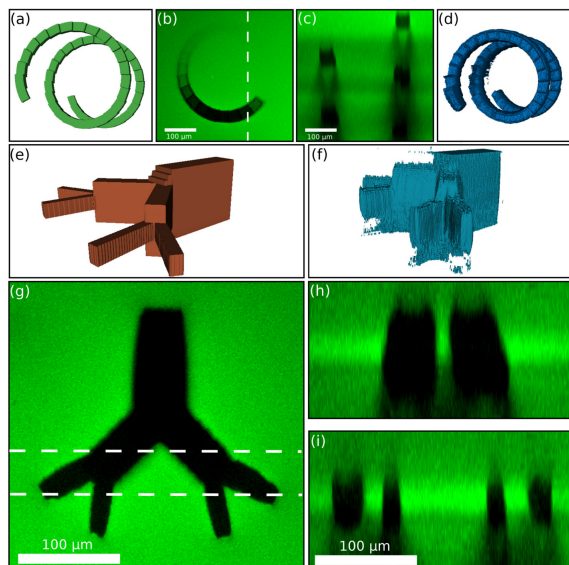


Figure 5.4: An overview of two test patterns machined into the gel. (a) 3D model of a helical pattern input into the control program. (b) Confocal microscope image of a cross section of the helix showing the machined region in black. Scale bar represents $100 \mu\text{m}$ (c) Reslice of the confocal stack along the dashed line in panel (b). Scale bar represents $100 \mu\text{m}$ (d) 3D reconstruction of the segmented confocal data showing the machined feature. (e) 3D model of a branching pattern input into the machining control program. (f) 3D reconstruction of resulting machined region made by segmenting the confocal images. (g) Confocal slice showing a cross section of the micromachined region Scale bar represents $100 \mu\text{m}$ and also applies to panels h and i. (h-i) Cross-sections of the confocal volumes at the indicated lines.

and tomographic images were collected using confocal microscopy. The Rhodamine stained silk fluoresced brightly while the machined regions were dark indicating removal of the hydrogel in these regions. In most cases, the edges of the machined features showed evidence of greater material removal than the bulk of the features. This pattern was due to the control program which paused lateral motion of the micropositioning stage at the end of each line prior to closing the shutter so the edges of the features were always exposed to more pulses than the center. Increased fluorescence was also visible around the edges of the features which was attributed to the deposition of removed material along the borders. This phenomenon was also observed when imag-

ing using the autofluorescence of silk for contrast rather than exogenous stains (Figure 5.5).

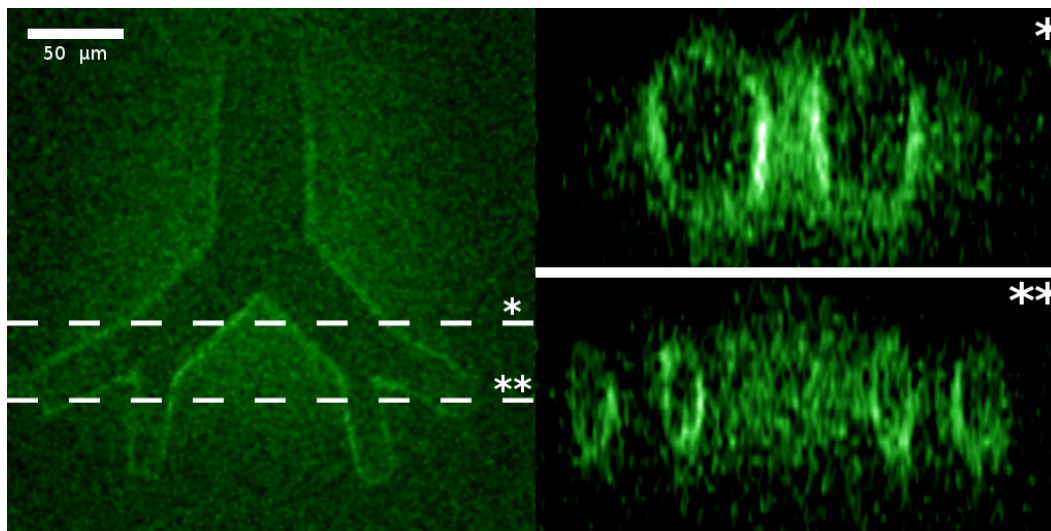


Figure 5.5: Confocal cross section (left) of the vascular like pattern described in Fig. 5.4 using only the autofluorescence of silk fibroin for contrast. An increase in autofluorescence can be appreciated immediately surrounding the machined region which suggests that an increased density of silk is present in those locations. The right two panels are re-slices of the confocal stack along the indicated lines. The scale bar applies to all panels

To be useful in biomedical applications, a material must be non-toxic and support cell growth. To ensure that the machined regions were not harmful to cells in culture, sterile gels were prepared by filtering the silk through a 0.22 μm pore filter and mixed the solution in a 35 mm diameter plastic petri dish under sterile conditions for gelation. Prior to removing the dishes from the hood the lids were covered with parafilm to maintain sterility. All machining of the gels was done within the sealed petri dishes in ambient conditions.

Parallel lines approximately 3 μm in width separated by about 20 μm were micromachined onto the top surface of a gel through the bulk. Human foreskin fibroblasts were seeded on the surface and observed using phase contrast microscopy as they attached and spread over the dish. It was observed that the cells tended to align with the grooves machined into the gel and grew

parallel with these surface features (Figure 5.6a-d). This contact guidance phenomenon is well-known and has previously been used to induce alignment of various cell types [26, 27]. Since features can be machined onto the gel through a sealed dish, we hypothesize that this could be a convenient method to reorient or disrupt already established cell cultures.

In tissue engineering, access to oxygen and nutrients within an artificial tissue is a major challenge that limits cell density within tissue engineered constructs [28]. To address this issue, researchers have generated scaffolds with interconnected porous networks [29]. However, such pores are randomly distributed, limiting the amount of control of cell growth and infiltration that is possible. Multiphoton micromachining allows fully pre-determined micron-scale features to be generated within a construct, allowing spatial control over cell infiltration. To test whether micromachined features within the silk hydrogels could be used to direct cell growth in 3-dimensions, Y shaped branching patterns were machined into the gels such that the main branch intersected the surface allowing cells and media to penetrate the bulk of the gel (Figure 5.7a). Cells were stained with a fluorescent dye and confocal images were taken of each feature at days 5, 9, and 14 post seeding. Cell density was assessed at three locations within each feature: the main branch, the transition region, and the lower branch. By day 9 and continuing to day 14, cells were observed in all three regions in 100% of the small features. The larger features were less well populated with cells found in 100% of the main branches, 86% of the transition regions, and only 14% of the lower branches by day 9. On day 14, 71% of the large features had cells in the lower branches. One of the large features did not intersect the surface of the gel and was omitted from this analysis. No subsurface cells were observed in areas that were not laser machined (Figure 5.7a).

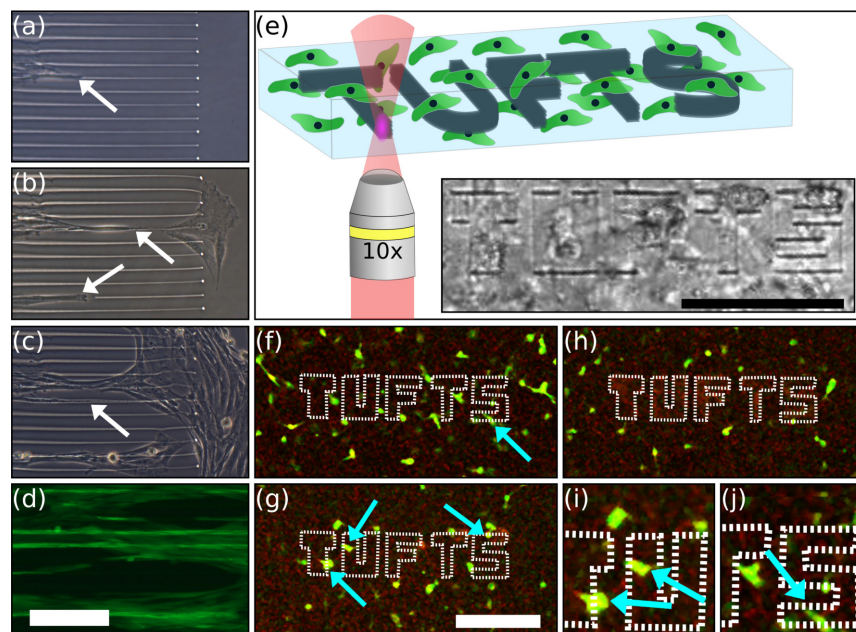


Figure 5.6: Micromachined features *in vitro*. (a-d) Machined lines on the surface of a gel at day 1, 3, 5, and 8 respectively. Arrows indicate cells growing along the machined lines. Panel (d) shows fluorescently labeled cells growing in the lines. The scale bar is $100\ \mu\text{m}$ long. Panel (d) shows a slightly different region of the gel as high cell density obscured the features at the location of the other images. (e) Cartoon showing micromachining of a gel laden with hMSCs (not to scale). Inset: Brightfield image of the machined region. Scale bar represents $250\ \mu\text{m}$. (f-h) Confocal images of the cell laden gel following live/dead staining $76\ \mu\text{m}$ below, $62\ \mu\text{m}$ above, and in the plane of machining respectively. Dashed lines outline the micromachined region. Scale bar represents $250\ \mu\text{m}$. (i-j) Close-up of living cells irradiated by the beam above (i) and below (j) the focal plane.

Rather than providing a means for cells to infiltrate a material from the surface, it is often easier to encapsulate cells within the material itself. It has been shown that human mesenchymal stem cells (hMSCs) can be encapsulated within this type of silk hydrogel [25]. When cells are encapsulated in this way the concentrations of oxygen, nutrients, and growth factors are governed by diffusion, limiting the size of such constructs. 3D patterned cell-laden hydrogels would have more surface area for the diffusion of oxygen and well-defined patterns could provide an artificial microvasculature, greatly increasing the maximum size at which cell growth could be supported. To investigate

the ability of multiphoton micromachining to pattern cell-laden hydrogels, hMSCs were embedded in the bulk of a $\sim 500 \mu\text{m}$ thick gel. The word “Tufts” was micromachined into the gel (Figure 5.6e) and, less than 4 hours after machining, cells were stained with a live/dead fluorescence assay. Following staining the dishes were examined using confocal microscopy. Dead cells were found in the plane of micromachining with living cells present both directly above and below the machined volume (Figure 5.6f-j). This was expected as cells are largely transparent to 810 nm light so they should be unaffected by the beam far from the focus. The high temperatures at the focus of the beam are likely responsible for the dead cells found in the micromachined regions.

Finally, a pilot *in vivo* study was conducted in which 3 mice were implanted with 2 machined gels each. One gel contained a branching pattern with a main branch diameter of $200 \mu\text{m}$, the second gel contained a branching pattern with a main branch diameter of $400 \mu\text{m}$. One mouse was sacrificed at 2, 3, and 4 weeks. Upon subsequent imaging the machined features were identified in 4 of the 6 samples with at least one feature identified at each time point. Cells were found to penetrate the gels via the machined features in the 2 and 3 week sample (Figure 5.7). In the 4 week sample cells were found to have overgrown the machined feature and not penetrated into the gel. It is likely that the overgrowth in the 4 week case was not due to the extra time of implantation as no cells were seen to penetrate the gel, but rather occurred relatively soon after implantation.

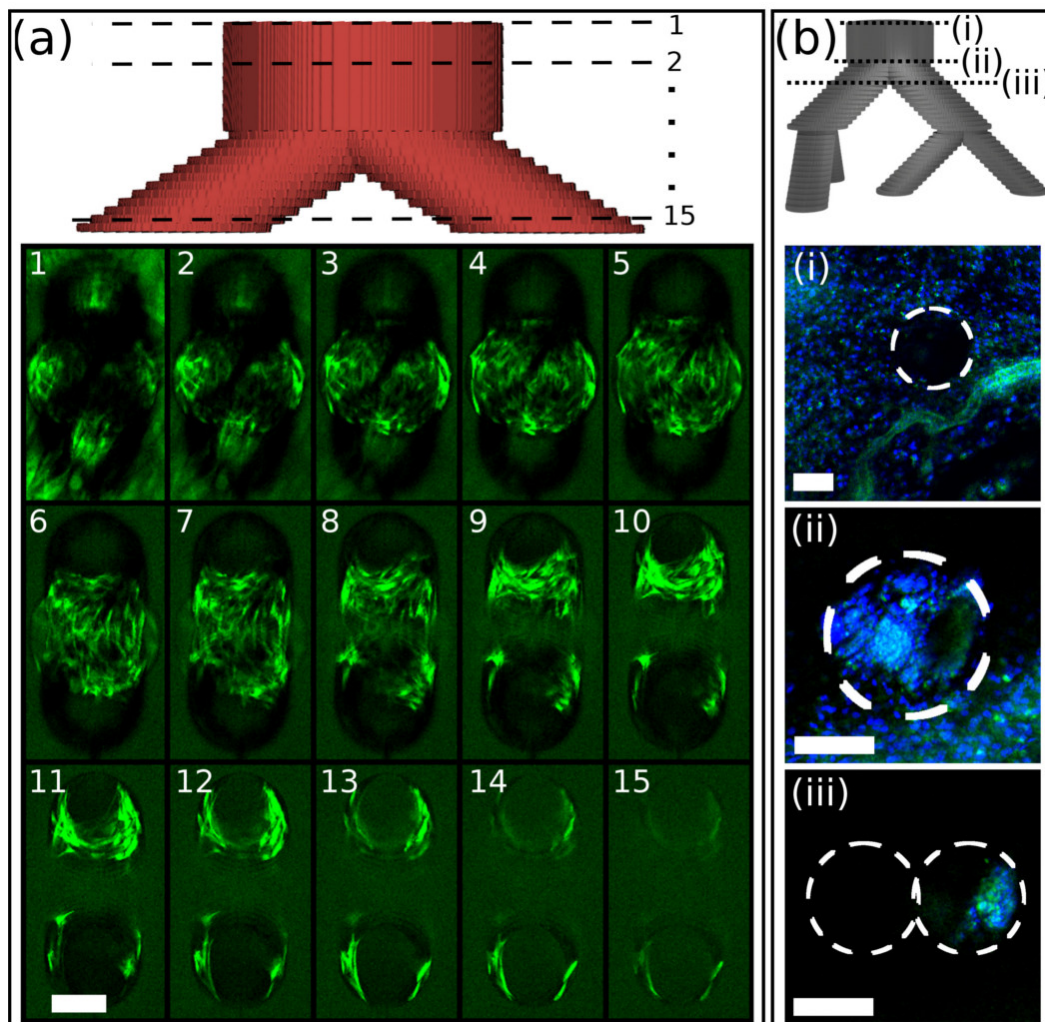


Figure 5.7: Cell infiltration into machined features. (a) Top: 3D model of the pattern machined into hydrogels that were subsequently seeded with cells *in vitro*. (a) Bottom: Series of confocal images of fibroblasts growing within a Y-shaped machined feature on day 9 after seeding. Each image is separated by 10 μm in the Z-direction. Scale bar indicates 100 μm (b) Top: 3D model of the pattern machined into a hydrogel that was subsequently implanted subcutaneously in mice. Lines marked (i-iii) indicate the confocal cross-sections shown in the panels below. The white circles in (i) and (ii) correspond to the main branch diameter and approximate location in the construct. The smaller circles in (iii) correspond to the secondary branch diameters. Cells had infiltrated to the bottom of the main branch (ii) and had begun extending down one of the secondary branches (iii). All scale bars represent 100 μm .

5.3 Discussion

These results are significant as they show that multiphoton micromachining in silk fibroin hydrogels was capable of directing cell growth and speeding infiltration into an artificial construct. Patterned biocompatible constructs are of great interest in the field of tissue engineering which seeks to artificially recapitulate natural structures in the body. One promising avenue to do so is the use of decellularization as a means to replace damaged organs [30]. This technique involves the harvest of a healthy organ and the removal of all cellular material leaving behind a structured extracellular matrix. The resulting decellularized scaffold acts as a template for new cell growth. However, this technique requires access to a healthy organ as well as time for cell culture. While this method could be used to reduce rejection of donated organs, it does little to help those who are still waiting for an organ transplants. While the micropatterning described here is too small-scale to be used to replicate an entire organ, it provides a unique combination of high resolution (micron-scale) structuring with the possibility of generating large (mm-scale) features. This combination of high resolution with large volume of modification could prove useful to link large scale 3D patterning of biological materials using techniques like 3D bio-printing[31], with techniques to produce random voids in a material on the 0.1 μm scale[29].

In conclusion, silk hydrogels were found to be an attractive substrate for photoinitiator-free multiphoton micromachining. Using only moderate laser power it was possible to generate voids within the bulk material at depths of nearly 1 cm. This approach enabled rapid formation of high-resolution structures over multiple length scales in three-dimensions and could be carried out in cell-laden hydrogels without damage to living cells in the volume immediately adjacent to the micromachined region. The features are formed in a soft,

biocompatible matrix which enables the guidance of cells in three dimensions and appears to promote infiltration of cells *in vivo* without loss of the pattern's structural integrity. All-aqueous processing of the material and machining at ambient temperatures without harsh solvents or toxic photoinitiators should make it possible to further promote cell infiltration and differentiation using growth factors or other chemical signals. While there are many options to improve the resolution and utility of the micromachining workstation, the technique described here allows for rapid prototyping of meso-scale features in a robust, simple to use, biocompatible substrate. 3D patterns that are suitable for guiding cell growth can be produced over large volumes with high resolution in a manner similar to a 3D printer, but using empty space as an ink. Such patterned gels allow control over cell growth and implantation on the 10 μm scale allowing the recapitulation of native micron-scale structures in tissue engineering scaffolds. This approach for the generation of programmable structures using multiphoton micromachining in biocompatible silk hydrogels are virtually impossible to produce using any other method, opening numerous new avenues of investigation into the 2D and 3D patterning of soft materials.

5.4 Materials & Methods

Multiphoton micromachining workstation: ~ 125 fs pulses of 810 nm light from a titanium sapphire oscillator (Tsunami, Spectra Physics) at a repetition rate of 80 MHz were passed through a computer controlled shutter and directed into the rear accessory port of an inverted microscope. The light was focused to a ~ 5 μm spot through a 0.3 NA microscope objective with a working distance of 1.03 cm onto the sample which was placed on a computer controlled XYZ translation stage (Ludl Electronics, Hawthorne, NY). Using

a custom LabView application complex patterns could be micromachined by inputting stacks of binary images into the program. Pulse energies were manually adjusted via a half-wave plate and polarizer giving continuous control of pulse energy from 0.1 to approximately 10 nJ per pulse.

Hydrogel preparation: Silk fibroin was extracted as described in Ref. [32] with a degumming time of 60 minutes. Gels were prepared by adding 10 units/mL type VI horseradish peroxidase and 10 $\mu\text{L}/\text{mL}$ 1% hydrogen peroxide [25]. To facilitate fluorescence imaging, Rhodamine B stained gels were prepared after the desired pattern had been micromachined. These gels were soaked in a solution of 0.1 mM Rhodamine B for 4 hours and then were rinsed in 10 changes of deionized water over the following 24 hours to remove any Rhodamine not bound to the silk.

Gel micromachining: Lines were micromachined on the top surface of a thin gel at pulse energies ranging from 0.25 to 5 nJ/pulse and were imaged an MFP-3D-Bio atomic force microscope (Asylum Research, Santa Barbara, CA). The samples were scanned in contact mode under phosphate buffered saline solution using TR800PSA cantilevers with a calibrated spring constant of 0.4 N/m.

Maximum depth of machining was determined by forming a silk gel inside a plastic fluorescence cuvette. 30 μm thick lines were micromachined in the silk at regular depth intervals. Translation speed varied between 100 $\mu\text{m}/\text{s}$ and 25 $\mu\text{m}/\text{s}$ depending on the depth. A side view of the lines was obtained by rotating the cuvette 90 degrees and imaging via brightfield microscopy.

2D contact guidance: Silk solutions were filtered through a 0.22 μm filter and gelled in a 35 mm petri dish. Prior to removal from the hood, dishes were sealed with parafilm to maintain sterility. Lines were then micromachined onto the top surface of the gel. Human foreskin fibroblasts were seeded onto the gel

and cultured in DMEM with 10% FBS at 37 °C, 5% CO₂. Gels were imaged via phase contrast microscopy at day 1, 3, and 5 post seeding. On day 8 the cells were stained with a Live/Dead® Viability/Cytotoxicity kit (Molecular Probes, Inc. Eugene, OR) fluorescence assay and imaged via fluorescence microscopy.

Cell-laden hydrogels: Human mesenchymal stem cells (hMSC's) were isolated from fresh bone marrow aspirate (Lonza, Basel, Switzerland) as previously described [33]. hMSC's were gently mixed into a partially gelled silk hydrogel at a rate of 1000 cells per mm³. 100 μL of the silk/cell mixture was added to each glass bottomed petri dishes [25]. After gelation, micromachining was performed on the cell-laden hydrogels. Within 4 hours of machining the cells were stained with a Live/Dead® Viability/Cytotoxicity kit (Molecular Probes, Inc. Eugene, OR) and examined via confocal fluorescence microscopy.

3D cell guidance: Sterile gels were prepared as described in “2D contact guidance”. 3D “Y” shaped branching patterns were machined into the gel with the main branch of the “Y” intersecting the top surface of the gel. Main branch diameters were 200 μm and 400 μm in the small and large features respectively. Human foreskin fibroblasts were seeded onto the surface of the gel after micromachining. Gels were examined via confocal microscopy on day 5, 9, and 14 post seeding. The day before each imaging session dishes were stained with CytoTraker™ Green (Molecular Probes, Eugene, OR).

Implantation: Sterile gels were prepared in 35 mm petri dishes as described above and a 4 mm biopsy punch was used to remove cylinders of gel. Branching patterns (Figure 5.7b) were machined into each cylinder. All procedures involving mice were approved by the Tufts University Institutional Animal Care and Use Committee. Animals were anesthetized by isoflurane inhalation during the procedure. Machined gels were implanted subcutaneously into the lumbar region of 3 mice. Silk implants and adjacent tissues were ex-

tracted following euthanasia (carbon dioxide asphyxiation) at 2, 3, and 4 weeks post-implantation. Gels were recovered from the mice and fixed in 10% formalin and stained with Phalloidin and DAPI (4',6-diamidino-2-phenylindole).

Bibliography

- [1] V. L. S. Lapointe, A. T. Fernandes, N. C. Bell, F. Stellacci, and M. M. Stevens, "Nanoscale Topography and Chemistry Affect Embryonic Stem Cell Self-Renewal and Early Differentiation," *Advanced Healthcare Materials*, vol. 2, no. 12, pp. 1644–1650, 2013.
- [2] X. Shi, S. Chen, J. Zhou, H. Yu, L. Li, and H. Wu, "Directing osteogenesis of stem cells with drug-laden, polymer-microsphere- based micropatterns generated by teflon microfluidic chips," *Advanced Functional Materials*, vol. 22, no. 18, pp. 3799–3807, 2012.
- [3] O. Jeon and E. Alsberg, "Regulation of stem cell fate in a three-dimensional micropatterned dual-crosslinked hydrogel system," *Advanced Functional Materials*, vol. 23, no. 38, pp. 4765–4775, 2013.
- [4] B. B. Mandal and S. C. Kundu, "Cell proliferation and migration in silk fibroin 3D scaffolds," *Biomaterials*, vol. 30, no. 15, pp. 2956–2965, 2009.
- [5] J. Giannatsis and V. Dedoussis, "Additive fabrication technologies applied to medicine and health care: a review," *The International Journal of Advanced Manufacturing Technology*, vol. 40, pp. 116–127, dec 2007.
- [6] F. Rengier, A. Mehndiratta, H. von Tengg-Kobligk, C. M. Zechmann, R. Unterhinninghofen, H.-U. Kauczor, and F. L. Giesel, "3D printing based on imaging data: review of medical applications," *International*

- journal of computer assisted radiology and surgery*, vol. 5, no. 4, pp. 335–341, 2010.
- [7] A. Cohen, A. Laviv, P. Berman, R. Nashef, and J. Abu-Tair, “Mandibular reconstruction using stereolithographic 3-dimensional printing modeling technology,” *Oral surgery, oral medicine, oral pathology, oral radiology, and endodontics*, vol. 108, pp. 661–6, nov 2009.
- [8] S. V. Murphy and A. Atala, “3D bioprinting of tissues and organs,” *Nature biotechnology*, vol. 32, no. 8, pp. 773–785, 2014.
- [9] S. M. Peltola, F. P. W. Melchels, D. W. Grijpma, and M. Kellomäki, “A review of rapid prototyping techniques for tissue engineering purposes,” *Annals of medicine*, vol. 40, pp. 268–80, jan 2008.
- [10] M. Goppert-Mayer, “Elementary processes with two quantum jumps,” *Annalen der Physik*, vol. 9, pp. 273–94, 1931.
- [11] Y. Liu, S. Sun, S. Singha, M. R. Cho, and R. J. Gordon, “3D femtosecond laser patterning of collagen for directed cell attachment,” *Biomaterials*, vol. 26, pp. 4597–605, aug 2005.
- [12] M. Oujja, S. Pe’rez, E. Fadeeva, J. Koch, B. N. Chichkov, and M. Castillejo, “Three dimensional microstructuring of biopolymers by femtosecond laser irradiation,” *Applied Physics Letters*, vol. 95, no. 26, p. 263703, 2009.
- [13] D. Day and M. Gu, “Microchannel fabrication in PMMA based on localized heating by nanojoule high repetition rate femtosecond pulses,” *Optics express*, vol. 13, no. 16, pp. 5939–5946, 2005.

- [14] A. M. Kloxin, A. M. Kasko, C. N. Salinas, and K. S. Anseth, “Photodegradable Hydrogels for Dynamic Tuning of Physical and Chemical Properties,” *Science*, vol. 324, pp. 59–63, apr 2009.
- [15] N. I. Smith, K. Fujita, O. Nakamura, and S. Kawata, “Three-dimensional subsurface microprocessing of collagen by ultrashort laser pulses,” *Applied Physics Letters*, vol. 78, no. 7, p. 999, 2001.
- [16] R. W. Boyd, S. G. Lukishova, and Y. R. Shen, *Self-focusing: Past and Present: Fundamentals and Prospects*, vol. 114. Springer Science & Business Media, 2008.
- [17] P. Hanczyc, M. Samoc, and B. Norden, “Multiphoton absorption in amyloid protein fibres,” *Nature Photonics*, vol. 7, pp. 969–972, nov 2013.
- [18] M. B. Applegate, B. Marelli, D. L. Kaplan, and F. G. Omenetto, “Determination of multiphoton absorption of silk fibroin using the Z-scan technique,” *Optics express*, 2013.
- [19] H. Tao, D. L. Kaplan, and F. G. Omenetto, “Silk materials - a road to sustainable high technology,” *Advanced materials*, vol. 24, pp. 2824–37, jun 2012.
- [20] F. G. Omenetto and D. L. Kaplan, “A new route for silk,” *Nature Photonics*, vol. 2, no. 11, pp. 641–643, 2008.
- [21] J. J. Amsden, P. Domachuk, A. Gopinath, R. D. White, L. D. Negro, D. L. Kaplan, and F. G. Omenetto, “Rapid nanoimprinting of silk fibroin films for biophotonic applications,” *Advanced Materials*, vol. 22, no. 15, pp. 1746–1749, 2010.

- [22] M. Brenckle, H. Tao, and S. Kim, “Protein-Protein Nanoimprinting of Silk Fibroin Films,” *Advanced Materials*, vol. 25, no. 17, pp. 2409–2414, 2013.
- [23] S. Kim, A. Mitropoulos, and J. Spitzberg, “Silk inverse opals,” *Nature Photonics*, vol. 6, no. December, pp. 2–7, 2012.
- [24] S. Lazare, a. Sionkowska, M. Zaborowicz, a. Planecka, J. Lopez, M. Dijoux, C. Louména, and M.-C. Hernandez, “Bombyx mori silk protein films microprocessing with a nanosecond ultraviolet laser and a femtosecond laser workstation: theory and experiments,” *Applied Physics A*, vol. 106, pp. 67–77, nov 2011.
- [25] B. P. Partlow, C. W. Hanna, J. Rnjak-Kovacina, J. E. Moreau, M. B. Applegate, K. A. Burke, B. Marelli, A. N. Mitropoulos, F. G. Omenetto, and D. L. Kaplan, “Highly Tunable Elastomeric Silk Biomaterials,” *Advanced Functional Materials*, pp. 4615–4624, apr 2014.
- [26] G. A. Dunn and T. Ebendal, “Contact guidance on oriented collagen gels,” *Experimental Cell Research*, vol. 111, no. 2, pp. 475–479, 1978.
- [27] N. Gomez, S. Chen, and C. E. Schmidt, “Polarization of hippocampal neurons with competitive surface stimuli: contact guidance cues are preferred over chemical ligands,” *Journal of The Royal Society Interface*, vol. 4, no. 13, pp. 223–233, 2007.
- [28] E. Sachlos and J. T. Czernuszka, “Making tissue engineering scaffolds work. Review: the application of solid freeform fabrication technology to the production of tissue engineering scaffolds.,” *European cells & materials*, vol. 5, pp. 29–39; discussion 39–40, 2003.

- [29] L. M. Bellan, S. P. Singh, P. W. Henderson, T. J. Porri, H. G. Craighead, and J. a. Spector, “Fabrication of an artificial 3-dimensional vascular network using sacrificial sugar structures,” *Soft Matter*, vol. 5, no. 7, p. 1354, 2009.
- [30] S. F. Badylak, D. Taylor, and K. Uygun, “Whole Organ Tissue Engineering: Decellularization and Recellularization of Three-Dimensional Matrix Scaffolds,” *Annual Review of Biomedical Engineering*, vol. 13, no. 1, p. 110301095218061, 2010.
- [31] S. V. Murphy and A. Atala, “3D bioprinting of tissues and organs.,” *Nature biotechnology*, vol. 32, no. 8, pp. 773–785, 2014.
- [32] D. N. Rockwood, R. C. Preda, T. Yücel, X. Wang, M. L. Lovett, and D. L. Kaplan, “Materials fabrication from Bombyx mori silk fibroin.,” *Nature protocols*, vol. 6, pp. 1612–31, oct 2011.
- [33] G. H. Altman, R. L. Horan, I. Martin, J. Farhadi, P. R. H. Stark, V. Volloch, J. C. Richmond, G. Vunjak-Novakovic, and D. L. Kaplan, “Cell differentiation by mechanical stress,” *The FASEB Journal*, vol. 16, no. 2, pp. 270–2, 2002.

Chapter 6

Biocompatible silk step-index optical waveguides

6.1 Introduction

The previous chapters of this dissertation have focused on how light can be used to change the structure of silk. In this chapter the equation is flipped and the ability of silk to change light is described. Light can be altered by materials in a variety of ways: absorption, scattering, reflection, or refraction. As previously discussed, silk is highly transparent to visible light. However, the index of refraction of silk is quite high (~ 1.5) meaning that light can be trapped within silk due to total internal reflection (TIR) so long as the film is surrounded by a material with a lower refractive index. In glass, this phenomenon has been used to produce fiber optics that are capable of transmitting light thousands of kilometers with very little loss enabling essentially instantaneous communication between people around the globe. The key components that make up an optical fiber are the high index of refraction core, the low index of refraction cladding, and the surrounding medium. When light prop-

agates through the high index core, a portion of the energy penetrates into the cladding as an evanescent wave. If the interface between the core and the cladding is smooth, no energy is lost. However, if the interface is rough or unpredictable, light from the evanescent wave can be absorbed or scatter at the interface, reducing the intensity of light in the core. In a typical optical fiber, the surrounding medium has no effect on the light. However, in special circumstances the cladding can be removed from a portion of the core to allow the evanescent field to interact with the surrounding medium. Depending on the conditions, the interaction can be tuned to sense a variety of different analytes [1] or for imaging [2].

In the biomedical field, the ability to deliver light to a small volume within the body has tremendous potential to extend the utility of light-based imaging and therapy. Such delivery is challenging due to the absorption and scattering characteristics of most biological tissue. In the visible spectrum, penetration of light is limited to only a few hundred microns. Absorption of near infrared light by chromophores is minimized around 850 nm, resulting in a maximum depth of penetration of several centimeters. However, scattering from cell nuclei and other structures causes light delivered at a point to rapidly diffuse through a large volume of tissue [3]. This diffusion makes high resolution imaging, or precise delivery of light to a small target impossible.

Optical fibers are an attractive method for delivery of light because they are small, inexpensive, and highly efficient. Although glass is biologically inert, these fibers are not well suited to biological applications. Broken fibers are sharp and can cause damage to surrounding tissue. Glass is also very stiff and this mechanical mismatch can damage surrounding soft tissue due to either fiber motion or natural body motions such as heartbeat and breathing. The mismatch in stiffness between the tissue and the fiber can result in scar

formation [4] which may limit light delivery to the desired target. Implanted glass fibers are currently used to deliver light for treatment of malignant brain tumors [5], but this technique is limited to severe cases due to the risks outlined above. To wire the body with optical waveguides, a soft light guiding material is needed.

Hydrogels of biopolymers are used as materials for scaffolds in tissue engineering. They are easily interfaced with the biological environment due to their mechanical properties; porosity, which resembles that of extra cellular matrix; and their high water content. Hydrogels capable of transmitting light *in vivo* have previously been described that are capable of using encapsulated cells for sensing and therapy [6]. The index of refraction of these gels, however, was lower than that of the surrounding tissue making the constructs incapable of guiding light around bends in tissue. This severe limitation was recently addressed by the development of a step-index optical waveguide made solely from hydrogels that are capable of guiding light around curves in tissue [7]. However, dichloromethane, a harsh organic solvent, is used in their manufacture, raising concerns about long term biocompatibility and preventing the encapsulation of cells or functional biomolecules.

The use of hydrogels as waveguides has also been investigated for sensing of various biomolecules [8, 9]. Many hydrogels are amenable to cell encapsulation which can then be used for light-mediated sensing or drug release [6, 10]. Other research into biocompatible optical waveguides have utilized a variety of other materials including cellulose [11], silicone [12], agarose [10], and even bacterial cells [13], but due to high propagation losses, these materials have not seen rapid adoption.

Silk fibroin has been under steady investigation as an attractive material for tissue engineering due to its all aqueous processing, biocompatibility, non-

immunogenicity, and ability to stabilize labile compounds such as DNA and enzymes [14]. It has also been investigated as an attractive optical material due to its near complete transparency, and ability to conform to nano-scale structures such as photonic crystals and diffraction gratings [15]. Nearly all silk processing is done in water without any harsh chemicals making it possible to dope silk devices with cells [16], growth factors [17], and laser dyes [18]. By using a material able to degrade within the body after a period of time, as is possible with silk [19], the need for a second surgery to retrieve the implanted waveguide is eliminated.

Previous efforts have realized printed silk optical waveguides on quartz which predominantly used ambient air as a cladding layer. These waveguides had low loss (~ 0.5 dB/cm) propagation but were not free-standing limiting their utility for *in vivo* applications [20].

In this chapter, an optical waveguide made entirely of silk fibroin is presented (Fig. 1A). The core of the waveguide was a long narrow strip of silk film with an index of refraction of 1.54 [20]. The silk film was surrounded by a silk hydrogel comprised of greater than 90% water resulting in a refractive index of around 1.34. The index of refraction difference was large enough to provide strong guidance and propagation of light within the core of the waveguide. The flexibility, biodegradability, and low loss of these waveguides makes them ideally suited for biomedical applications.

6.2 Methods

Silk fibroin was extracted from raw *Bombyx mori* cocoons as previously described [21]. Briefly, cocoons were cut and boiled in a 0.02 M solution of sodium carbonate to remove the gum-like sericin protein. The resulting fibroin was

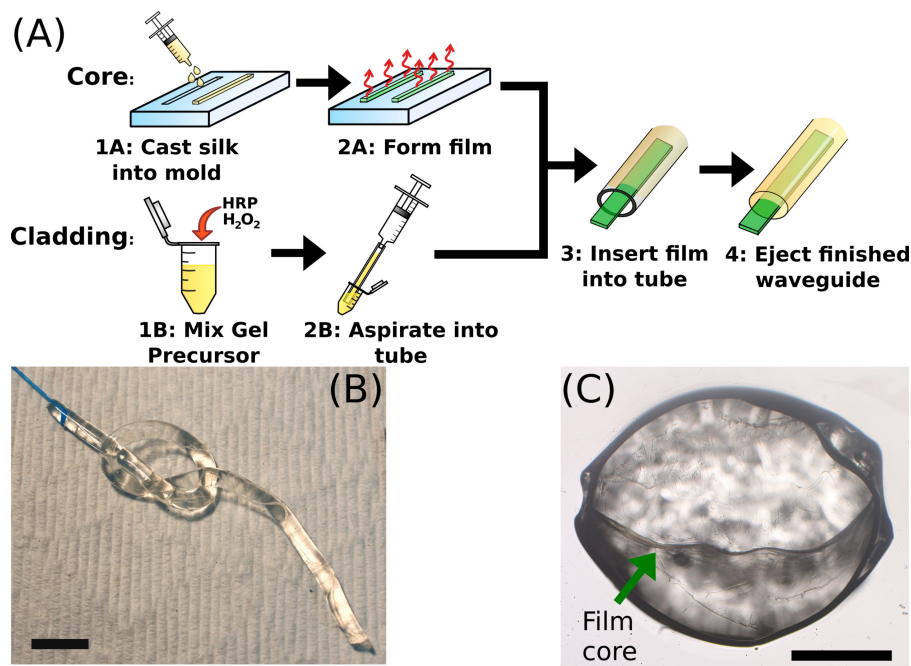


Figure 6.1: Panel A: schematic representation of the construction of silk optical waveguides. To fabricate the core, silk solution is cast into molds (1A) and allowed to dry into films (1B). For the cladding, HRP and H_2O_2 are added to a silk solution (1B) and aspirated into a PTFE tube (2B). Prior to gelation, the film is inserted into the liquid gel precursor (3). After the gel precursor solidifies, pressure on the syringe ejects the completed waveguide (4). Panel B: photograph of a 9 cm long silk waveguide coupled to a glass optical fiber knotted to show flexibility. Scale bar indicates 1 cm. Inset: Brightfield microscope image of a cross-section of a 3 mm diameter silk waveguide. Scale bar indicates 1 mm. Arrow indicates the silk film core which is 2.9 mm wide and $\sim 40 \mu\text{m}$ thick.

dissolved in 9.2 M lithium bromide and subsequently dialyzed against deionized water for 48 hours to remove the salt. Prior to use, the solution was filtered through a $0.22 \mu\text{m}$ filter to remove any dust or other impurities that would scatter light. To form the core film, $200 \mu\text{L}$ of 6.5% silk fibroin solution was cast into a poly-dimethylsiloxane (PDMS) mold measuring 2 mm wide by 14.5 cm long and left to dry in ambient conditions. To facilitate coupling into the silk waveguides, a hand-drawn glass fiber taper was inserted into the still liquid silk. The tapered geometry was formed by applying tensile stress on

a multi-mode glass fiber ($NA = 0.39$) while holding it above a butane flame to produce a taper approximately $10\ \mu\text{m}$ in diameter at the tip. After the liquid silk dried into a film, the fiber taper was fully encapsulated within the silk. Films with the encapsulated fiber were water-vapor annealed for 2 hours after drying by placing them in a vacuum chamber partially filled with water. This post treatment was necessary to render the initially water soluble films insoluble [22].

The silk film was then surrounded by a silk hydrogel to act as a cladding. The gels were formed by mixing silk fibroin solution, horseradish peroxidase ($10\ \text{U/mL}$), and $10\ \mu\text{L/mL}$ of 1% hydrogen peroxide. The subsequent reaction resulted in the formation of an elastic, optically transparent hydrogel [16]. To produce the desired cylindrical geometry, a 3.18 mm inner diameter Polytetrafluoroethylene (PTFE) tube was used as a mold. The tube was first filled with 10% Tween 20 to prevent the gels from sticking to the PTFE. The tube was cleared of Tween and then shaken vigorously to remove most of the residual surfactant from the inner walls. The silk hydrogel precursor solution was aspirated into the tube using a syringe. While the gel precursor solution was still in the liquid state the silk film core was inserted into the tube. Following gelation, gentle pressure applied to the syringe was sufficient to eject the completed waveguide from the PTFE tube (Fig. 1B). This entire procedure involves only environmentally and biologically friendly compounds and ambient temperatures making it suitable for cell growth or the inclusion of labile compounds.

The refractive index of the silk gels was measured using spectroscopic ellipsometry. 1 mm thick samples of gels ($300\ \mu\text{L}$ volume) were formed on glass slides. These gels were measured at wavelengths ranging from 400 nm to 1300 nm at 70 and 75 degree incident angles. The data were fit to Cauchy's equa-

tion to extract the refractive index of the gels. Ellipsometry data collected were found to be a good fit for the Cauchy model. The index of refraction of the gel was found to depend on the concentration of silk in the gel and ranged from 1.33 to 1.36 at 532 nm and varied roughly linearly with increasing silk concentration.

Optical losses in the silk film core were measured via the cutback technique [23]. 4 films with encapsulated optical couplers were prepared and 540 nm light was end-coupled into the glass optical fiber [23]. The silk waveguide was cut at regular intervals and the power output measured after each cut to calculate the loss per unit distance (Fig. 2).

6.3 Results

The loss along the film was found to be relatively constant except high loss was noted near the tip of the glass coupling fiber. The high initial loss is likely due to unguided modes escaping from the waveguide's core. For this reason, the first centimeter was excluded from the reported waveguide propagation loss which was calculated based on an average of all the other locations to be 2.0 ± 0.7 dB/cm (mean \pm standard deviation). This level of loss is comparable to other polymeric waveguides which range from 0.02 to 5 dB/cm [24]. Observing the films, it was noted that most of the losses occurred along the relatively rough edges of the film. Little scattering was seen on the top and bottom surface because air dried silk films are very smooth (< 5 nm rms) [15].

To test whether the silk waveguides were capable of guiding light in biological tissue, the waveguide was inserted into bovine muscle. Two incisions were made in the tissue forming a right angle. The proximal end of the silk waveguide was placed in one of the incisions and threaded around the cor-

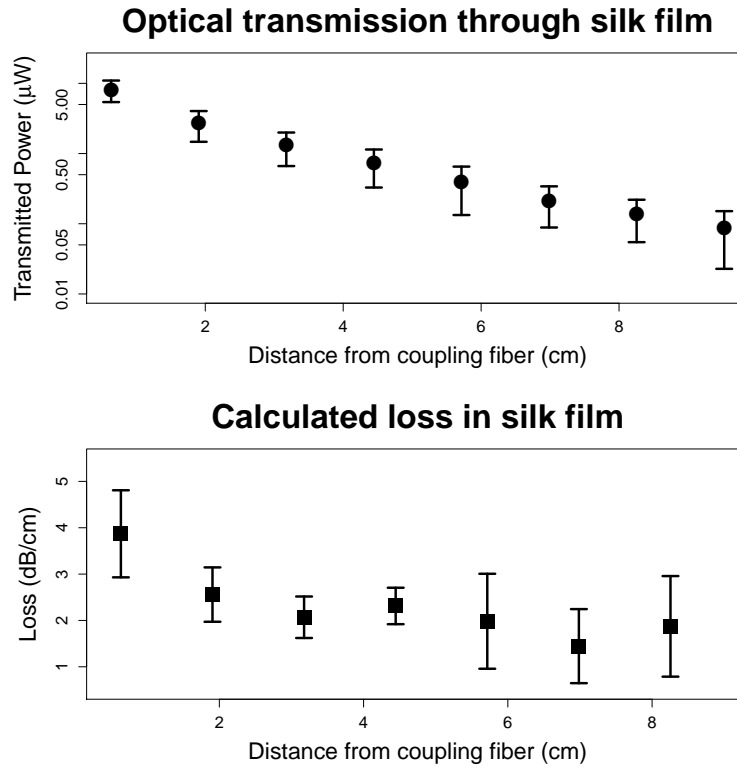


Figure 6.2: Top: Plot showing transmitted power as a function of distance from the coupling fiber. Y-axis is presented on a log scale so the straight line of the data indicates an exponential decline in transmitted power with a consistent decay constant. Error bars indicate 1 standard deviation, $n=4$. Bottom: Calculated loss per centimeter as a function of distance from the tip of the coupling fiber. High loss near the tip of the coupling fiber is likely due to unguided modes. Error bars indicate 1 standard deviation, $n=4$.

ner. The incisions were held closed using 23 gauge needles and care was taken to ensure that the tissue contacted the cladding of the waveguide to eliminate guidance due to the index difference between the cladding and air. The incisions were flooded with phosphate buffered saline to make sure that no cladding modes would be guided. Prior to the bend, light could be observed in both the cladding and the core. After the bend light could only be seen in the silk film core (Fig. 3).

The approximate light carrying capacity of these waveguides was estimated by transversely exposing the silk films to various intensities of green light for

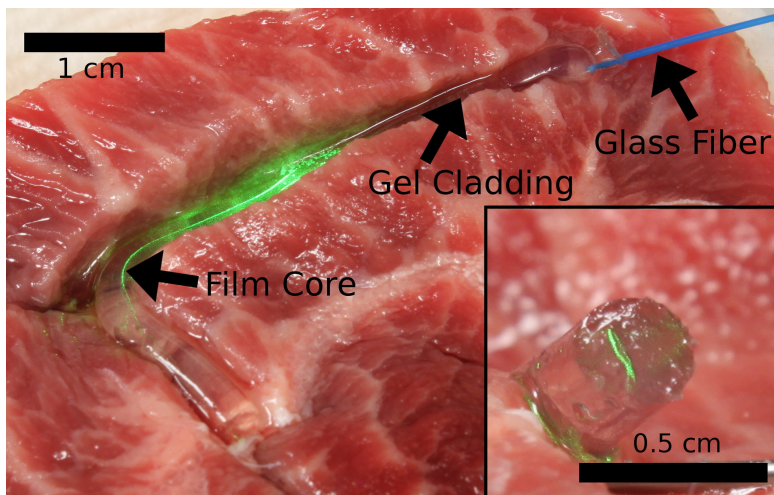


Figure 6.3: Silk waveguide guiding light in tissue. Light coupled from multi-mode glass fiber is confined within the silk film core of a 3.5 cm long waveguide. Inset shows the core of the waveguide glowing green after closure of the incisions.

10 s. Following exposure, the films were examined under brightfield microscopy for signs of damage. No damage was noted up to intensities of ~ 10 W/cm². Above 11 W/cm², significant thermal damage was observed. These intensities far exceed the damage threshold for tissue, indicating that photodamage to the fiber would not be a limiting factor in biomedical applications.

6.4 Discussion

In this work a silk film encapsulated in a silk hydrogel was shown to act as an effective waveguide in tissue. These waveguides are relatively easy to produce, robust, and able to survive handling and placement within tissue. Utilizing a glass fiber taper to couple light into the silk waveguide provides a convenient interface between the biocompatible waveguides and conventional optical systems. Loss in the waveguide core was measured to be 2.0 dB/cm which is significantly higher than losses reported previously in silk [20]. In-

creased losses are likely due to surface scattering by the rough edges of the film. When observing the waveguide, nearly all of the lost light was seen from the edges. This implies that the loss could be significantly reduced by smoothing the edges or by using a cylindrical core geometry.

Silk is both biocompatible and biodegradable, so once implanted waveguides could be left within the body. Based on data from other types of silk gels it is estimated that the cladding of these waveguides would be fully infiltrated by cells and blood vessels after approximately 12 weeks [25]. Once the cladding was infiltrated, the core of the film could last up to an additional year [19]. There would likely be no disruption of wave guiding properties until the cells reached the interface between the silk film core and the silk gel cladding. When this occurs there would be an increase in scattering losses. These losses may, in fact, be useful as they could be monitored over time to estimate the degree of cellular infiltration into the waveguide.

Biocompatible waveguides capable of delivering light to a point deep within the body have many applications. One such is photodynamic therapy (PDT) which is currently used to treat tumors using photoactivated chemotherapeutics. PDT illumination is typically provided transdermally, however, during tumor debulking surgery, it is frequently applied directly to the site of the tumor [26]. In this case, a silk waveguide could be left behind to deliver multiple PDT treatments over time to reduce the likelihood of recurrence. This type of staggered therapy has been shown to be more effective than a single dose of light because PDT drugs rapidly deplete the oxygen in the tissue during the production of free radicals [27]. Delivering multiple light doses over time, allows the oxygen concentration to recover, and the drugs to work more effectively. After the conclusion of therapy, the silk waveguide would degrade eliminating the need for a second surgery to retrieve it. The waveguides de-

scribed in this chapter are both environmentally and biologically friendly using only mild chemicals and producing no toxic byproducts. The ability to bring visible light to a small area deep within the body opens up new avenues of investigation in imaging and therapy.

Bibliography

- [1] R. Harris and J. Wilkinson, “Waveguide surface plasmon resonance sensors,” *Sensors and Actuators B: Chemical*, vol. 29, no. 1-3, pp. 261–267, 1995.
- [2] D. Axelrod, “Total internal reflection fluorescence microscopy in cell biology,” *Traffic*, vol. 2, no. 11, pp. 764–774, 2001.
- [3] S. L. Jacques, “Optical Properties of Biological Tissues: A Review,” *Physics in Medicine and Biology*, vol. 58, pp. R37–61, 2013.
- [4] L. W. Tien, F. Wu, M. D. Tang-Schomer, E. Yoon, F. G. Omenetto, and D. L. Kaplan, “Silk as a multifunctional biomaterial substrate for reduced glial scarring around brain-penetrating electrodes,” *Advanced Functional Materials*, vol. 23, pp. 3185–3193, 2013.
- [5] D. Bechet, S. R. Mordon, F. Guillemain, and M. a. Barberi-Heyob, “Photodynamic therapy of malignant brain tumours: A complementary approach to conventional therapies,” *Cancer Treatment Reviews*, vol. 40, no. 2, pp. 229–241, 2014.
- [6] M. Choi, J. W. Choi, S. Kim, S. Nizamoglu, S. K. Hahn, and S. H. Yun, “Light-guiding hydrogels for cell-based sensing and optogenetic synthesis in vivo,” *Nature Photonics*, vol. 7, pp. 987–994, oct 2013.

- [7] M. Choi, M. Humar, S. Kim, and S.-H. Yun, “Step-Index Optical Fiber Made of Biocompatible Hydrogels,” *Advanced Materials*, vol. 27, no. 27, pp. 4081–4086, 2015.
- [8] T. Forster, C. Strohhofer, and K. Bock, “Biosensor for calcium based on a hydrogel optical waveguide with integrated sensor proteins,” *Solid-State Sensors, . . .*, pp. 1218–1221, 2009.
- [9] Y. Wang, C.-J. Huang, U. Jonas, T. Wei, J. Dostalek, and W. Knoll, “Biosensor based on hydrogel optical waveguide spectroscopy,” *Biosensors & bioelectronics*, vol. 25, pp. 1663–8, mar 2010.
- [10] A. Jain, A. H. J. Yang, and D. Erickson, “Gel-based optical waveguides with live cell encapsulation and integrated microfluidics.,” *Optics letters*, vol. 37, pp. 1472–4, may 2012.
- [11] A. Dupuis, N. Guo, Y. Gao, N. Godbout, S. Lacroix, C. Dubois, and M. Skorobogatiy, “Prospective for biodegradable microstructured optical fibers.,” *Optics letters*, vol. 32, pp. 109–11, jan 2007.
- [12] L. Ding, R. I. Blackwell, J. F. Künzler, and W. H. Knox, “Femtosecond laser micromachining of waveguides in silicone-based hydrogel polymers.,” *Applied optics*, vol. 47, pp. 3100–8, jun 2008.
- [13] H. Xin, Y. Li, X. Liu, and B. Li, “Escherichia coli-Based Biophotonic Waveguides.,” *Nano letters*, no. JUNE, 2013.
- [14] H. Tao, D. L. Kaplan, and F. G. Omenetto, “Silk materials - a road to sustainable high technology,” *Advanced materials*, vol. 24, pp. 2824–37, jun 2012.

- [15] F. G. Omenetto and D. L. Kaplan, “A new route for silk,” *Nature Photonics*, vol. 2, no. 11, pp. 641–643, 2008.
- [16] B. P. Partlow, C. W. Hanna, J. Rnjak-Kovacina, J. E. Moreau, M. B. Applegate, K. A. Burke, B. Marelli, A. N. Mitropoulos, F. G. Omenetto, and D. L. Kaplan, “Highly Tunable Elastomeric Silk Biomaterials,” *Advanced Functional Materials*, pp. 4615–4624, apr 2014.
- [17] V. Karageorgiou, L. Meinel, S. Hofmann, A. Malhotra, V. Volloch, and D. Kaplan, “Bone morphogenetic protein-2 decorated silk fibroin films induce osteogenic differentiation of human bone marrow stromal cells,” *Journal of Biomedical Materials Research - Part A*, vol. 71, no. 3, pp. 528–537, 2004.
- [18] S. Toffanin, S. Kim, S. Cavallini, M. Natali, V. Benfenati, J. J. Amsden, D. L. Kaplan, R. Zamboni, M. Muccini, and F. G. Omenetto, “Low-threshold blue lasing from silk fibroin thin films,” *Applied Physics Letters*, vol. 101, no. 9, p. 091110, 2012.
- [19] Y. Wang, D. Rudym, A. Walsh, and L. Abrahamsen, “In vivo degradation of three-dimensional silk fibroin scaffolds,” *Biomaterials*, vol. 29, pp. 3415–3428, 2008.
- [20] S. T. Parker, P. Domachuk, J. Amsden, J. Bressner, J. a. Lewis, D. L. Kaplan, and F. G. Omenetto, “Biocompatible Silk Printed Optical Waveguides,” *Advanced Materials*, vol. 21, pp. 2411–2415, jun 2009.
- [21] D. N. Rockwood, R. C. Preda, T. Yücel, X. Wang, M. L. Lovett, and D. L. Kaplan, “Materials fabrication from Bombyx mori silk fibroin,” *Nature protocols*, vol. 6, pp. 1612–31, oct 2011.

- [22] X. Hu, K. Shmelev, L. Sun, E. S. Gil, S. H. Park, P. Cebe, and D. L. Kaplan, “Regulation of silk material structure by temperature-controlled water vapor annealing,” *Biomacromolecules*, vol. 12, pp. 1686–1696, 2011.
- [23] L. Chen, J. Cameron, and X. Bao, “Characterization of Optical Fibers,” in *Handbook of Computer Networks*, pp. 815–827, John Wiley & Sons, 2007.
- [24] B. H. Ma, A. K. Jen, and L. R. Dalton, “Polymer-Based Optical Waveguides : Materials , Processing , and Devices,” *Advanced Materials*, vol. 14, no. 19, pp. 1339–1365, 2002.
- [25] O. Etienne, A. Schneider, J. a. Kluge, C. Bellemin-Laponnaz, C. Polidori, G. G. Leisk, D. L. Kaplan, J. a. Garlick, and C. Egles, “Soft Tissue Augmentation Using Silk Gels: An In Vitro and In Vivo Study,” *Journal of Periodontology*, vol. 80, no. 11, pp. 1852–1858, 2009.
- [26] W. F. Sindelar, T. F. DeLaney, Z. Tochner, G. F. Thomas, L. J. Dachoswki, P. D. Smith, W. S. Friauf, J. W. Cole, and E. Glatstein, “Technique of photodynamic therapy for disseminated intraperitoneal malignant neoplasms. Phase I study,” *Archives of surgery*, vol. 126, no. 3, pp. 318–324, 1991.
- [27] M. H. Roozeboom, M. A. Aardoom, P. J. Nelemans, M. R. T. M. Thissen, N. W. J. Kelleners-Smeets, D. I. M. Kuijpers, and K. Mosterd, “Fractionated 5-aminolevulinic acid photodynamic therapy after partial debulking versus surgical excision for nodular basal cell carcinoma: a randomized controlled trial with at least 5-year follow-up,” *Journal of the American Academy of Dermatology*, vol. 69, no. 2, pp. 280–287, 2013.

Chapter 7

Silk photocrosslinking using riboflavin

7.1 Introduction

In the previous chapter, the use of silk to modify light via total internal reflection was described. Earlier chapters showed the use of ultrashort pulses of light to modify silk. Here, the focus returns to the theme of using light to change silk, but rather than using expensive femtosecond lasers to produce voids, cheap LEDs are used in conjunction with a biocompatible photoinitiator (riboflavin) to form solid gels from liquid silk solutions. The use of photopolymerization to create high resolution patterns has been critical for technological advancement in the electronics industry. In the manufacture of computer chips photopolymerizable materials (photoresists) are used to pattern silicon wafers. The steady advance of computing power is due largely to the refinement of photolithographic techniques which now allow resolutions below 20 nm [1]. The biomedical field has also benefited from photopolymerizable materials and improvements in photolithography. Photopolymerization

allows for spatial control of material properties which has been applied to alter cellular microenvironments yielding significant advances in our understanding of cell signaling, behavior, and differentiation [2, 3]. Photopatterning has also been used to direct cell attachment and migration via the selective exposure of cell binding moieties [4], as well as create stiffness gradients in a material to investigate cellular response to mechanical cues [5].

On the macro scale, photocrosslinking has found application in the medical field. Photochemical tissue bonding offers a method of wound closure that uses the photosensitizer rose bengal (4,5,6,7-tetrachloro-2',4',5',7'-tetraiodofluorescein) and green light to chemically crosslink tissues. This technique allows for rapid closure of wounds without the use of sutures which results in faster healing with reduced scar formation [6], and is able to create a fluid-tight seal for microvascular anastomoses [7]. A similar technique has been used to treat atherosclerosis by altering the mechanical properties of explanted vein tissue to more closely mimic that of the coronary artery. These "artery-like" veins have shown exceptional potential for use in coronary artery autografts [8]. Treatment of eye injuries is a particularly attractive application for phototissue bonding because of the delicacy of corneal operations such as suturing. These invasive procedures may lead to increased inflammation and corneal scarring [9] reducing the transparency of the cornea and leading to disrupted vision. Amnion patches photo-bonded to the cornea with rose bengal significantly increase ocular burst pressure in rabbits with full-thickness corneal wounds [10]. Photoactivated adhesives and patches made from biodendrimers [9] and hyaluronic acid [11] respectively have also shown promise in the suture-free treatment of corneal wounds.

Crisp vision depends on the ability of the cornea to focus light onto the retinal surface. Near-sightedness (myopia) and far-sightedness (hyperopia) can be

corrected by altering the corneal curvature by using photorefractive keratectomy (PRK) to selectively remove portions of the cornea. For PRK procedures to be performed safely, sufficient corneal thickness must remain after the procedure to provide mechanical strength to the eye. This limitation makes PRK unsuitable for patients with thin corneas due to genetics or corneal ectatic disorders. Keratoconus is one such ectatic disorder in which corneal thinning leads to the cornea assuming a cone shape, rather than its usual domed appearance. Though fairly rare in the US [12], keratoconus is found in over 2% of the population in rural India [13]. The effects of this disease include loss of visual acuity, and permanent eye damage, often requiring extensive surgery to treat [14]. Recently, a technique was developed to slow the thinning of the cornea in patients with keratoconus by crosslinking corneal collagen using riboflavin and exposure to ultraviolet light. The crosslinking process results in a stiffer cornea which slows the progression of the disease, but only marginally improves vision [15]. Contact lenses can help correct vision problems in some patients, but for those who are intolerant of contacts few options remain.

Silk fibroin is a biopolymer that has been under steady investigation for decades due to its numerous favorable characteristics: biocompatibility, cytocompatibility, mechanical strength, ability to stabilize labile compounds, and biodegradability [16]. Silk is also a promising optical material due to its near perfect transparency to visible light and has been used to make a wide variety of optical elements including lenses, phase masks, diffraction gratings, and waveguides [17, 18]. This combination of properties makes silk an attractive material for use in ocular prostheses. Previous work has used ruthenium to photocrosslink silk [19], however, under certain conditions, ruthenium can be highly toxic and is being investigated as a potential chemotherapeutic for cancer [20].

Riboflavin is an attractive photoinitiator for biomedical applications both because it is found naturally in tissues, and because it is able to crosslink via exposure to harmless visible light rather than potentially damaging ultraviolet radiation. Riboflavin photocrosslinking appears to be quite nonspecific and has been shown to photocrosslink many materials including collagen [21, 22], alginate [23], and poly(ethylene glycol) [24]. In this chapter the use of flavin-mononucleotide (FMN), a water soluble variant of riboflavin, as a photoinitiator to catalyze the transition of a liquid silk solution to a highly elastic hydrogel in the presence of light is presented. First, a theory of the mechanism of silk-riboflavin photocrosslinking is proposed. Next, the ability of this system to generate high resolution patterns of silk using photolithography is presented. Finally, a pilot study in enucleated porcine eyes is described in which silk hydrogels are adhered to deepithelialized cornea. We believe that by combining high-resolution patterning with corneal adhesion it would be possible to alter the optical thickness of the cornea with high spatial resolution to improve visual acuity in people suffering from myopia, hyperopia, and corneal ectatic disorders such as keratoconus, without the risks associated with laser vision correction surgeries [25].

7.2 Results

These results represent the first time that riboflavin has been used to photocrosslink silk fibroin. Several preliminary studies were undertaken to ensure that both light and riboflavin were necessary to initiate crosslinking and to determine the concentration of riboflavin that led to the most efficient crosslinking. The speed of crosslinking was tested by measuring the elastic and storage moduli during gelation using a rheometer (Figure 7.1). This setup allowed con-

tinuous monitoring of the gel's stiffness over time. These experiments showed that a solution containing 2 mM of riboflavin yielded the fastest crosslinking.

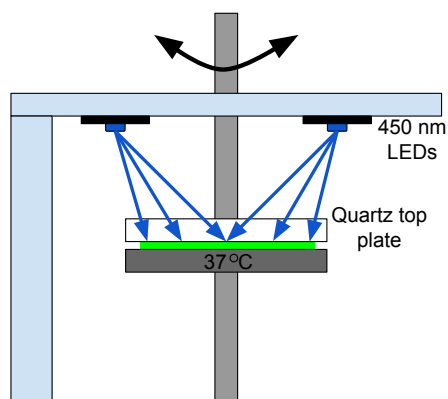


Figure 7.1: Cartoon depicting experimental set-up for monitoring evolution of gel stiffness. 3, 450 nm LEDs were equally spaced around the rheometer shaft and illuminated the sample with an intensity of 18.7 mW/cm^2 . Green region indicates the fluorescent silk solution during crosslinking.

The removal of illumination during testing immediately halted gel formation (Figure 7.2) implying that the stiffness of these gels can be precisely controlled using only light exposure. Similarly, light alone (without riboflavin) did not result in any sign of gel formation.

Mechanism: Previous work on the mechanism of photocrosslinking collagen using riboflavin is conflicted. Some groups explain the effect as solely due to singlet oxygen production [26], while others credit the production of tyrosyl radicals which can form dityrosine crosslinks [27]. Both potential mechanisms were investigated in silk by dissolving lyophilized silk protein in heavy water (D_2O), a radical oxygen promoter; sodium azide (NaN_3), a radical oxygen scavenger; and superoxide dismutase (SOD), an enzyme that catalyzes the dismutation of superoxide anion radicals to oxygen or hydrogen peroxide. Gel formation was monitored using a rheometer as described above.

Based on this experiment it is evident that the mechanism for photo crosslinking of silk fibroin is not due solely to the presence of singlet oxygen.

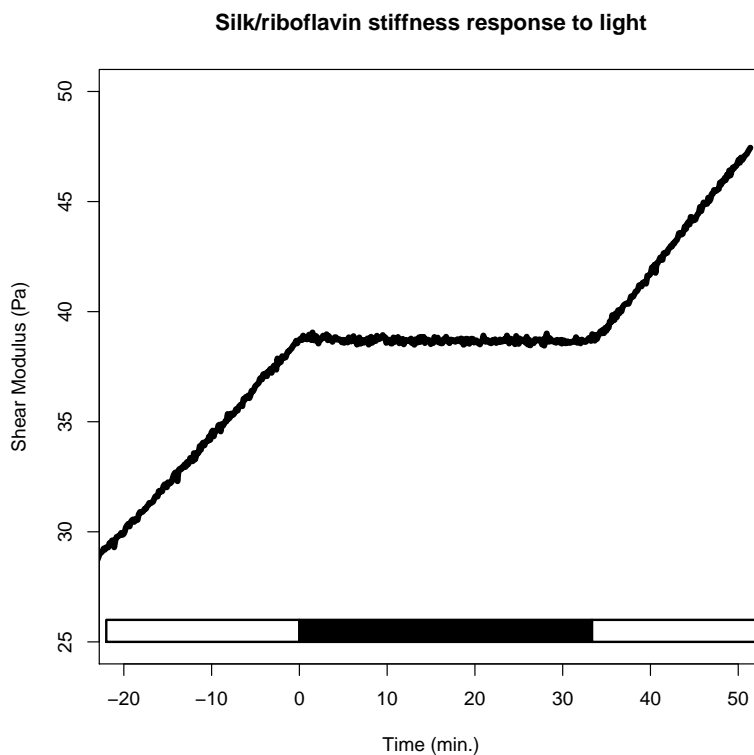


Figure 7.2: Plot showing the evolution of stiffness during illumination (white bars) and with the light off (black bar). The gel stops stiffening when light is removed.

Since singlet oxygen has a longer lifetime in D_2O , there would have been faster stiffening when silk was dissolved in D_2O . However, there was no significant difference between the D_2O group and the control (Figure 7.3). Similarly, the addition of sodium azide which efficiently scavenges singlet oxygen should have sharply reduced the stiffness following illumination. Instead, only a modest decrease in stiffness in the presence of sodium azide was found. These results imply that singlet oxygen does play a small role in silk fibroin cross-linking, but it is not the primary mechanism. Conversely, the addition of superoxide dismutase resulted in a more than six-fold increase in stiffness suggesting that the superoxide anion radical plays a strongly inhibitory role in this process.

A mechanism explaining riboflavin photocrosslinking in collagen was sug-

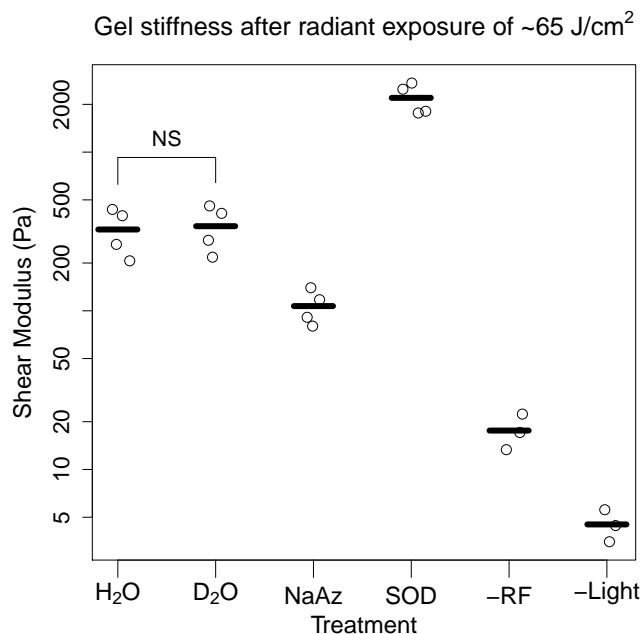
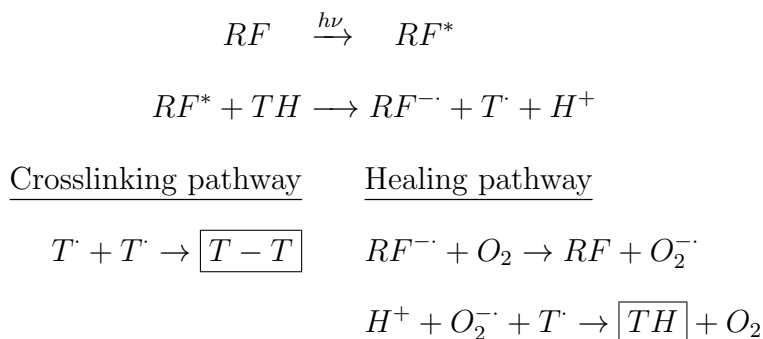


Figure 7.3: Effect of different compounds on gelation rate after illumination for 1 hour. Shear modulus values are recorded for silk dissolved in deionized water (H_2O), deuterated water (D_2O), sodium azide (NaAz), and superoxide dismutase (SOD). Negative controls $-\text{RF}$ and $-\text{Light}$ were tested without riboflavin and without illumination respectively. Shear modulus is presented on a log scale. NS indicates a non-significant difference. All other pairs of values were significant with $p < 0.001$. $N=4$ for treatment groups and $N=3$ for control groups. All data are plotted as points with bars representing the mean of each group.

gested by Kato *et al.* whose findings mirror our own [27]. Their hypothesis is that photoexcited riboflavin (RF^*) strips protons from tyrosine residues (T) in collagen forming tyrosyl radicals (T^-). Two tyrosyls are then able to form a single dityrosine complex (T-T) chemically crosslinking collagen protein backbones. Superoxide anion radicals (O_2^-) are an intermediate species in this reaction and have been shown to heal radical tyrosine which would prevent the formation of dityrosine bonds [28]. Other researchers have noted dityrosine as a photoproduct of illuminating riboflavin *in vivo* [29].



To confirm the presence of dityrosine in silk/riboflavin gels their fluorescence spectra were examined (Figure 7.4). Under excitation with 310 nm light, dityrosine fluoresces strongly around 400 nm [30]. Riboflavin has a broad absorption peak from 350 to 450 nm which might obscure the dityrosine fluorescence, so gels were rinsed with water to remove the riboflavin following gel formation. There was evidence of a clear dityrosine fluorescence peak in the rinsed gels that was not present in silk alone. The un-rinsed gels show both a small dityrosine peak as well as a small peak at 532 nm which is indicative of riboflavin fluorescence. In the un-rinsed samples the dityrosine fluorescence at 410 nm is absorbed by the riboflavin in the gel resulting in the detection of both weak dityrosine and riboflavin fluorescence.

The observed mechanical properties of riboflavin photocrosslinked gels also support the proposed mechanism. Silk/riboflavin gels have a large shear modulus coupled with a negligible storage modulus. Enzymatically crosslinked silk fibroin hydrogels form dityrosine bonds through the action of horseradish peroxidase show similar elastic properties [31].

Photolithography: Since both riboflavin and light are required for hydrogel formation it would likely be possible to generate high resolution patterns of

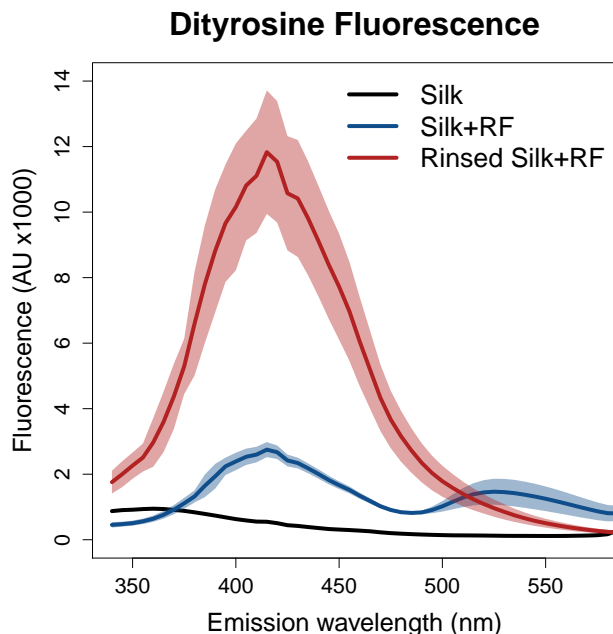


Figure 7.4: Fluorescence spectra of 3 solutions after 60 minutes of illumination by 450 nm light. Silk alone (black) shows no fluorescence, un-rinsed silk gels have a small dityrosine peak at 410 nm and a small riboflavin peak at 530 nm, rinsed silk gels have a strong dityrosine peak and no evidence of riboflavin fluorescence. Dark lines indicate the means of 8 samples with the standard deviations at each wavelength indicated by the shaded regions.

silk gel using photolithography. To do so, a photomask of a U.S. Air Force resolution test pattern printed on mylar with a guaranteed resolution of 20 μm was used. Illumination using 450 nm LEDs was provided from above through the mask. After illumination the pattern could be clearly seen in the gel due to photobleaching of the riboflavin. The sample was placed in deionized water and gently agitated for 5 minutes to remove any unpolymerized silk. There was clear pattern transfer after washing and, following drying in ambient conditions, the polymerized silk was tightly bound to the substrate (Figure 7.5). Using this rudimentary system the achievable resolution was $\sim 20 \mu\text{m}$ which is the same as the resolution of the photomask. It is likely that the resolution of these patterns could be significantly improved using a higher resolution mask and a more sophisticated apparatus.

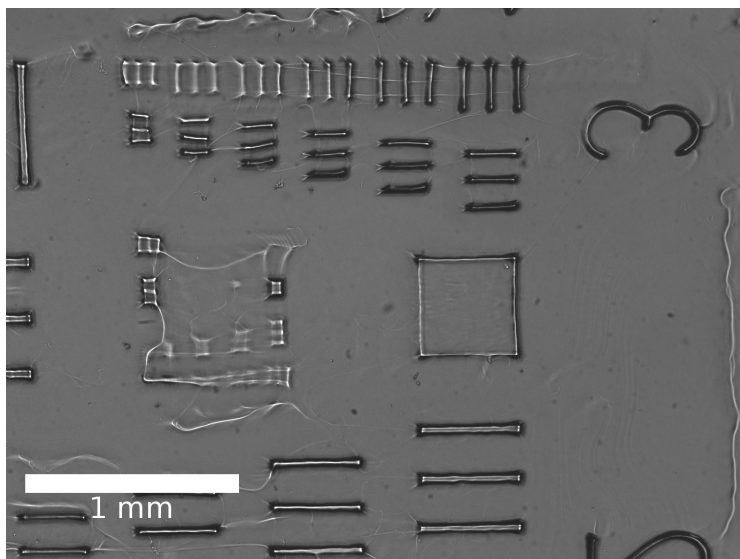


Figure 7.5: Brightfield microscope image of a high-resolution pattern of silk gel produced by photolithography. Blue light was passed through a photomask and used to illuminate a mixture of silk and riboflavin. Using this setup, silk could be patterned with a resolution of $\sim 20 \mu\text{m}$.

Silk/cornea adhesion: To test whether photocrosslinked silk hydrogels could be adhered to corneal collagen an attempt was made to bond silk films impregnated with FMN and SOD to enucleated porcine eyes (Figure 7.6). Films were cut into 1 cm disks and applied to eyes with the corneal epithelium removed.

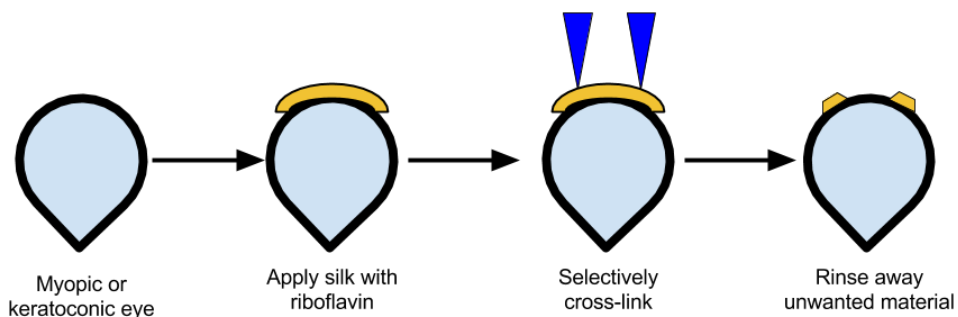


Figure 7.6: Schematic representation of riboflavin adherence for vision correction. Silk films doped with riboflavin are applied to a diseased eye. Following illumination, silk is selectively adhered to the eye surface. The unexposed silk can be rinsed away leaving behind an eye altered to correct vision.

The thickness of the silk on the eye was measured by optical coherence

tomography (OCT) immediately after application to the eye, following light exposure, and after a vigorous rinse in phosphate buffered saline (PBS) (Figure 7.7). Both the riboflavin impregnated films as well as the control films without riboflavin were found to adhere to the eyes initially (Figure 7.8) because silk films are very sticky as they begin to dissolve. However, silk films without riboflavin quickly degrade under additional wetting leaving the cornea largely bare. Conversely, the riboflavin films imaged post illumination showed little indication of wear and remained adhered to the surface of the eye even after a vigorous rinse with PBS. Control samples containing riboflavin but not exposed to light were easily removed from the eye by rinsing with PBS. Histologic inspection of the eyes revealed that the silk gel was smoothly attached to the corneal collagen without any evidence of separation (Figure 7.9).

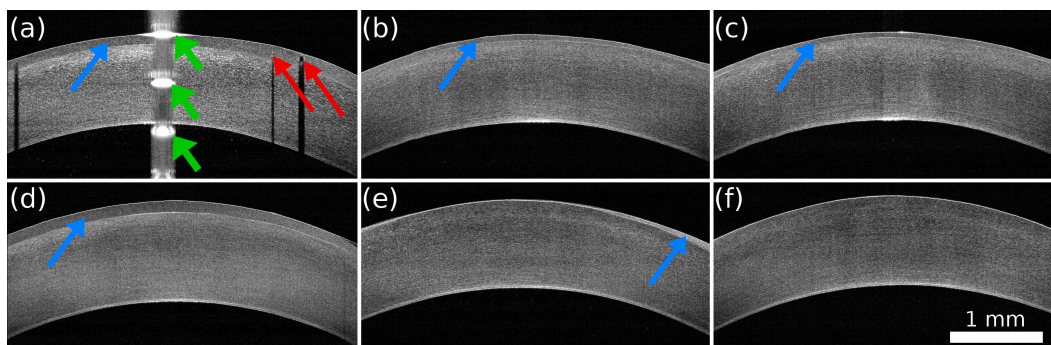


Figure 7.7: Representative OCT images of silk films applied to deepithelialized enucleated porcine eyes. Top row: Riboflavin impregnated silk. Blue arrows indicate the layer of silk overlying the corneal collagen. Red arrows on right side indicate air bubbles in the silk prior to illumination causing shadowing. Short green arrows indicate specular reflection artifacts in the OCT image. Bottom row: Images of control film without riboflavin.

7.3 Discussion

In this chapter a novel method of forming silk fibroin hydrogels was presented in which excited riboflavin radicalizes tyrosine residues in the silk protein back-

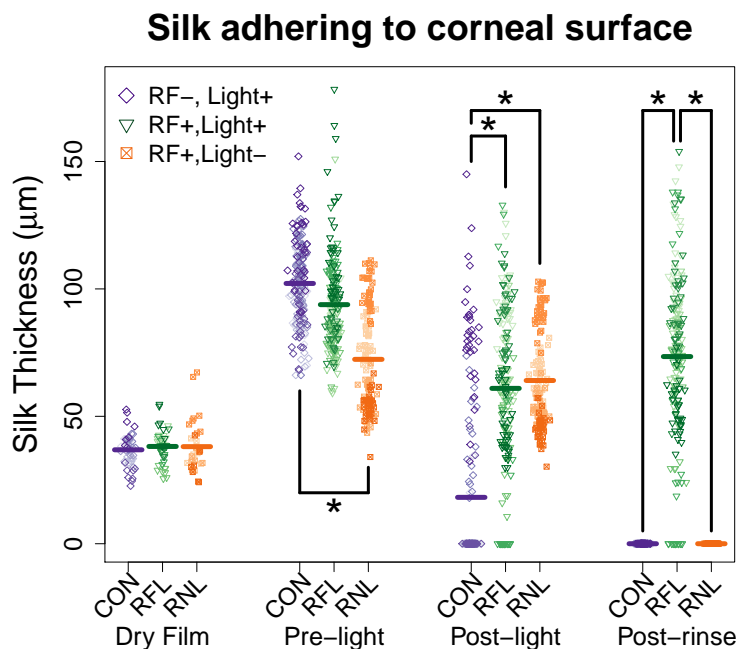


Figure 7.8: Silk thickness measured in 32 locations on each eye prior to application to the eye, immediately after application to the eye, following light exposure, and following a rinse with PBS. Films without riboflavin (CON) and films not exposed to light (RNL) show no ability to withstand rinsing. Riboflavin impregnated silk films exposed to light (RFL) are able to adhere to the corneal surface. All measurements are displayed. Data from individual eyes is indicated by a different shade. Heavy bars indicate the mean of all the data in that group. Stars indicate statistical significance between groups ($p < 0.05$). $n=6$ for CON and RFL, $n=4$ for RNL.

bone resulted in the formation of dityrosine complexes binding silk molecules together. Both silk and riboflavin are biocompatible and suitable for ocular prosthesis. Gel stiffness can be precisely controlled by adjusting the amount of light delivered, and stiffening ceased when either the light or the riboflavin was removed (Figure 7.3). Riboflavin removal was accomplished by simple rinsing which left behind a transparent hydrogel.

Like other photoactivated systems including modified silk sericin [32], this method can be used to generate high resolution patterns via photolithography. Since it is easy to control the stiffness of these gels, it should be possible to generate gels with stiffness gradients to allow the study of the effects of mechanical

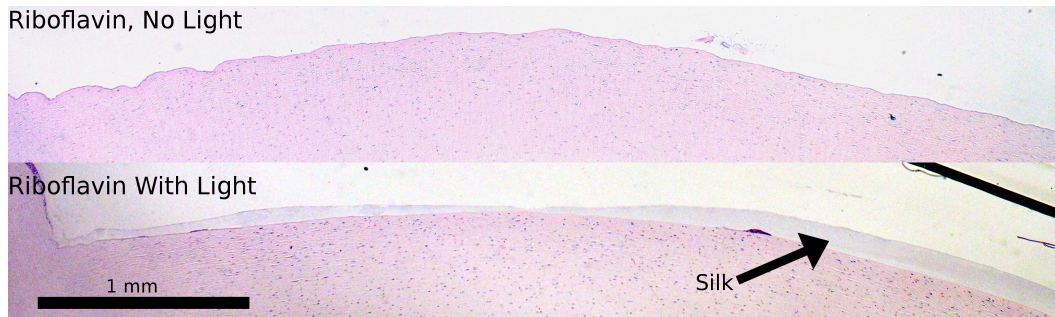


Figure 7.9: Histologic sections of porcine cornea treated with riboflavin doped silk films. Top: silk gels were not exposed to light and washed away. Bottom: Silk gel was illuminated and formed close association with corneal collagen.

cues. Using biocompatible riboflavin as a photoinitiator allows non-ionizing visible light to be used for crosslinking instead of potentially damaging ultraviolet radiation. This system could potentially be used to increase the stiffness of a gel while cell culture is ongoing to investigate how cells respond to a substrate that is increasing in stiffness over time. As gradual stiffening of extracellular matrix is a marker for diseases such as fibrosis and atherosclerosis, this material system could be helpful for understanding the evolution of these disorders. Photocrosslinked silk hydrogels show promise for the treatment of ocular injury and disease. The material can be selectively adhered to the cornea depending on the location of illumination. Adding this layer changes the optical properties of the eye and would have a profound effect on vision. For myopia and hyperopia sufferers these films could be selectively applied to change the curvature of the eye to correct vision. The silk layer presented using this technique is not yet uniform enough for the precise optical corrections needed to restore visual acuity. However, silk fibroin, like other proteins, absorbs light strongly at wavelengths shorter than 200 nm. Excimer lasers used to correct myopia and hyperopia in PRK procedures via the ablation of collagen operate at 193 nm. In addition to collagen, this type of laser has been shown to ablate a wide variety of other polymeric materials [33]. Thus,

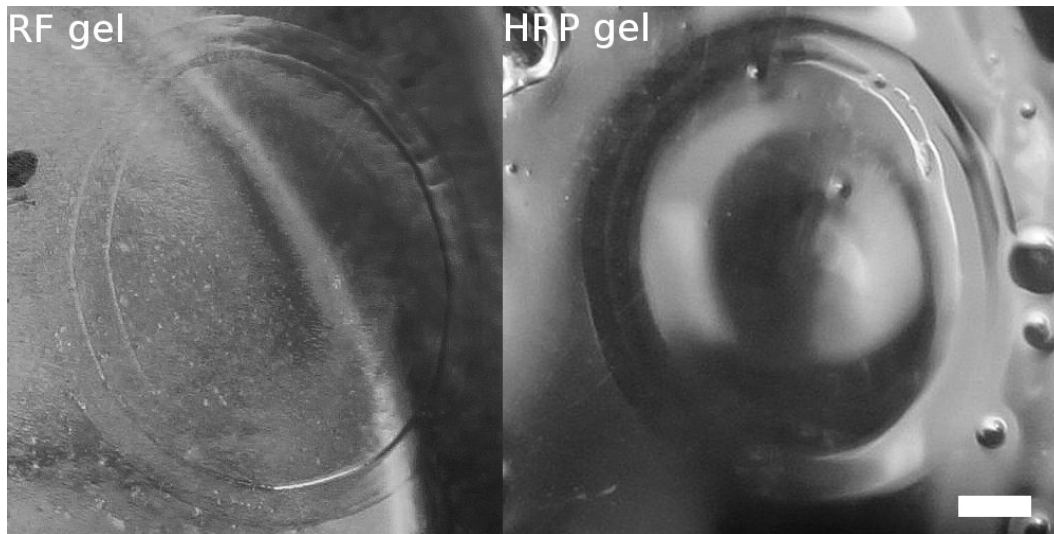


Figure 7.10: Silk gels modified by excimer laser excitation. Silk hydrogels produced by horseradish peroxidase (right) or riboflavin (left) were exposed to 36 pulses each of 193 nm excimer light from a commercial PRK machine. The region of modification closely matched the spot size indicating that such gels are amenable to shaping by excimer emissions.

precise shaping of the silk gel layer on the cornea should be amenable to PRK processing. This belief was confirmed by preliminary studies which showed the possibility of modification via exposure to excimer laser pulses (Figure 7.10). Complications due to laser corrective surgical procedures are permanent and can lead to blindness [34]. By performing laser ablation on silk prostheses instead of the native cornea, nearly risk-free laser vision correction should be possible even on patients with very thin corneas.

Future work in this area will include *in vivo* studies to ensure that corneal reepithelialization is unimpeded and that the silk gels are robust enough to withstand shear stresses associated with blinking and rubbing. Methods of producing stronger gels more quickly through the addition of horseradish peroxidase and the use of lasers to provide illumination instead of LEDs will also be investigated.

7.4 Materials & Methods

Silk fibroin protein was isolated from silkworm cocoons as described previously [35]. Briefly, cocoons were boiled in a 0.02 M sodium carbonate solution to remove the glue-like sericin protein that holds the cocoon together. The resulting fibroin was dissolved in 9.3 M lithium bromide, and dialyzed against deionized water for 72 hours. All silk used in rheometry was lyophilized and subsequently redissolved to a concentration of 6% (wt/wt) in either deionized or deuterated water.

Rheometry: The evolution of the cross-linking process was monitored by allowing samples to gel on a TA Instruments ARES-LS2 rheometer (TA Instruments, New Castle, DE). Samples were analyzed in a parallel plate configuration with a quartz top plate and stainless steel base that was maintained at 37 degrees Celsius throughout testing. Illumination was provided by 3, 450 nm LEDs providing 18.7 mW/cm² of light to the sample (Figure 7.1). Light from the LEDs passed through the top plate allowing the evolution of crosslinking to be measured in real time.

Statistics: Rheological measurements of different experimental treatments were found to have unequal variances by Bartlett's Test and the Fligner-Killeen test indicating that an analysis of variance (ANOVA) would be unreliable. Subsequent log-transformation of the data yielded approximately equal variance between the two groups (Bartlett's test p-value = 0.96). A one-way ANOVA was conducted on the log-transformed data and significance between groups was assessed with Tukey's post-hoc test.

Preliminary rheometer measurements were undertaken to find an optimum concentration of riboflavin. Highly soluble riboflavin 5'-monophosphate (FMN) was used to allow for the testing of a range of concentrations. Solutions of 0.2 mM, 2 mM, and 20 mM were tested on the rheometer as described

above and it was found that 2 mM yielded the fastest cross-linking (Figure 7.11). This concentration similar to the concentration of riboflavin used clinically for corneal crosslinking treatments (2.66 mM) [15].

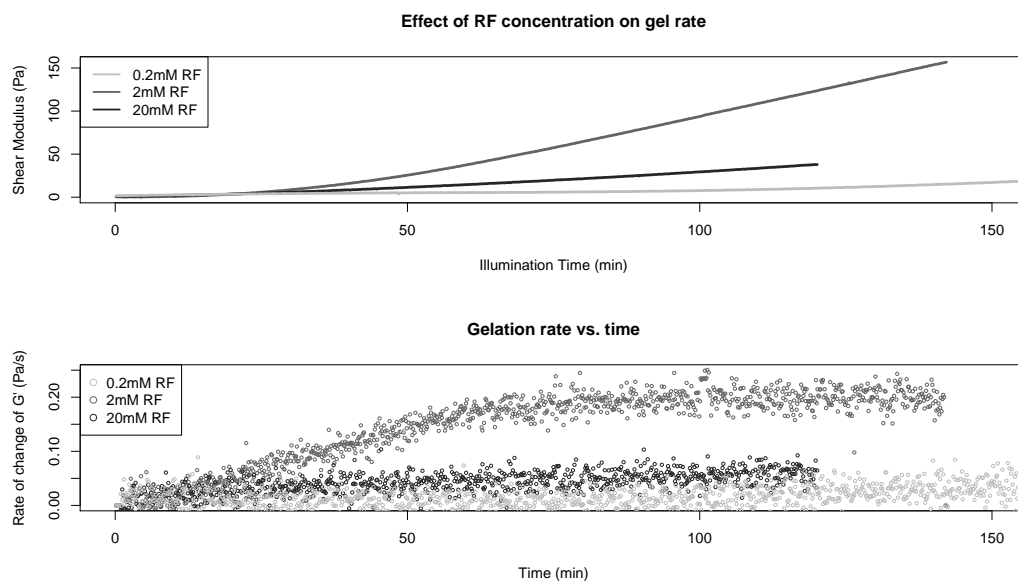


Figure 7.11: Optimizing riboflavin concentration. Top: plot showing evolution of stiffness of silk solutions containing various concentrations of riboflavin. Bottom: Numerical derivative of top plot showing that the steady-state rate of gelation is highest at a concentration of 2 mM.

Dityrosine fluorescence: Riboflavin and water were added to a silk fibroin solution to a concentration of 5% (wt/wt) silk and 2 mM riboflavin. A control solution of 5% silk was also prepared without riboflavin. 50 μL of either the riboflavin or control solution was pipetted into an opaque 96-well plate. Wells were exposed to light for 0, 20, 40, or 60 minutes. Shadowing from the walls of the well make it difficult to estimate the total light exposure over this period. Half of the riboflavin containing gels were rinsed in deionized water over the next 48 hours. Following rinsing, fluorescence spectra were collected of all wells using a Spectramax M2 (Molecular Devices, Sunnyvale, CA) micro-plate fluorescence spectrometer. Excitation wavelengths of 310 nm and 450 nm were used to look for dityrosine and riboflavin fluorescence respectively.

Photolithography: A mylar photomask with a United States Air Force resolution test pattern was obtained from Advance Reproductions (North Andover, MA). Silk solution with riboflavin was drop cast onto a glass slide and manually spread into a uniform layer. The photomask was placed 1 mm above the surface of the liquid solution and 15 J/cm² of light provided from above. Following illumination, the glass slide was placed in deionized water and agitated gently for 5 minutes. The slide was removed from the water and allowed to dry for 12 hours prior to imaging.

Corneal adhesion: Riboflavin and SOD impregnated silk films along with silk and SOD films without riboflavin were prepared by mixing the components with liquid silk solution. Riboflavin was added to a concentration of 0.2 mM and SOD added at a concentration of 1.7 U/mL. Water was added to each solution to bring the concentration of silk down to 6% (wt/wt). Fresh porcine eyes were obtained from Animal Technologies (Tyler, TX). 25% ethanol was applied to each eye to facilitate the removal of the corneal epithelium [36]. Loosened epithelium was fully removed by mechanical debridement with a razor blade. Once the cornea was cleared of epithelium, a 1 cm diameter disk of silk film was applied to the cornea. Eyes were then exposed to 15 J/cm² of 450 nm light over 20 minutes. During illumination phosphate buffered saline (PBS) was gently applied to the eye every 5 minutes to keep it moist. Samples were imaged using optical coherence tomography (OCT) before application to the eye, before illumination, after illumination, and following a vigorous rinsing with 3 mL PBS. Eyes were fixed in formalin for sectioning and staining with hemotoxylin and eosin. Silk thickness in the OCT images were measured manually using ImageJ. For statistical analysis data were averaged across all positions on the eyes. Separate multiple comparison tests were performed at each time point. ANOVAs were performed on the dry film and pre-light

time points followed by Tukey’s post-hoc test. After fitting, the residuals of the post-light and post-wash time points were not normally distributed so the non-parametric Kruskal-Wallis test was used. Differences between groups were evaluated via Dunn’s test using the Holm p-value adjustment method.

Bibliography

- [1] M.-S. Noh, B.-S. Seo, S.-J. Lee, A. Miloslavsky, C. Cork, L. Barnes, and K. Lucas, “Proceedings of the SPIE,” in *Implementing and validating double patterning in 22-nm to 16-nm product design and patterning flows* (M. V. Dusa and W. Conley, eds.), pp. 76400S–76400S–11, mar 2010.
- [2] J. W. Nichol, S. T. Koshy, H. Bae, C. M. Hwang, S. Yamanlar, and A. Khademhosseini, “Cell-laden microengineered gelatin methacrylate hydrogels,” *Biomaterials*, vol. 31, no. 21, pp. 5536–5544, 2010.
- [3] A. Khademhosseini and G. C. Bong, “Microscale technologies for tissue engineering,” *2009 IEEE/NIH Life Science Systems and Applications Workshop, LiSSA 2009*, vol. 103, no. 8, pp. 56–57, 2009.
- [4] A. M. Kloxin, A. M. Kasko, C. N. Salinas, and K. S. Anseth, “Photodegradable Hydrogels for Dynamic Tuning of Physical and Chemical Properties,” *Science*, vol. 324, pp. 59–63, apr 2009.
- [5] R. Sunyer, A. J. Jin, R. Nossal, and D. L. Sackett, “Fabrication of Hydrogels with Steep Stiffness Gradients for Studying Cell Mechanical Response,” *PLoS ONE*, vol. 7, no. 10, pp. 1–9, 2012.
- [6] B. P. Chan, I. E. Kochevar, and R. W. Redmond, “Enhancement of Porcine Skin Graft Adherence Using a Light-Activated Process,” *Journal of Surgical Research*, vol. 108, pp. 77–84, nov 2002.

- [7] A. C. O'Neill, J. M. Winograd, J. L. Zeballos, T. S. Johnson, M. a. Randolph, K. E. Bujold, I. E. Kochevar, and R. W. Redmond, "Microvascular anastomosis using a photochemical tissue bonding technique.," *Lasers in surgery and medicine*, vol. 39, pp. 716–22, oct 2007.
- [8] R. Redmond, I. E. Kochevar, M. C. McCormack, and W. G. Austen, "Clinical Potential of Light-Activated Tissue Crosslinking," in *CLEO: 2015*, (Washington, D.C.), p. AW3J.2, OSA, 2015.
- [9] S. Stinnett, M. W. Grinstaff, and T. Kim, "New Dendritic Adhesives for Sutureless Ophthalmic Surgical Procedures," *Arch. Ophthalmol*, vol. 122, pp. 867–870, 2013.
- [10] E. E. Verter, T. E. Gisel, P. Yang, A. J. Johnson, R. W. Redmond, and I. E. Kochevar, "Light-initiated bonding of amniotic membrane to cornea.," *Investigative ophthalmology & visual science*, vol. 52, pp. 9470–7, jan 2011.
- [11] D. Miki, K. Dastgheib, T. Kim, A. Pfister-Serres, K. a. Smeds, M. Inoue, D. L. Hatchell, and M. W. Grinstaff, "A photopolymerized sealant for corneal lacerations.," *Cornea*, vol. 21, no. 4, pp. 393–399, 2002.
- [12] R. H. Kennedy, W. M. Bourne, J. A. Dyer, and Others, "A 48-year clinical and epidemiologic study of keratoconus," *Am J Ophthalmol*, vol. 101, no. 3, pp. 267–273, 1986.
- [13] J. B. Jonas, V. Nangia, A. Matin, M. Kulkarni, and K. Bhojwani, "Prevalence and associations of keratoconus in rural maharashtra in central India: the central India eye and medical study," *American journal of ophthalmology*, vol. 148, no. 5, pp. 760–765, 2009.

- [14] N. S. Gokhale, “Epidemiology of keratoconus,” *Indian Journal of Ophthalmology*, vol. 61, no. 8, p. 382, 2013.
- [15] G. Wollensak, E. Spoerl, and T. Seiler, “Riboflavin/ultraviolet-a-induced collagen crosslinking for the treatment of keratoconus,” *American Journal of Ophthalmology*, vol. 135, pp. 620–627, may 2003.
- [16] H. Tao, D. L. Kaplan, and F. G. Omenetto, “Silk materials - a road to sustainable high technology,” *Advanced materials*, vol. 24, pp. 2824–37, jun 2012.
- [17] F. G. Omenetto and D. L. Kaplan, “A new route for silk,” *Nature Photonics*, vol. 2, no. 11, pp. 641–643, 2008.
- [18] M. B. Applegate, G. Perotto, D. L. Kaplan, and F. G. Omenetto, “Bio-compatible step index optical waveguides,” *Biomedical optics express*, vol. (forthcomi, 2015.
- [19] J. L. Whittaker, N. R. Choudhury, N. K. Dutta, and A. Zannettino, “Facile and rapid ruthenium mediated photo-crosslinking of Bombyx mori silk fibroin,” *Journal of Materials Chemistry B*, vol. 2, no. 37, p. 6259, 2014.
- [20] H. A. Wee and P. J. Dyson, “Classical and non-classical ruthenium-based anticancer drugs: Towards targeted chemotherapy,” *European Journal of Inorganic Chemistry*, no. 20, pp. 4003–4018, 2006.
- [21] S. Ibusuki, G. J. Halbesma, M. a. Randolph, R. W. Redmond, I. E. Kochevar, and T. J. Gill, “Photochemically cross-linked collagen gels as three-dimensional scaffolds for tissue engineering,” *Tissue engineering*, vol. 13, pp. 1995–2001, aug 2007.

- [22] E. Masurovsky and E. Peterson, “Photo-reconstituted collagen gel for tissue culture substrates,” *Experimental Cell Research*, vol. 76, pp. 447–448, feb 1973.
- [23] S.-H. Kim and C.-C. Chu, “Fabrication of a biodegradable polysaccharide hydrogel with riboflavin, vitamin B2, as a photo-initiator and L-arginine as coinitiator upon UV irradiation.,” *Journal of biomedical materials research. Part B, Applied biomaterials*, vol. 91, pp. 390–400, oct 2009.
- [24] A. K. Nguyen, S. D. Gittard, A. Koroleva, S. Schlie, A. Gaidukeviciute, B. N. Chichkov, and R. J. Narayan, “Two-photon polymerization of polyethylene glycol diacrylate scaffolds with riboflavin and triethanolamine used as a water-soluble photoinitiator.,” *Regenerative medicine*, vol. 8, pp. 725–38, nov 2013.
- [25] A. Yildirim, H. Cakir, N. Kara, H. Uslu, B. Gurler, E. B. Ozgurhan, and H. N. Colak, “Corneal collagen crosslinking for ectasia after laser in situ keratomileusis: Long-term results.,” *Journal of cataract and refractive surgery*, pp. 1–6, aug 2014.
- [26] A. S. McCall, S. Kraft, H. F. Edelhauser, G. W. Kidder, R. R. Lundquist, H. E. Bradshaw, Z. Dedeic, M. J. C. Dionne, E. M. Clement, and G. W. Conrad, “Mechanisms of corneal tissue cross-linking in response to treatment with topical riboflavin and long-wavelength ultraviolet radiation (UVA).,” *Investigative ophthalmology & visual science*, vol. 51, pp. 129–38, jan 2010.
- [27] Y. Kato, K. Uchida, and S. Kawakishi, “Aggregation of collagen exposed to UVA in the presence of riboflavin: a plausible role of tyrosine modification.,” *Photochemistry and photobiology*, vol. 59, pp. 343–9, mar 1994.

- [28] E. P. L. Hunter, M. F. Desrosiers, and M. G. Simic, “The effect of oxygen, antioxidants, and superoxide radical on tyrosine phenoxyl radical dimerization,” *Free Radical Biology and Medicine*, vol. 6, no. 6, pp. 581–585, 1989.
- [29] E. Silva, S. Fürst, and A. Edwards, “Visible light anaerobic photoconversion of tyrosine sensitized by riboflavin. Cytotoxicity on mouse tumoral cells,” *Photochemistry and . . .*, vol. 62, no. 6, pp. 5–9, 1995.
- [30] L. A. Marquez and H. B. Dunford, “Kinetics of Oxidation of Tyrosine and Dityrosine by Myeloperoxidase Compounds I and II: IMPLICATIONS FOR LIPOPROTEIN PEROXIDATION STUDIES,” *Journal of Biological Chemistry*, vol. 270, pp. 30434–30440, dec 1995.
- [31] B. P. Partlow, C. W. Hanna, J. Rnjak-Kovacina, J. E. Moreau, M. B. Applegate, K. A. Burke, B. Marelli, A. N. Mitropoulos, F. G. Omenetto, and D. L. Kaplan, “Highly Tunable Elastomeric Silk Biomaterials,” *Advanced Functional Materials*, pp. 4615–4624, apr 2014.
- [32] N. E. Kurland, T. Dey, C. Wang, S. C. Kundu, and V. K. Yadavalli, “Silk protein lithography as a route to fabricate sericin microarchitectures,” *Advanced Materials*, vol. 26, no. 26, pp. 4431–4437, 2014.
- [33] R. Srinivasan and B. Braren, “Ultraviolet laser ablation of organic polymers,” *Chemical Reviews*, vol. 89, pp. 1303–1316, 1989.
- [34] J. B. Randleman and R. D. Shah, “LASIK Interface Complications: Etiology, Management, and Outcomes,” *Journal of Refractive Surgery*, vol. 28, pp. 575–588, aug 2012.
- [35] D. N. Rockwood, R. C. Preda, T. Yücel, X. Wang, M. L. Lovett, and

D. L. Kaplan, “Materials fabrication from Bombyx mori silk fibroin,”
Nature protocols, vol. 6, pp. 1612–31, oct 2011.

- [36] M. Griffith, W. B. Jackson, M. D. Lafontaine, G. Mintsioulis, P. Agapitos,
and W. Hodge, “Evaluation of current techniques of corneal epithelial
removal in hyperopic photorefractive keratectomy,” *Journal of Cataract
& Refractive Surgery*, vol. 24, no. 8, pp. 1070–1078, 1998.

Chapter 8

Conclusion & future directions

In this dissertation many ways in which light/matter interactions can be used to sculpt silk fibroin were described as well as a method for using silk to alter the propagation of light within biological tissue. This work presented several techniques for shaping soft silk materials that allow high-resolution patterning which would be impossible using conventional techniques. It was shown that silk is uniquely suited for light-based processing for biomedical applications due to its exceptional transparency, strength, and biocompatibility. In Chapter 3, the unexpectedly large multiphoton cross-section of silk given its amino acid composition was shown. This surprising finding led to the exploration three-dimensional photopatterning of silk fibroin. The large multiphoton cross-section of silk enabled 810 nm light with modest peak intensity ($\sim 100 \text{ MW/cm}^2$) to be absorbed up to 1 cm below the surface of the material and that this absorption of light led to the formation of a void. The unprecedented depth at which features could be produced allowed large-scale structures to be formed inside the gel without cumbersome and labor intensive stacking steps. In Chapter 4, the mechanism by which voids were formed was investigated. Here, the shape and size of the voids were accurately modeled

using a finite element approach. Assuming Gaussian focusing and a purely 3-photon absorption process, a map of the light intensity in both time and space was produced, and the amount of energy absorbed during a typical laser exposure could be estimated at each location. A threshold energy absorption was found such that, if the energy absorbed exceeded it, the location within the gel would be denatured and become a void. Actual void measurements were compared with simulated exposures and it was determined that this critical energy was approximately 60 pJ/molecule. The model was able to accurately predict void size and shape relying solely on scaling with the cube of intensity, suggesting that multiphoton absorption in silk at NIR wavelengths is a purely 3-photon process. This finding supported the conclusions drawn in Chapter 3. The model did not depend on pulse repetition rate implying that accumulation of heat or other photoproducts were not primary mechanisms of void formation. This model also proved useful for sweeping through various parameters *in silico* and determining the conditions under which material removal was maximized. The most favorable conditions were long duration of exposure to high energy pulses with the shortest possible pulse width. In the range of wavelengths tested, 740 nm light was most efficiently absorbed by the silk. The optimum spot size depended on pulse energy, with larger spots being capable of removing more material when the pulse energy is high. However, larger spots also tend to decrease the achievable axial resolution regardless of pulse energy. In Chapter 5 a method for the formation of complex 3D voids inside silk gels by translating the sample relative to the focus of the beam was studied. By mounting the sample on a computer controlled 3-axis translation stage moving at an average speed of $\sim 100 \mu\text{m/s}$ structures up to 400 μm in diameter could be made in a practical amount of time. These features were then used to guide cell growth and migration both *in vitro* and *in vivo*. It was

verified that cells embedded within the hydrogel were able to survive irradiation with the ultrashort pulses of light provided they were not in the focal volume of the beam. No other available modality allows pre-determined voids to be formed within a solid substrate with such high resolution. This work is an important first step toward high resolution pre-vascularization of artificial organ constructs and fills a gap in current biocompatible manufacturing. In Chapter 6 focus shifts from the paradigm of light being used to alter silk to the framework of using silk to alter light. The high index of refraction and near complete transparency of silk make it an attractive material for optical waveguides. By encapsulating a silk film ($n \approx 1.54$) inside a silk hydrogel ($n \approx 1.34$) nearly complete confinement of light within the film was achieved. This work has the potential to deliver high intensity light to targets deep within tissue to increase the penetration of imaging modalities that rely on ballistically scattered photons such as optical coherence tomography, as well as light-based therapies such as photodynamic therapy. Finally, Chapter 7 returned to the theme of light being used to alter the structure of silk and showed how riboflavin could be used as a photoinitiator to crosslink silk via the formation of dityrosine bonds when exposed to blue or ultraviolet light. It was also shown how, using riboflavin, silk could be directly adhered to corneal collagen. This bonding could provide a means to safely augment corneas which have been affected by disease or injury.

8.1 Future Directions

In many instances, the work presented here is still in its infancy, with only proof-of-concept of results shown. To translate these findings to clinical or industrial use, further work must be undertaken. The ability to deterministi-

cally pattern 3D voids within the hydrogel has implications for the creation of artificial blood vessels. Future work will attempt to integrate these structures with conventional microfluidic devices constructed from polydimethylsiloxane (PDMS) or molded silk hydrogels [1]. In silk hydrogel microfluidics, laser micromachining could be used to add additional high resolution branches to the structure to improve diffusion into the gel. It has already been shown that the laser machining process is compatible with cell-laden hydrogels so this would be an attractive application to increase the concentration of oxygen and nutrients available for encapsulated cells. The ability to use these structures in artificial organ application also depends on the thrombogenic properties of the material. Work towards epithelializing the laser produced channels would reduce the risk of clot and enable faster translation to the clinic. The ability to pattern voids at the microscale fills a currently missing niche in 3D patterning of biomaterials. There are numerous techniques for generating large-scale (~ 5 mm) tubular structures, and using sacrificial substrates, random interconnected voids on the nano-scale can be produced. There is no other technique, however, that can be used to create deterministic voids with resolutions approaching 1 micron within a large volume.

One of the main challenges of multiphoton processing is the cost of the equipment. In order for multiphoton micromachining to be widely adopted by the biomedical community it must be translated from the optical table to the wet lab. To do so, the large solid-state laser used here must be replaced with a small form factor fiber laser that won't require regular alignment and tuning. Current femtosecond fiber laser technology is available in the required wavelength range, pulse energy, and pulse width to achieve rapid micromachining of silk hydrogels. Based on the laser and the lenses required, a reasonable estimate for the cost of purchasing a system to be approximately \$100,000.

As technology improves, the peak intensities available will rise even as costs fall. This trend will enable the production of multiphoton micromachining workstations at a reasonable cost to labs around the world.

The speed of fabrication is also a major challenge. The work presented in Chapter 4 described how the laser parameters could be tuned to maximize light absorption, but adjustments to the optomechanical setup could also be made to speed up the process. Depending on the resolution required, the XYZ-translation stage could be replaced with compact, high-speed galvanometer driven mirrors. Scanning galvanometers allow for a relatively wide area to be rapidly addressed, but the spot size is limited. For high-resolution applications the use of a piezoelectric stage and an immersion objective would be ideal. Although the depth of penetration would be limited in this case, it should allow the production of 3D nanometer scale features. Nanostructured silk hydrogels could be used to produce photonic crystals with point defects for use as sensors or waveguides.

The final hurdle in the widespread use of multiphoton micromachining is that relatively few labs have expertise in using silk. The discovery that tryptophan is responsible for the ease of multiphoton processing in silk fibroin (Chapter 3) hints that the technique of multiphoton micromachining may be extensible to other biocompatible materials. Keratin, a structural protein like silk, contains tryptophan natively and is a promising target for multiphoton structuring. Other commonly used biomaterials (collagen, alginate, poly(vinyl)-alcohol, etc.) have the potential to be chemically modified to include tryptophan to increase their multiphoton absorption cross-section. It is likely that the addition of tryptophan would increase the ability of these materials to be patterned using ultrashort pulses of light. Preliminary work has already shown that alginate gels soaked in a tryptophan solution is much

more amenable to laser modification than alginate soaked in water. The use of tryptophan as a photoinitiator is almost surely safer than other photoinitiators on the market enabling the use of photomodification in experiments that are highly sensitive to toxins.

Using silk to alter the path of light through the body has tremendous implications for imaging and therapy of deep targets. Silk is excellent at stabilizing labile compounds such as dyes, antibodies, and enzymes, all of which could be easily incorporated into the silk optical waveguides. One possible avenue of research would be to include carriers that release drugs when exposed to certain wavelengths of light. A silk optical waveguide could be left behind after surgery and used to watch for infection. If detected, a second wavelength of light could be used to release high concentration of antibiotics or anti-inflammatory drugs directly to the site of the problem. Once healed, the waveguide could be left behind to degrade naturally. In this case, the biggest challenge is to reduce the amount of light lost in the waveguide. Currently, much of the lost light appears to exit from the rough edges of the film. The edges are rough because the PDMS mold used to create the waveguide was not perfectly smooth. Using a smoother substrate would allow the silk films to form without a jagged edge and should help keep the light confined to the film until reaching the output facet. For *in vivo* use, the dimensions of the fiber would ideally to be reduced to the smallest practical diameter. Silk has an advantage over other polymers because even at very small diameters it remains mechanically robust. Initial work casting the silk onto a Fresnel lens with ~ 0.5 mm grooves yielded thin films capable of guiding light, but repeatability was a challenge. As the dimensions are reduced, creation of a single mode waveguide becomes a possibility. With a single mode guide, biocompatible fiber imaging bundles could be produced which would allow multichannel imaging and

sensing, vastly increasing the waveguides' utility.

Using riboflavin to photocrosslink silk also has potential for tissue engineering and other applications. As was shown in Chapter 7, the photoinitiator can be used to adhere silk tightly to corneal collagen. This work has the potential to allow for low-cost, and nearly risk-free laser vision correction surgery. Due to silk's transparency, this adherence could also find application in a wide variety of ophthalmologic scenarios. One potential application is in the treatment of corneal wounds. Current techniques involve the use of cyanoacrylate glues [2]. However, these glues must be kept dry in order to cure requiring the eye to be kept dry for an uncomfortably long 2-4 minutes. In addition, cyanoacrylate glues are impermeable to fluids which can result in conjunctivitis [3]. The most commonly used alternative to cyanoacrylate is fibrin glues which are derived from human blood. These glues provide a more permeable, biocompatible seal but put patients at increased risk of transmission of viruses from the blood donor. Fibrin glues are also weaker than cyanoacrylates. [4] Adhesion of silk to the corneal surface with riboflavin and visible light could provide a viable alternative to both cyanoacrylate and fibrin glues.

The two hurdles to implementation of silk/riboflavin gels in these applications are the speed of crosslinking, and the strength of the gel itself. To improve the speed, silk films could be made with riboflavin, horseradish peroxidase (HRP), and superoxide dismutase (SOD). When applied to the eye a dilute solution of hydrogen peroxide (H_2O_2) could be dripped on top of the film and simultaneously exposed to light. The riboflavin will help the silk react with the collagen, forming a tight bond, and the HRP/ H_2O_2 could help the silk crosslink to itself improving the strength of the material. Additional research would need to be done to ensure that the low concentrations of peroxide needed to crosslink the gel are tolerated by the corneal epithelium. Since

the mechanism for forming HRP gels and silk/riboflavin gels is essentially the same, it should be possible to achieve gel strengths comparable to the pure HRP gels which are strong enough to support native corneal pressure. To further improve the speed of crosslinking, additional concentrations and combinations of enzymes could be tested. In the work presented here only a single concentration of SOD and HRP were used. It is possible that varying the concentrations and ratios of these enzymes could yield faster crosslinking rates. The other way to improve the crosslinking speed is to increase the amount of light incident on the gel. The use of a laser at a raking angle to the cornea could provide required amount of light in a matter of seconds without damaging the retina.

Another intriguing possibility for silk/riboflavin crosslinking is to use multiphoton absorption to drive the reaction. In Chapter 7 we showed how 2D patterns could be generated using a photomask, but the confinement of light absorption to the focal volume would allow the generation of 3D patterns as well. Preliminary results suggest that multiphoton photocrosslinking is possible (Figure 8.1). The use of riboflavin as a photoinitiator means that only benign, biocompatible chemicals would be used in this technique making it suitable for biomedical applications. Multiphoton photocrosslinking could also be combined with multiphoton micromachining in which riboflavin gels could be cross-linked and ablated with the same laser. The major hurdles that would need to be overcome for this technique to be practical are the adherence of the silk to the substrate and the speed of the reaction. In early trials it was difficult to reliably adhere the crosslinked silk to the substrate. Careful choice of substrate materials and possibly chemical modifications to the substrate might be necessary. To increase the speed of the reaction higher light intensities could be used. One way this could be accomplished would be

to use amplified femtosecond pulses. This would potentially allow single-shot crosslinking near the surface, but issues of self-focusing would arise at greater crosslinking depths. If these issues could be overcome the use of riboflavin as a photoinitiator to crosslink silk could provide a biocompatible, mask-free, rapid prototyping system with very high resolution and extreme flexibility.

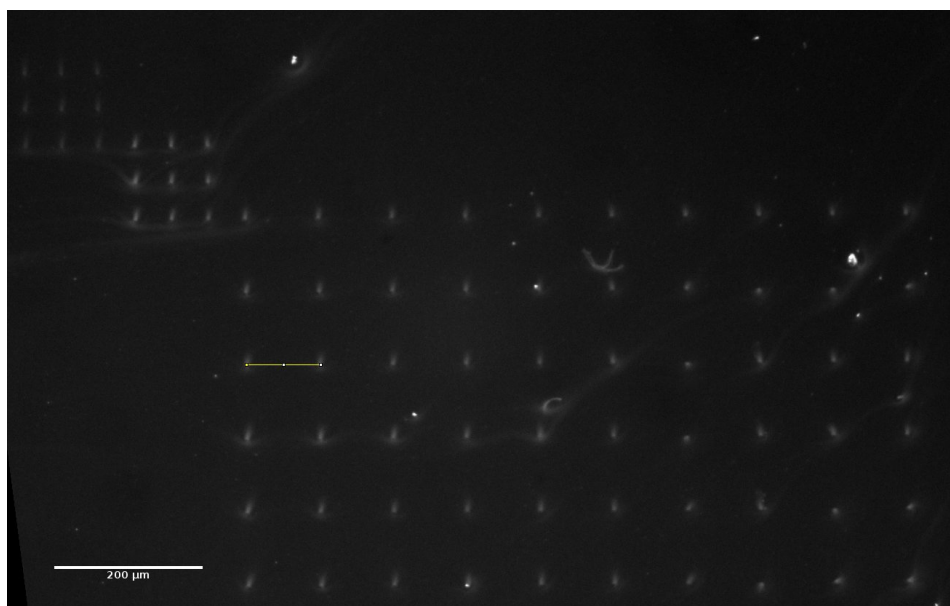


Figure 8.1: Fluorescence image of riboflavin photcrosslinked with ultrashort pulses of NIR light. Bright dots indicate the presence of riboflavin only in the regions exposed to light.

Light is a unique tool for the structuring of materials. Given sufficient intensity, nearly all materials can be affected by light making it extremely versatile. It is also relatively easy to control with the wide availability of turnkey laser systems and diffraction-limited lenses. Light offers extremely high spatial resolution. Whether utilizing deep UV lithography for patterning silicon wafers on the nanometer scale, or taking advantage of nonlinear optical effects to reduce the volume of light/matter interaction, the precision with which light can be controlled is unparalleled. Processing via light is also very gentle typically requiring no physical contact. This allows even soft, fragile materials to be patterned or shaped using light without collateral damage. As discussed

in Chapter 1, the use of light for processing materials in biomedicine is gaining popularity with dozens of new applications and technologies appearing each year.

As noted throughout this dissertation, silk fibroin is a fantastic material for biomedical applications, and it particularly well suited to light-driven processing: it is exceptionally transparent, extremely strong, can support cell growth, and is uniquely amenable to multiphoton absorption. The use of light to modify silk, and silk to modify light, hold great promise for the future diagnosis and treatment of disease.

Bibliography

- [1] S. Zhao, Y. Chen, B. P. Partlow, A. S. Golding, P. Tseng, J. Coburn, M. B. Applegate, J. E. Moreau, F. G. Omenetto, and D. L. Kaplan, “Bio-functionalized silk hydrogel microfluidic systems,” *Biomaterials*, vol. 93, pp. 60–70, 2016.
- [2] B. J. Vote and M. J. Elder, “Cyanoacrylate glue for corneal perforations: A description of a surgical technique and a review of the literature,” *Clinical and Experimental Ophthalmology*, vol. 28, no. 6, pp. 437–442, 2000.
- [3] A. N. Carlson and K. R. Wilhelmus, “Giant papillary conjunctivitis associated with cyanoacrylate glue,” *American journal of ophthalmology*, vol. 104, no. 4, pp. 437–438, 1987.
- [4] A. Panda, S. Kumar, A. Kumar, R. Bansal, and S. Bhartiya, “Fibrin glue in ophthalmology,” *Indian journal of ophthalmology*, vol. 57, no. 5, p. 371, 2009.

Appendix A

Model feature

```
getFeature3s = function(Pow,repRate,pWidth, sSize,
    lambda,conc,mu,d,time,r,z,Ec,shape='sech2'){
    #Function to calculate void location at all points in space

    #Pow is power in Watts
    #repRate is the pulse repetition frequency in Hz
    #pWidth is pulse FWHM in femtoseconds
    #sSize is the FWHM spot size in microns
    #lambda is the wavelength in nanometers
    #mu is the depth dependent exponential coefficient (1/mm)
    #d is the depth in mm
    #r is the mesh of radial points in microns
    #z is the mesh of axial points in microns
    #NB: Mesh is assumed to include only positive values for r and z due to
        symmetry

    require(reshape2)

    dz = z[2]-z[1] #Resolution in z-direction
    dr= r[2]-r[1] #Resolution in r direction
    fw1em = 1.699 * sSize #Conversion of FWHM to FW(1/e^2)M
```

APPENDIX A. MODEL FEATURE

```
w0 = .5* fw1em #Beam radius HW(1/e^2)M (micron)
zR = (pi*w0^2)/(lambda/1000) #Rayleigh range (micron)
Ep = Pow/repRate #J Energy of the pulse
pWidths=pWidth*1e-15 #Converting fs to seconds

#For gaussian pulse shape
if (shape=='gaussian'){
  a= .94*(Ep/pWidths) #Peak power (W)
  c= pWidths/(2*sqrt(2*log(2))) #The standard deviation of the Gaussian
  #P(t) = a*exp((t^2)/(c^2))
  tDep=a^3*c*sqrt((2*pi)/3) #Integral of P(t)^3 from -infy to infy
    (gaussian)
}

#For sech^2 pulse shape
else if (shape == 'sech2'){
  a= .88*(Ep/pWidths) #Peak power (W) also the height of the simulated
    pulse
  b= 1.76/pWidths #The width term of the sech^2
  #P(t) = a * sech^2(b*t)
  tDep=a^3*16/(15*b) #Integral of P(t)^3 from -infy to infy (sech^2)
}

else{
  stop('Pulse shape not recognized.')
}

wz = w0*sqrt(1+(z/zR)^2) #Beam width as a function of z

voxVolume = 2*pi*r*dr*dz #Volume of a voxel (um^3)
voxMass = voxVolume * 1e-12 * conc/100 #Mass of a voxel (g)(1 cubic
  micron is 1e-12 mL)
sfMass = 55000 #Molar mass of 60mb silk (Wray2011) g/mole
molPerMole = 6.02e23 #molecules/mole Avagadro's number
massPerMolecule = sfMass/molPerMole #g/molecule
```

APPENDIX A. MODEL FEATURE

```

molPerVox = voxMass/massPerMolecule #molecules/voxel
molPerum3 = molPerVox/voxVolume #molecule/um^3

ener = matrix(0,length(z), length(r)) #Pre-allocating space for
      intensity map
sig=8.6e-77 *1e24#um^6s^2/ph^2 Molecular 3PA cross-section of 60 mb silk
      (Applegate2013)
sp_l = 3e8 #m/s speed of light
h=6.63e-34 #W s^2 Planck's constant

Eph = (h*sp_l)/(lambda*1e-9) #Photon Energy J/photon
sig_W = sig / Eph^2 #Conversion of Photon^2 to W^2 (um^6/W^2)

#####Scales sigma based on wavelength (empirically
      derived)#####
lams=c(740,750,770,780,790,800,810,820,830,840,860,880) #Wavelengths
      measured
vols=c(4.15, 4.2, 1.55, .9, 0.72, 0.45, 1.00, .95, .38, .45,
      .37, .3) #Volumes measured at the various wavelengths normalized
      to the value at 810 nm
thisLam = as.numeric(approx(lams,vols,xout=lambda,rule=2)$y) #Estimate
      the absorption of this sample
#####

#Calculate the amount of absorbed energy at each location
for (thisR in seq(1:length(r))) { #Iterate over r-locations
  ener[,thisR] = 8/(wz^6*pi^3)*exp((-6*r[thisR]^2)/(wz^2))* #Space
      dependent intensity^3 (vector)
  exp(-3*mu*d)* #Reduced intensity due to depth below surface cubed
      (number)
  tDep* #Integral of P(t)^3 (number)
  sig_W*mean(molPerum3,na.rm=T)*thisLam*2*pi*r[thisR]*dr*dz* #Energy
      absorbed/pulse around the whole ring
}

```

```
    time*repRate #number of pulses
}

#Reshape the matrix for easier plotting and calculations
ener=t(ener)

#Set r and z locations as columns instead of indices
longEner=melt(ener,id.vars=c("r","z"))
names(longEner)=c('r','z','Energy')
#Calculate threshold value (molPerVox is a vector that repeats as needed)
longEner$Threshold = Ec*molPerVox
#Test whether critical energy is exceeded
longEner$Void = longEner$Energy > longEner$Threshold
#Recast r and z as indices
fMap=acast(longEner,r~z,value.var="Void") #Map of void region

#Calculate the volume of the feature -- assumes no holes in feature
fCoords=which(fMap==1, arr.ind=T) #Indices of array
if (dim(fCoords)[1] != 0){
  fdf = data.frame(rows=fCoords[,1],cols=fCoords[,2])
  wfdf = dcast(fdf,cols ~ rows,value.var="cols") #Wide feature data frame
  wfdf = !is.na(wfdf) #Binarize
  #At each R location, sum the total number of void pixels -- this is the
  #radius of the void
  rvec = (apply(wfdf, 1, sum)-2)*dr #micron

  fvol=sum(pi*rvec^2*dz) #Numerical integration of stacked cylinders to
  #calculate volume
}

#If no void is produced
else{rvec = 0
fvol = 0
}

#Return stuff you might need
```

```
getFeature3s =  
  list("Volume"=fvol*2,"energyMap"=ener,"featureMap"=fMap,"rLoc"=r,"zLoc"=z)  
}
```

Appendix B

ImageJ Macro

```
//Macro to automatically estimate the volume
//of removed material from yz phase contrast images
//First open the file you'd like to analyze

run("Set Scale...", "distance=5.9 known=1 unit=um"); //For the 20x objective
run("Set Measurements...", "area mean fit redirect=None decimal=3")

fTimes = 1.111 //Features are 11% brighter than background.
dir=getDirectory("image"); //Returns directory of current image
im=getTitle(); //Returns title of current image
short_name=split(im, '.'); //Strips the '.tiff' off the image name

//Mouse click flags
lmb_clicked=0;
lmb_released=0;

run("Smooth"); //Smooth the image

print("Select rectangle containing only background")
```

```
setTool("rectangle");
run("Select None");

//Wait for user to select background area
while (lmb_clicked == 0 || lmb_released==0){
    getCursorLoc(x,y,z,flags);
    if(flags &16 != 0) {
        lmb_clicked=1;
    }
    if(lmb_clicked == 1&&flags==0){
        lmb_released=1;
    }
    wait(10);
}

\\Measure average background value
run("Measure");
mVal=round(getResult("Mean", (nResults-1)));

tVal = round(mVal*fTimes); \\Threshold must be integer

print(tVal); \\Output value (for debugging)

run("Rotate 90 Degrees Left"); \\Rotate image

setThreshold(tVal,4095); //Sets threshold

run("Convert to Mask"); //Make the image binary

//Analyze the particles in the image (only with low circularity) and add
to manager
run("Analyze Particles...", "size=25-Infinity circularity=0.00-.2
show=Outlines display");
```

